# Mechanistic Aspects of CO<sub>2</sub> Reduction Catalysis with Manganese-Based Molecular Catalysts

David C. Grills,\*,† Mehmed Z. Ertem,\*,† Meaghan McKinnon,§ Ken T. Ngo,§ and Jonathan Rochford\*,§

<sup>†</sup>Chemistry Division, Brookhaven National Laboratory, P. O. Box 5000, Upton, NY 11973-5000 United States

§Department of Chemistry, University of Massachusetts Boston, 100 Morrissey Boulevard, Boston, Massachusetts 02125, United States

#### **Abstract**

One approach for the conversion of  $CO_2$  into fuels or fuel precursors is the proton-coupled reduction of  $CO_2$  to CO or formic acid, using transition-metal complexes as catalysts in either electrocatalytic or photocatalytic processes. While a number of such molecular catalysts have been investigated over the years, many are based on expensive precious metals. However, a family of precatalysts with the generic formula,  $[Mn(\alpha\text{-diimine})(CO)_3L]^{+/0}$ , based on the earth-abundant metal, manganese, has recently emerged as a promising, cheaper alternative to the heavily-investigated Re-based analogues. In this review, we discuss the current mechanistic understanding of these and related Mn-based  $CO_2$  reduction precatalysts, from the point of view of both computational modeling and experimental techniques. We also highlight the methods used to accurately determine catalytic figures of merit, such as overpotential and turnover frequency. Finally, we have summarized the major findings in both electrocatalytic and photocatalytic  $CO_2$  reduction driven by Mn-based catalysts, including exciting new developments involving immobilization of the molecular catalysts on solid supports or electrodes, and also their use in photoelectrochemical  $CO_2$  reduction where solar energy is used to overcome the demanding electrochemical overpotential.

#### **Contents**

- 1. Introduction
  - 1.1 Manganese vs. rhenium tricarbonyl CO<sub>2</sub> reduction catalyst precursors
- 2. Mechanistic aspects of CO<sub>2</sub> reduction by group 7 catalysts
  - 2.1 Electrocatalytic CO<sub>2</sub> reduction
  - 2.2 Photocatalytic CO<sub>2</sub> reduction
- 3. Thermodynamic aspects of CO<sub>2</sub> reduction in aqueous and non-aqueous solvents
  - 3.1 Case study: A comparison of overpotentials for analogous Mn- and Re-based CO<sub>2</sub> reduction catalysts
- Experimental mechanistic investigations of CO<sub>2</sub> reduction by Mn-based complexes
  - 4.1 Electrochemical methods
    - 4.1.1 Voltammetry
    - 4.1.2 Controlled potential (bulk) electrolysis
    - 4.1.3 Infrared spectroelectrochemistry (IR-SEC)
  - 4.2 Electron paramagnetic resonance (EPR) spectroscopy
    - 4.2.1 Comments on the tetracarbonyl intermediates
  - 4.3 Stopped-flow techniques
  - 4.4 Time-resolved infrared (TRIR) spectroscopy
  - 4.5 Pulse radiolysis coupled with time-resolved infrared spectroscopy (PR-TRIR)
- 5. Summary of Mn-based CO<sub>2</sub> reduction catalysts
  - 5.1. Electrocatalysis
    - 5.1.1  $\alpha$ -diimine ligand modification
    - 5.1.2 Monodentate ligand 'L' modification.
    - 5.1.3 Brønsted and Lewis acid dependence
    - 5.1.4 Supramolecular assembly
    - 5.1.5 Catalyst immobilization
  - 5.2 Photocatalysis
    - 5.2.1 Introduction to photocatalytic CO<sub>2</sub> reduction
    - 5.2.2 Redox photosensitizers for reductive quenching
    - 5.2.3 Sacrificial electron donors
    - 5.2.4 Measurement of photocatalytic performance
    - 5.2.5 Published reports of photocatalytic CO<sub>2</sub> reduction using Mn-based catalysts
- 6. Conclusions and future outlook

Acknowledgements

References

#### 1. Introduction

The rise of atmospheric CO<sub>2</sub> beyond 400 ppm for the first time in human history is a major concern across the scientific community and the world as a whole. Utilizing our knowledge of synthesis, thermodynamics and kinetics, the chemical community has been striving towards the discovery of green and economically viable technologies to capture atmospheric CO<sub>2</sub> and also reduce future CO<sub>2</sub> emissions. The conversion of CO<sub>2</sub> into C-1 fuels, e.g., methanol or formic acid (HCO<sub>2</sub>H) and fuel precursors, such as carbon monoxide (CO), is a viable strategy to achieve a sustainable, carbon-neutral, global energy technology. One highly desired, yet challenging, approach is the proton-coupled catalytic conversion of CO<sub>2</sub> to CO or HCO<sub>2</sub>H in an electrocatalytic process using electrical potential energy (ideally derived from renewable sources such as solar energy), or in a photocatalytic process where photon energy absorbed by a catalyst or photosensitizer is stored in the form of chemical bonds in CO<sub>2</sub> reduction products. Currently, industrial CO production uses the Boudouard disproportionation of CO2 over 'coke' at 800 °C [1], or the steam reforming of low molecular weight hydrocarbons at ~1000 °C to produce synthesis-gas ( $H_2$ :CO ~ 3:1) [2]. The principal use of CO is as synthesis-gas for the production of long-chain hydrocarbons ( $C_nH_{2n+1}$ , n = 10 - 20) by the Fischer-Tropsch process [3]. Formic acid is also a highly valued product of CO<sub>2</sub> reduction as it is less toxic and nonflammable compared to CO. Moreover, formic acid is a liquid product which can be directly used in an efficient fuel cell [4-6]. Formic acid is produced at a scale of 720,000 tones/annum (for feed preservation, leather and textile processing, flue gas desulfurization) via the hydrolysis of methyl formate; ironically a product of MeOH and CO [7]. Ultimately, there is enormous demand for both CO and HCO<sub>2</sub>H, thus presenting great potential for a carbon neutral sustainable economy.

Transition metal complexes are prime candidates for the development of selective CO<sub>2</sub> reduction electrocatalysts and photocatalysts as they offer easy access to a diverse range of metal oxidation states and ligand structures to allow electronic fine-tuning of the metal center and optimization of hydrogen-bonding in the second coordination sphere. This is no more evident than in nature with the [NiFe] CO dehydrogenase enzyme which promotes the proton-coupled reduction of CO<sub>2</sub> to CO [8]. Molecular homogeneous transition metal-based catalysts have long been utilized for electrocatalytic CO<sub>2</sub> reduction [8-10], as the often formed metallocarboxylate intermediate reduces the reorganization energy for CO<sub>2</sub> activation by stabilizing a bent configuration of the carboxylate anion [11]. A comprehensive review of all transition metal catalysts for CO<sub>2</sub> reduction is beyond the scope of this review, and the reader is therefore directed to a number of excellent reviews on this topic [8, 9, 12-24].

This manuscript will focus solely on CO<sub>2</sub> reduction catalysis with complexes based on the first-row transition metal, manganese (Mn), and specifically the *fac*-MnX(L<sub>2</sub>)(CO)<sub>3</sub> class of catalyst precursors, where L<sub>2</sub> is typically a bidentate polypyridyl or related ligand and X is a monodentate ligand. The majority of MnX(L<sub>2</sub>)(CO)<sub>3</sub> complexes favor a facial (*fac*) arrangement of their three CO ligands, as opposed to the meridional isomer (*mer*), so for the purpose of this review the *fac* label will be dropped unless specifically relevant. MnX(L<sub>2</sub>)(CO)<sub>3</sub> complexes have become the focus of intense investigation in recent years, in part due to their high product selectivity for CO formation, but also because they are based on a much cheaper, more earthabundant metal compared to their more thoroughly investigated Re-based counterparts. A major goal of this review is to provide a detailed description of our current understanding of the mechanism for proton-coupled CO<sub>2</sub> reduction by the MnX(L<sub>2</sub>)(CO)<sub>3</sub> class of catalysts. To

achieve this, a summary of reported computational studies is provided with an overview of the relevant thermodynamic parameters that collectively define the challenges of this chemistry. This is followed by a discussion of the principle experimental methods utilized to probe the catalytic mechanism. In particular, the  $MnX(L_2)(CO)_3$  class of catalysts and their reactive intermediates exhibit very characteristic and strong infrared (IR) features due to their distinctive  $\nu(CO)$  stretches. Thus, a major effort has been made to summarize all  $\nu(CO)$  IR data for the reported catalysts and their reactive intermediates where available. Finally, a summary of the catalytic properties of  $MnX(L_2)(CO)_3$  systems is provided for both electrochemically and photochemically driven processes.

#### 1.1 Manganese vs. rhenium tricarbonyl CO<sub>2</sub> reduction catalyst precursors

Prior to discussing the details of CO<sub>2</sub> activation by homogeneous MnX(L<sub>2</sub>)(CO)<sub>3</sub> catalyst precursors, it is pertinent to consider their properties relative to the more extensively studied rhenium congeners. Since the first report by Hawecker, Lehn, and Ziessel of the photocatalytic reduction of CO<sub>2</sub> to CO with ReCl(bpy)(CO)<sub>3</sub> (bpy = 2,2'-bipyridine, Fig. 1, 1) using near-UV light in the presence of a sacrificial electron donor [12, 25, 26], and Meyer's pioneering studies indicating the existence of both one- and two-electron pathways for the electrocatalytic reduction of CO<sub>2</sub> to CO with the same complex [27], there have been many literature reports of related Rebased photo/electro-catalytic systems, with numerous reviews written on the topic [9, 14, 15, 18, 22, 28-32]. While reports of unsuccessful attempts at catalytic CO<sub>2</sub> conversion by Mn-based catalysts are rare [33], as are reports of stoichiometric CO<sub>2</sub> fixation by Mn complexes [34], it was not until a recent 2011 article by Deronzier, Chardon-Noblat and co-workers [35] that the successful application of MnBr(α-diimine)(CO)<sub>3</sub> (where α-diimine is bpy or 4,4'-dimethyl-2,2'-

bipyridine (dmbpy), Fig. 1, 2 and 3) as an electrocatalyst precursor for the proton-mediated conversion of CO<sub>2</sub> to CO was reported, in acetonitrile (CH<sub>3</sub>CN) in the presence of 5% (2.78 M) H<sub>2</sub>O. In contrast to their Re(I) analogues, which can reduce CO<sub>2</sub> in the absence of an added proton source, it is now understood that the Mn(I) catalysts typically require the presence of an excess source of Brønsted acid for the binding of CO<sub>2</sub> and formation of a key Mn(I) metallocarboxylic acid intermediate to occur. In hindsight, this observation helps to explain the lack of catalytic behavior previously reported for MnCl(bpy)(CO)<sub>3</sub> (Fig. 1, 4) in the absence of an appreciable proton source [36]. This prerequisite has been investigated computationally by Carter and co-workers [37, 38] and is discussed in detail below in Section 2 'Mechanistic Aspects of CO<sub>2</sub> Reduction by Group 7 Catalysts'. In Section 3 'Thermodynamic Aspects of CO<sub>2</sub> Reduction in Aqueous and Non-Aqueous Solvents', where a discussion of how to accurately determine catalyst overpotential is first provided, a direct comparison of the electrocatalytic properties of [M(bpy)(CO)<sub>3</sub>(CH<sub>3</sub>CN)]<sup>+</sup>, where M = Re(I) or Mn(I) (Fig. 1, 5 and 6), is presented.

**Figure 1.** Molecular structures of some of the first studied Mn- and Re-based CO<sub>2</sub> reduction precatalysts (1 - 4) plus the  $[M(bpy)(CO)_3(CH_3CN)]^+$  acetonitrile complexes where M = Re (5) or Mn (6) discussed herein. Citations are provided in parentheses.

# 2. Mechanistic aspects of CO<sub>2</sub> reduction by group 7 catalysts

Photo– and electrochemical conversion of  $CO_2$  to higher energy products, particularly to CO and formate (HCOO<sup>-</sup>), by manganese (Mn) and rhenium (Re) catalysts has been investigated in several computational studies [37-47]. Density functional theory (DFT) calculations have been performed to compute reduction potentials,  $pK_as$ , reaction free energies ( $\Delta G$ ) and free energies of activation ( $\Delta G^{\ddagger}$ ) in order to gain insight into the mechanism of catalytic  $CO_2$  reduction and product selectivity of the associated catalysts. Although DFT calculations have been the primary choice in many computational studies, in recent years post-Hartree-Fock (post-HF) level of theories such as domain based local pair natural orbital (DLPNO) single- and double-excitation coupled cluster (DPLNO-CCSD) [48], and DLPNO-CCSD with perturbative inclusion of triplet excitations (DLPNO-CCSD(T)) [49] methods have been employed for benchmark calculations in mechanistic studies of  $CO_2$  reduction by Mn– and Re–based complexes [37, 38, 47].

# 2.1 Electrocatalytic CO<sub>2</sub> reduction

In their seminal studies, Carter and co-workers examined several aspects of the mechanism of the proton-dependent electrocatalytic reduction of CO<sub>2</sub> to CO by **1** and **2** catalyst precursors [37, 38]. A common set of pathways for the generation of possible products after one— and two–electron reduction of **1** and **2** have been investigated at the B3LYP-D3 level of theory [50-53] in conjunction with the COSMO solvation model [54] for CH<sub>3</sub>CN.

The proposed mechanistic pathways, as depicted in Scheme 1, start with a single electron reduction resulting in the formation of  $[M^{I}X(bpy^{\bullet-})(CO)_{3}]^{-}$  (where M = Mn or Re and X = Br or Cl<sup>-</sup>) or M<sup>I</sup>(bpy<sup>-</sup>)(CO)<sub>3</sub> depending on whether the halide anion stays bound or dissociates during the reduction event. The formation of a pentacoordinate M<sup>I</sup>(bpy•-)(CO)<sub>3</sub> species could result in coordination of a solvent CH<sub>3</sub>CN molecule to the vacant site or alternatively dimerization to form  $[M^0(bpy)(CO)_3]_2$ . The computed free energy changes ( $\Delta Gs$ ) indicate that the pentacoordinate Re<sup>I</sup>(bpy<sup>\*-</sup>)(CO)<sub>3</sub> species prefers to bind a chloride ion or a solvent molecule, ΔG = -7.7 and -6.0 kcal/mol respectively, whereas the pentacoordinate intermediate is favored for Mn<sup>I</sup>(bpy•-)(CO)<sub>3</sub>, which can further react with another Mn<sup>I</sup>(bpy•-)(CO)<sub>3</sub> to form the Mn<sup>0</sup>-Mn<sup>0</sup> dimer complex [Mn<sup>0</sup>(bpy)(CO)<sub>3</sub>]<sub>2</sub>. The DFT calculations reveal twice as much net α spin population on Mn ( $\sigma_{\alpha} = 0.47$ ) compared to that on Re ( $\sigma_{\alpha} = 0.25$ ) for the M<sup>I</sup>(bpy•-)(CO)<sub>3</sub> species, indicating that metal-based reduction is more favorable for the case of Mn, consistent with the preference for a pentacoordinate intermediate. This is in line with the experimental observations of a much greater dimerization rate constant for Mn<sup>I</sup>(dtbpy $^{\bullet-}$ )(CO)<sub>3</sub> ( $2k_{\text{dim}} = (1.3 \pm 0.1) \times 10^9 \text{ M}^{-1}$  $s^{-1}$ ; dtbpy = 4,4'-ditertbutyl-2,2'-bipyridine) to generate dimer 8 (Fig. 2), [55] compared to  $Re^{I}(dmbpy^{\bullet-})(CO)_3$  ( $2k_{dim} = 40 \text{ M}^{-1} \text{ s}^{-1}$ ) to generate the  $[Re^{0}(dmbpy)(CO)_3]_2$  dimer, [56] since the fraction of pentacoordinate Re<sup>I</sup>(bpy<sup>•</sup>-)(CO)<sub>3</sub> available for dimerization is predicted to be much smaller than that of Mn<sup>I</sup>(bpy•-)(CO)<sub>3</sub>.

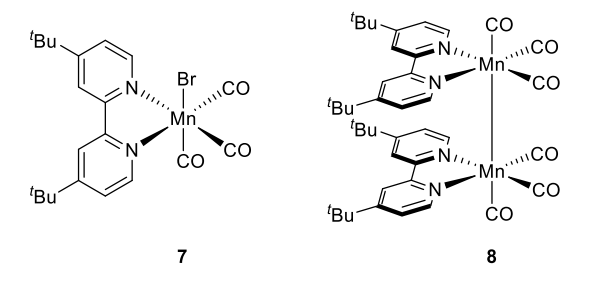


**Figure 2.** Molecular structures of MnBr(dtbpy)(CO)<sub>3</sub> (7) and dimeric [Mn(dtbpy)(CO)<sub>3</sub>]<sub>2</sub> (8) [55, 57].

After the second reduction step, a common reactive [M<sup>0</sup>(bpv<sup>•</sup>-)(CO)<sub>3</sub>]<sup>-</sup> intermediate forms which may react with  $CO_2$  to generate  $[M^I - CO_2]^ (M = M(bpy)(CO)_3$  moiety) or alternatively with a proton donor to form a hydride species, M<sup>I</sup>-H. The computed activation barriers with phenol as the proton source indicate that the CO<sub>2</sub> binding pathway is favored by ≅10 kcal/mol for both Mn and Re catalysts, which provides a plausible explanation for the high selectivity of these catalysts towards CO rather than hydrogen or formate production, the latter formed via CO<sub>2</sub> insertion into a M<sup>I</sup>-H bond [58]. A significant distinction between Mn and Re complexes is that the CO<sub>2</sub> binding step is predicted to be thermodynamically uphill ( $\Delta G = 2.2$ kcal/mol) for the former complex while it is downhill ( $\Delta G = -3.4 \text{ kcal/mol}$ ) for the latter, even though the kinetics of binding is predicted to be similar for both catalysts ( $\Delta G^{\ddagger} \cong 3.3 \text{ kcal/mol}$ ). An important outcome of the distinct CO<sub>2</sub> binding affinities is the requirement of a Brønsted acid to protonate and stabilize the [M<sup>I</sup>-CO<sub>2</sub>]<sup>-</sup> intermediate in the case of Mn catalysts, in agreement with the experimental observations of a lack of catalytic CO<sub>2</sub> reduction activity of 4 in the absence of weak Brønsted acids [33]. The protonation of [M<sup>I</sup>–CO<sub>2</sub>]<sup>-</sup> to generate M<sup>I</sup>–CO<sub>2</sub>H with phenol as the proton source is determined to be facile (barrierless) and highly exergonic ( $\Delta G \cong$ −33 kcal/mol) for both Mn and Re catalysts.

**Scheme 1.** Common set of pathways for the generation of possible products proposed by Carter and co-workers [37] after one— and two— electron reductions of MnBr( $\alpha$ -diimine)(CO)<sub>3</sub> and ReCl( $\alpha$ -diimine)(CO)<sub>3</sub> in CH<sub>3</sub>CN, where  $\alpha$ -diimine = bpy and related R-substituted bpy ligands.

Carter and co-workers identified two possible pathways for the formation of CO and H<sub>2</sub>O from the **M**<sup>I</sup>-CO<sub>2</sub>H intermediate, labeled as *protonation–first* and *reduction–first* pathways in Scheme 1 [37]. The *protonation–first* pathway starts with heterolytic C–OH bond cleavage facilitated by a proton donor leading to the formation of H<sub>2</sub>O and [**M**<sup>I</sup>-CO]<sup>+</sup>, which is further reduced to generate M<sup>I</sup>(bpy<sup>\*</sup>-)(CO)<sub>4</sub>. In contrast, the *reduction–first* pathway proceeds with reduction of [**M**<sup>I</sup>-CO<sub>2</sub>H] followed by heterolytic C–OH bond cleavage yielding H<sub>2</sub>O and the common M<sup>I</sup>(bpy<sup>\*</sup>-)(CO)<sub>4</sub> intermediate. Stepwise or concerted one-electron reduction and CO evolution steps complete the catalytic cycle, regenerating the active [M<sup>0</sup>(bpy<sup>\*</sup>-)(CO)<sub>3</sub>]<sup>-</sup> catalyst.

The computed activation free energies are identified to be quite similar for the rate determining chemical step of proton coupled C-OH bond scission for both pathways and catalysts ( $\Delta G^{\ddagger} \cong 11 \text{ kcal/mol}$ ). Importantly, the microkinetic simulations performed by Carter and co-workers on the basis of computed reduction potentials, free energy changes and activation free energies (which are refined by LPNO- [59] and DLPNO-CCSD(T) [49] calculations) demonstrated that only the *reduction-first* pathway is plausible for the Re catalyst whereas both *protonation-first* and *reduction-first* pathways could be operating for the Mn catalyst depending on the applied potential and the p $K_a$  of the proton source.

In a joint experimental and computational study, Agarwal et al investigated the reduction of CO<sub>2</sub> to CO by the MnBr(HOPhbpy)(CO)<sub>3</sub> (HOPhbpy = 6-(2-hydroxyphenyl)-2,2'-bipyridine) complex, which features a phenolic proton source adjacent to the Mn center where CO<sub>2</sub> binding occurs (Fig. 3 9) [42]. The authors performed DFT calculations at the M06-L level of theory [60] with the CPCM continuum solvation model [61, 62] for CH<sub>3</sub>CN to probe the underlying reasons for the enhancement in catalytic activity towards electrochemical reduction of CO<sub>2</sub> by 9 compared to 2 or MnBr(MeOPh-bpy)(CO)<sub>3</sub> (MeOPhbpy = 6-(2-methoxyphenyl)-2,2'-bipyridine) (Fig. 3 10).

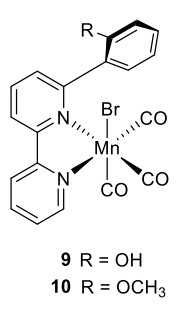


**Figure 3.** Molecular structures of pre-catalysts **9** and **10** reported by Agarwal et al. [42] where the bpy ligand contains a hydroxyphenyl or methoxyphenyl substituent at one of the bpy 6-positions.

Theoretical calculations indicate that the attack of Mn<sup>I</sup>–CO<sub>2</sub>H by a CO<sub>2</sub> molecule (Fig. 4a-b) to generate  $[Mn^I–(CO)_4]^+$  and  $HCO_3^-$  is associated with high activation free energies ( $\Delta G^{\ddagger}=34.0$  and 25.0 kcal/mol), whereas the presence of the phenol group as a proton source in the second coordination sphere facilitates the C–OH bond cleavage ( $\Delta G^{\ddagger}=13.0$  kcal/mol) by providing a pathway for proton-assisted dehydration of Mn<sup>I</sup>–CO<sub>2</sub>H (Fig. 4c) and decreasing the entropic cost associated with the activation energy.

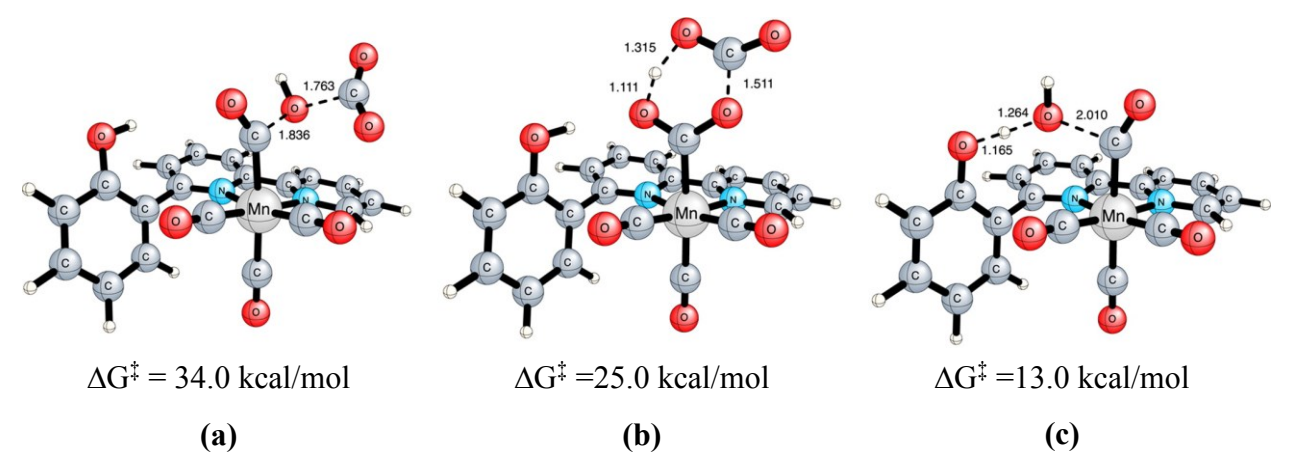


**Figure 4.** Optimized transition state structures for: (**a-b**) the interaction of a molecule of CO<sub>2</sub> with Mn(HOPh-bpy)(CO)<sub>3</sub>(COOH), and (**c**) the proton-assisted dehydration of Mn(HOPh-

bpy)(CO)<sub>3</sub>(COOH). Reproduced with permission from ref. [42]. Copyright 2015 American Chemical Society.

Lam et al revisited the electrocatalytic CO<sub>2</sub> reduction mechanism of [Mn<sup>0</sup>(bpy•-)(CO)<sub>3</sub>] with 2,2,2-trifluoroethanol (CF<sub>3</sub>CH<sub>2</sub>OH, TFE) as the proton source, focusing on the effect of homoconjugation (CF<sub>3</sub>CH<sub>2</sub>O<sup>-</sup>/CF<sub>3</sub>CH<sub>2</sub>OH) or formation of a carbonate adduct intermediate (CF<sub>3</sub>CH<sub>2</sub>OCO<sub>2</sub><sup>-</sup>) of the deprotonated TFE alkoxide anion on the energetics of the steps involving hydrogen bonding to, or proton transfer from, TFE molecules [43]. The authors performed DFT calculations at the B3LYP-D3 level of theory with a Poisson Boltzmann (PBF) continuum solvation model [63] for CH<sub>3</sub>CN and presented an electrocatalytic cycle similar to that proposed by Carter and co-workers (Scheme 1) for both [Mn<sup>0</sup>(bpy<sup>•-</sup>)(CO)<sub>3</sub>]<sup>-</sup> and [Mn<sup>0</sup>(bpm<sup>•-</sup>)(CO)<sub>3</sub>]<sup>-</sup> (where bpm is 2,2'-bipyrimidine, Fig. 5, 11) complexes. Computed activation free energies ( $\Delta G^{\ddagger}$ = 18.9 and 21.1 kcal/mol, for bpy and bpm respectively) were more favorable for the heterolytic C-OH bond cleavage step following the reduction-first pathway compared to those of the protonation-first pathway ( $\Delta G^{\ddagger} = 22.2$  and 23.7 kcal/mol, for bpy and bpm respectively). Although the predicted  $\Delta G^{\ddagger}$ s were higher in the case of the bpm ligand (therefore lower predicted turnover frequencies), the reduction of Mn<sup>I</sup>–CO<sub>2</sub>H in the reduction–first pathway was 0.5 V more favorable (-1.69 V and -1.19 V vs SCE, for bpy and bpm respectively) consistent with the greater electron affinity of the bpm ligand. As a consequence of these observations, [Mn<sup>0</sup>(bpm<sup>\*</sup>-)(CO)<sub>3</sub>] was predicted to perform electrocatalytic CO<sub>2</sub> reduction at lower overpotentials compared to [Mn<sup>0</sup>(bpy<sup>•</sup>-)(CO)<sub>3</sub>]<sup>-</sup> at the expense of lower turnover frequencies.

Rawat et al investigated the mechanism and product selectivity of a *N*-heterocyclic carbene pyridine (NHC-py) containing MnBr(NHC-py)(CO)<sub>3</sub> complex (Fig. 5, **12**) for electrocatalytic CO<sub>2</sub> reduction using the B3LYP-D3 method and the CPCM continuum solvation model for CH<sub>3</sub>CN [44]. The authors demonstrated that except in the presence of very strong acids (e.g., HCl) as the proton donor, CO<sub>2</sub> binding to the [Mn<sup>0</sup>(NHC-py<sup>-</sup>)(CO)<sub>3</sub>]<sup>-</sup> intermediate is strongly favored over proton transfer from a Brønsted acid to generate the hydride intermediate, Mn<sup>1</sup>(H)(NHC-py)(CO)<sub>3</sub>, which provides high selectivity towards CO formation rather than hydrogen or formate as products, similar to [Mn<sup>0</sup>(bpy<sup>-</sup>)(CO)<sub>3</sub>]<sup>-</sup>. An interesting finding observed in the computed structures is the weak interaction of the nitrogen atom of the carbene with CO<sub>2</sub> in Mn<sup>1</sup>Br(NHC-py)(CO)<sub>3</sub> and [Mn<sup>0</sup>Br(NHC-py<sup>-</sup>)(CO)<sub>3</sub>]<sup>-</sup> complexes, which might assist in the dissociation of the halide ion.

**Figure 5.** Molecular structures of the [Mn(bpm)(CO)<sub>3</sub>]<sup>-</sup> anion **11** investigated by Lam et al. and the MnBr(NHC-py)(CO)<sub>3</sub> complex **12** investigated by Rawat et al [44].

Recently, Ngo et al reported the electrocatalytic reduction of  $CO_2$  to CO by the  $\{Mn^I([(MeO)_2Ph]_2bpy)(CO)_3(CH_3CN)\}^+([(MeO)_2Ph]_2bpy = 6,6'-bis(2,6-dimethoxyphenyl)-2,2'-bipyridine) complex (Fig. 6, 13), demonstrating the first example of a catalyst which provides access to the$ *protonation–first*pathway, thus minimizing the overpotential requirement [47].

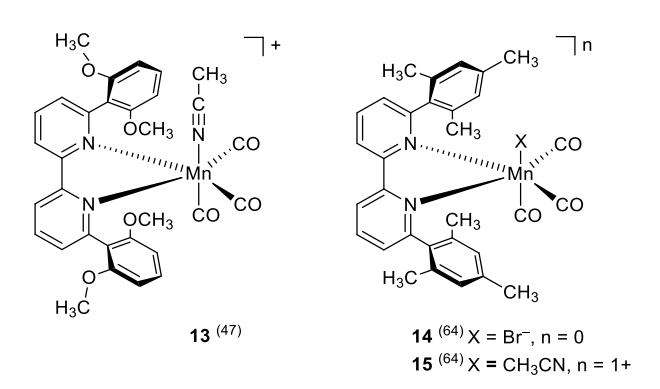


**Figure 6.** Molecular structures of MnX( $\alpha$ -diimine)(CO)<sub>3</sub> CO<sub>2</sub> reduction precatalysts **13 - 15** where  $\alpha$ -diimine is a 6,6'-disubstituted 2,2'-bipyridyl ligand. Citations are provided in parentheses.

The steric influence imposed by the  $[(MeO)_2Ph]_2$ bpy ligand, similar to the 6,6'-dimesityl-2,2'-bipyridine (mes<sub>2</sub>bpy) ligand (Fig. 6, **14** and **15**) reported earlier by Sampson et al. inhibits Mn<sup>0</sup>–Mn<sup>0</sup> dimerization upon one-electron reduction [64]. Additionally however, the presence of methoxy groups located in close proximity to the Mn center in the report by Ngo et al. enables weak allosteric hydrogen–bonding interactions with Brønsted acids. This effectively lowers the activation free energies associated with the heterolytic C–OH bond cleavage step, thus promoting the *protonation–first* pathway. DFT calculations performed at the M06 level of theory [65] coupled with the SMD continuum solvation model [66] showed that the  $\Delta G^{\ddagger}$ s associated with the C–OH bond cleavage step (Fig. 7) are significantly lower for the *protonation–first* pathway for the Mn<sup>1</sup>([(MeO)<sub>2</sub>Ph]<sub>2</sub>bpy)(CO)<sub>3</sub>(CO<sub>2</sub>H) complex compared to those for Mn<sup>1</sup>(mes<sub>2</sub>bpy)(CO)<sub>3</sub>(CO<sub>2</sub>H) (e.g.,  $\Delta G^{\ddagger} = 25.1$  vs 30.7 kcal/mol, respectively, using TFE as a proton source) in line with the experimental observations that only the former catalyst promotes the *protonation–first* pathway to a significant extent. The authors also performed DLPNO-CCSD(T) calculations for the activation energies associated with the *protonation–first* pathway

of both complexes for a set of Brønsted acids (H<sub>2</sub>O, MeOH, TFE, PhOH) to assess the performance of a set of selected density functionals. Similar qualitative results were identified for all the functionals tested, with the M06-L functional providing the best quantitative agreement with the DLPNO-CCSD(T) level of theory.

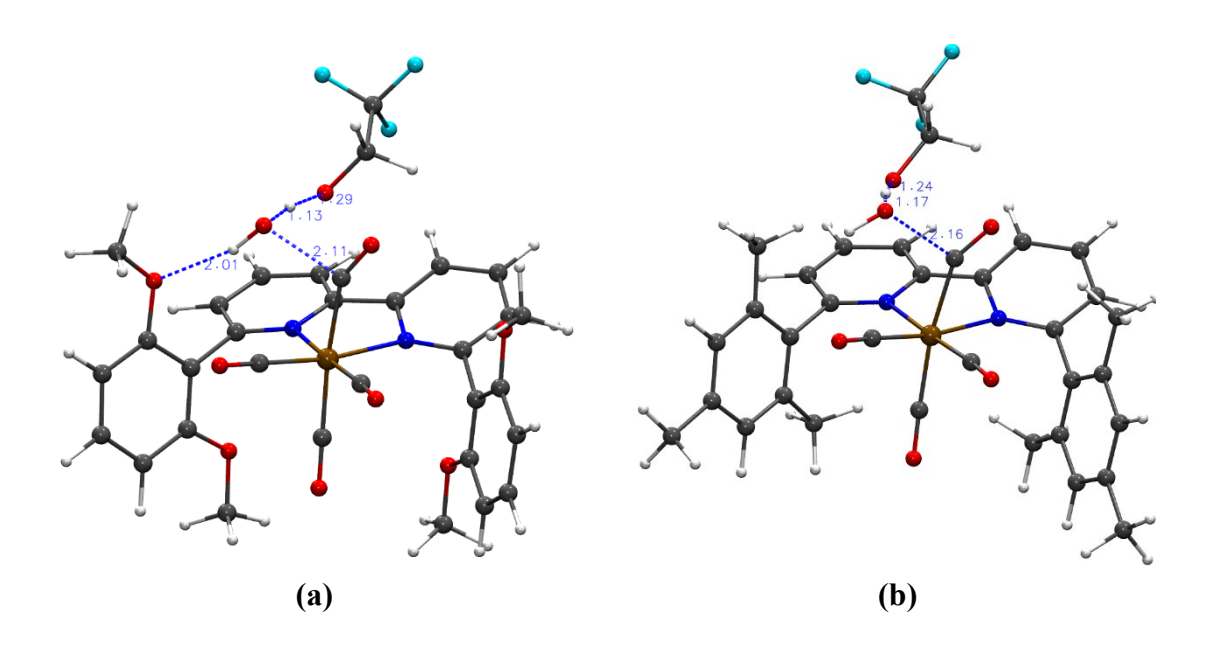
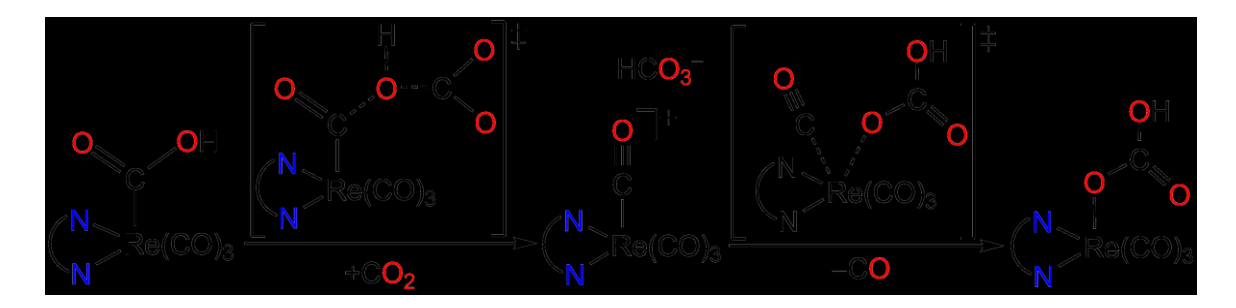


**Figure 7.** Optimized transition state structures for heterolytic C–OH bond cleavage for the *protonation–first* pathway using TFE as the proton source for (a) Mn<sup>I</sup>([(MeO)<sub>2</sub>Ph]<sub>2</sub>bpy)(CO)<sub>3</sub>(CO<sub>2</sub>H) and (b) Mn<sup>I</sup>(mes<sub>2</sub>bpy)(CO)<sub>3</sub>(CO<sub>2</sub>H). Color code: Mn, ochre; C, gray; N, blue; O, red; F, cyan; H, white. Selected distances (Å) are shown as blue dashed lines.

# 2.2 Photocatalytic CO<sub>2</sub> reduction

While the focus of this manuscript in primarily on the catalytic conversion of CO<sub>2</sub>, primarily to CO and HCOO<sup>-</sup>, by homogeneous Mn catalysts, there are a number of Re-based computational studies which should be considered as they highlight alternative pathways (relative to Scheme 1) for CO<sub>2</sub> reduction. While these studies are inspired by experimental studies which have utilized photoinitiated catalysis they are equally relevant to electrochemical methods as analogous reactive intermediates may be generated at an electrode surface.

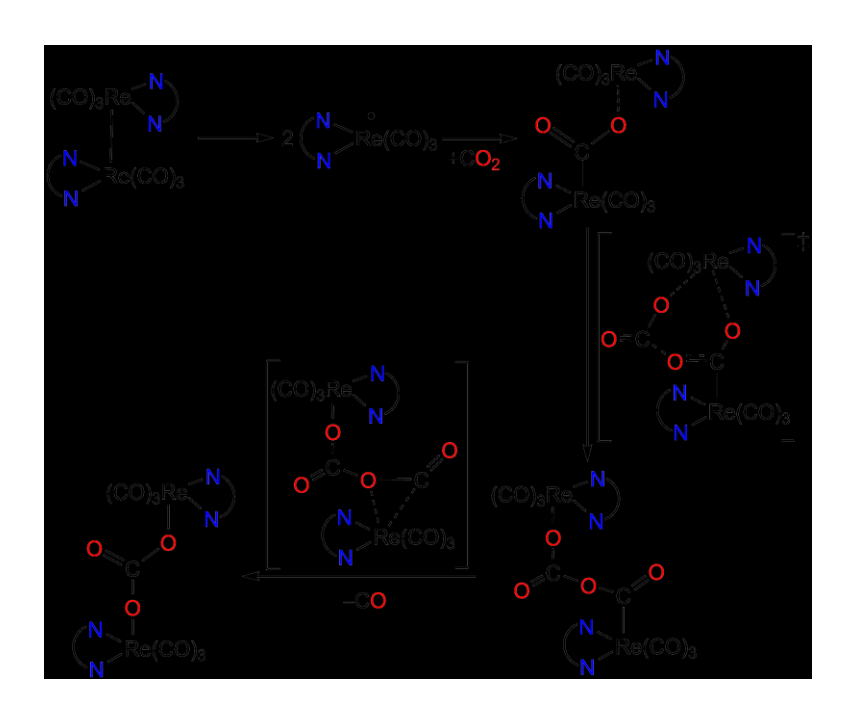
In an early work, Muckerman and co-workers investigated the mechanism of CO evolution from Re<sup>I</sup>(bpy)(CO)<sub>3</sub>(COOH) using DFT calculations [39]. Geometry optimizations at the M06-L level of theory in conjunction with the CPCM continuum solvation model for DMSO were performed to study the reaction between Re<sup>I</sup>(bpy)(CO)<sub>3</sub>(COOH) and CO<sub>2</sub> (Scheme 2). The authors uncovered that CO<sub>2</sub> could react with Re<sup>I</sup>(bpy)(CO)<sub>3</sub>(COOH) to generate a [Re<sup>I</sup>(bpy)(CO)<sub>4</sub>][HCO<sub>3</sub><sup>-</sup>] complex salt with an activation enthalpy ( $\Delta$ H<sup>‡</sup>) of 24 kcal/mol. In the following step, the HCO<sub>3</sub><sup>-</sup> counteranion displaces CO via associative ligand exchange ( $\Delta$ H<sup>‡</sup> = 12 kcal/mol) to generate the Re<sup>I</sup>(bpy)(CO)<sub>3</sub>(OCO<sub>2</sub>H) bicarbonate complex (Scheme 2). The proposed mechanism was also supported by <sup>13</sup>CO<sub>2</sub> isotope labeling experiments, which demonstrated that the HCO<sub>3</sub><sup>-</sup> anion originates from the CO<sub>2</sub> substrate upon reacting with Re<sup>I</sup>(bpy)(CO)<sub>3</sub>(COOH).



**Scheme 2.** Proposed mechanism by Muckerman and co-workers [39] for CO evolution via the reaction of Re<sup>I</sup>(bpy)(CO)<sub>3</sub>(COOH) with CO<sub>2</sub>.

In their following work, using a similar computational methodology, Muckerman and coworkers studied the mechanistic details of formation of a rhenium carbonate dimer. [Re(bpv)(CO)<sub>3</sub>]<sub>2</sub>(OCO<sub>2</sub>), and CO via photocleavage of the [Re<sup>I</sup>(bpv)(CO)<sub>3</sub>]<sub>2</sub> dimer in CO<sub>2</sub>saturated N.N-dimethylformamide (DMF) solvent (Scheme 3) [40]. The initial step of the proposed mechanism involves generation of two pentacoordinate Re<sup>I</sup>(bpy<sup>•-</sup>)(CO)<sub>3</sub> complexes via photocleavage of the Re<sup>0</sup>-Re<sup>0</sup> bond, which in turn react with a carbon dioxide molecule to generate the carboxylate dimer ( $\Delta H = -36 \text{ kcal/mol}$ ), [Re(bpy)(CO)<sub>3</sub>]<sub>2</sub>(OCO), in an effective two-electron reduction of CO<sub>2</sub>. The insertion of a second molecule of CO<sub>2</sub> proceeds with  $\Delta H^{\ddagger}$  = 22 kcal/mol to yield the [Re(bpy)(CO)<sub>3</sub>]<sub>2</sub>(OC(O)OCO) intermediate, which upon rearrangement evolves CO forming the carbonate-bridged rhenium dimer,  $[Re(bpv)(CO)_3]_2(OCO_2)$  ( $\Delta H^{\ddagger} = 15.3$ kcal/mol) (Scheme 3). The proposed mechanism agrees well with earlier experimental observations [27, 67] of the analogous dmbpy complex, specifically with identification of  $[Re^{I}(dmbpy)(CO)_{3}]_{2}(O^{13}CO)$ <sup>13</sup>CO. long-lived intermediate and  $[Re^{I}(dmbpy)(CO)_{3}]_{2}(O^{13}CO_{2})$  and  $[Re^{I}(dmbpy)(CO)_{3}]_{2}(O^{13}C(O)OH)$  as products from the

reaction of the [Re<sup>I</sup>(dmbpy)(CO)<sub>3</sub>]<sub>2</sub> dimer in <sup>13</sup>CO<sub>2</sub>-saturated DMF solvent upon incident irradiation.



**Scheme 3.** Proposed mechanism by Muckerman and co-workers [40] for the formation of rhenium carbonate dimer, [Re(bpy)(CO)<sub>3</sub>]<sub>2</sub>(OCO<sub>2</sub>), and CO via photocleavage of Re<sup>0</sup>–Re<sup>0</sup> dimer in CO<sub>2</sub>–saturated DMF solvent.

In a recent combined experimental and computational study, Schneider et al reported the competitive kinetic isotope effects ( $^{13}$ C KIEs) on photocatalytic CO<sub>2</sub> reduction by ReCl(bpy)(CO)<sub>3</sub> in CH<sub>3</sub>CN and DMF solvents in the presence of triethanolamine (TEOA) as a sacrificial reductant [45]. The authors performed DFT calculations at the M06 level of theory coupled with the SMD continuum solvation model to examine the photocatalytic reaction mechanism of CO<sub>2</sub> reduction by ReCl(bpy)(CO)<sub>3</sub> and to compute the  $^{13}$ C KIEs. High precision natural abundance  $^{13}$ C isotope effect measurements resulted in  $^{13}$ C KIEs of 1.0718 and 1.0685, in

CH<sub>3</sub>CN and DMF respectively, which are consistent with the computed <sup>13</sup>C KIEs for CO<sub>2</sub> binding to the one–electron reduced five coordinate Re<sup>I</sup>(bpy•-)(CO)<sub>3</sub> species (Fig. 8). These findings indicate that the first irreversible step for photocatalytic CO<sub>2</sub> reduction in CH<sub>3</sub>CN and DMF solvents is the same and similar reactive intermediates are produced upon reduction in both solvents. In dry solvent conditions, CO<sub>2</sub> binding to the one–electron reduced Re<sup>I</sup>(bpy•-)(CO)<sub>3</sub> species could be followed by dimerization as discussed above, whereas further reduction in the presence of weak Brønsted acids protonation and further reduction steps could lead to formation of CO and H<sub>2</sub>O in a similar fashion to proposed mechanisms for electrocatalytic CO<sub>2</sub> reduction by Mn and Re catalysts.

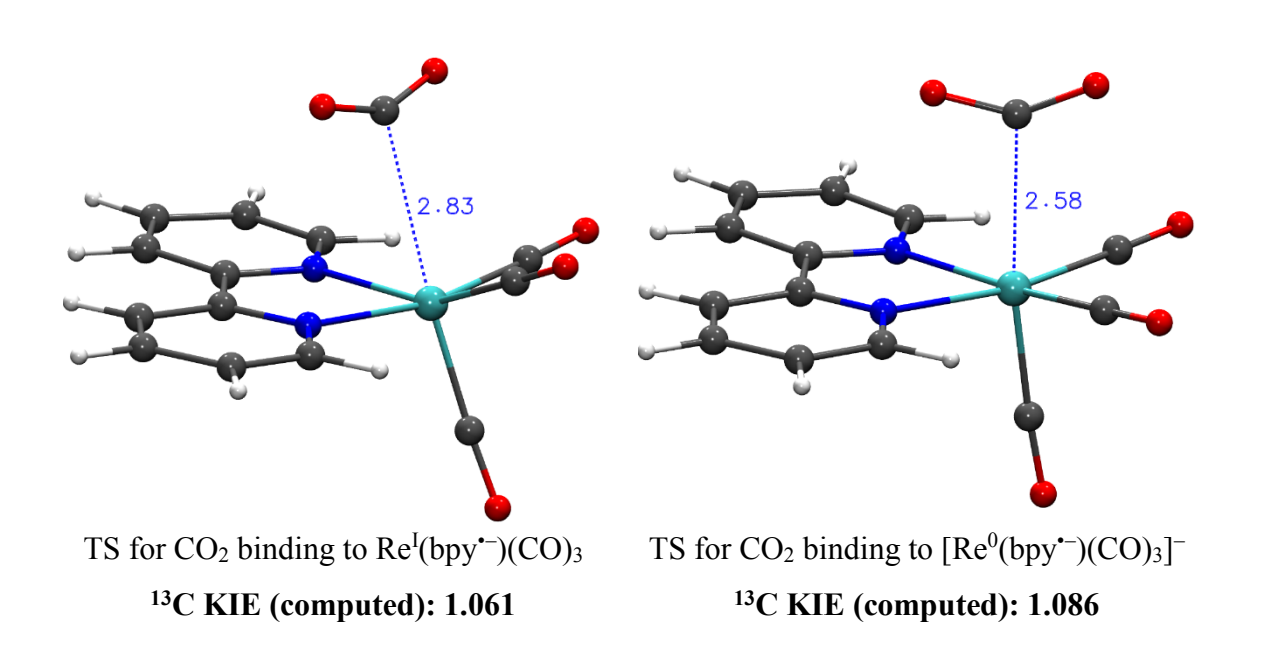


**Figure 8.** Optimized transition state structures for CO<sub>2</sub> binding to Re<sup>I</sup>(bpy•–)(CO)<sub>3</sub> (left) and to [Re<sup>0</sup>(bpy•–)(CO)<sub>3</sub>]<sup>–</sup> (right) and computed <sup>13</sup>C kinetic isotope effects (KIEs). Color code: Re, cyan; C, gray; N, blue; O, red; H, white.

# 3. Thermodynamic aspects of CO<sub>2</sub> reduction in aqueous and non-aqueous solvents

The one-electron reduction of free CO<sub>2</sub> to generate the CO<sub>2</sub> radical anion, CO<sub>2</sub>. (Eq. (1)) is a thermodynamically demanding reaction, which occurs at an equilibrium potential of -1.90 V vs. the standard hydrogen electrode (SHE) in water at pH 7, due, in part, to the large reorganization energy involved [68]. However, through the application of bio-inspired proton-coupled electron transfer (PCET) catalysis, the thermodynamic requirements for CO<sub>2</sub> reduction can be reduced significantly, producing, for example, HCO<sub>2</sub>H at a more modest potential of -0.61 V (Eq. (3)), or CO at -0.52 V (Eq. (4)). To illustrate the diversity and proton dependency of CO<sub>2</sub> redox chemistry, a summary of aqueous equilibrium potentials (vs. SHE) for the pure redox (Eqs. (1) & (2)) and proton-coupled (Eqs. (3) - (8)) conversions of CO<sub>2</sub> to some of its reduced derivatives is provided below for the following reaction conditions: pH = 7; 25 °C; 1 atm of gases (g); 1 M solutes (aq); water as a solvent (l). The data in these equations are from Table 1 in ref. [69] and references therein.

It is important to also recognize that one of the major challenges in identifying a successful homogeneous catalyst for the proton-coupled conversion of CO<sub>2</sub> is product selectivity, especially with respect to the often less thermodynamically demanding and therefore competitive proton reduction reaction, i.e., hydrogen (H<sub>2</sub>) evolution (Eq. (9)) [70]. This is especially challenging for electrocatalytic HCO<sub>2</sub>H production, which shares a metal hydride intermediate with the H<sub>2</sub> evolution mechanistic pathway.

$$2H^{+}_{(aq)} + 2e^{-} \rightleftharpoons H_{2(g)}$$
 -0.41 V vs. SHE @ pH 7 (0.00 V vs. SHE @ pH 0) (9)

Many different CO<sub>2</sub> reduction catalysts have been developed over the years for use in both aqueous and non-aqueous solution. To evaluate catalytic performance and make comparisons between different systems, various parameters are considered, such as overpotential for electrocatalysts  $(\eta)$ , and turnover number (TON), turnover frequency (TOF), and product selectivity for both electro- and photocatalysts [21, 71, 72]. Ideally, a catalyst would be as active as possible (i.e., operate at low  $\eta$  with a high TOF), durable (i.e., exhibit a high TON over extended time), and selective for a single product. For electrocatalysts,  $\eta$  is defined as the difference between the applied potential at the working electrode (E) and the equilibrium potential  $(E_{eq})$  for the electrochemical reaction (Eq. (10)), with  $E_{eq}$  being derived from the standard electrode potential  $(E^{\circ})$  and a potential term  $(\varepsilon_{\rm D})$  related to the activities (concentrations) of reactants and products at the electrode surface [73]. For heterogeneous electrocatalysts  $\eta$  is typically determined from the applied potential, E, that results in a specified current density  $(j, A/cm^2)$ , while for homogeneous catalysts, it has been suggested to use a value of E corresponding to the potential at which the catalytic current is half its maximum value  $(E_{\text{cat/2}})$  [72].

$$\eta = |E_{\text{eq}} - E| \tag{10}$$

Unfortunately, despite the fact that many  $CO_2$  reduction catalysts have been studied in organic solvents such as  $CH_3CN$ , values of  $E^\circ$  for various  $CO_2$  reduction reactions in these solvents are still quite rare, unlike in water where they are well known (Eqs. (1) – (8)). One example is the standard electrode potential for the  $2H^+/2e^-$  proton-coupled reduction of  $CO_2$  to CO in dry  $CH_3CN$  (Eq. (12)), which was recently estimated as -0.13 V vs ferrocenium/ferrocene (Fc<sup>+/0</sup>) by Matsubara *et al.* [69] and -0.12 V vs Fc<sup>+/0</sup> by Appel and Mayer [74]. Thus, in principle, if a catalyst that reduces  $CO_2$  to CO is operated in dry  $CH_3CN$  in the presence of an acid-base buffer of well-defined pH, it should be a simple matter to calculate  $E_{eq}$  from this standard potential using the Nernst equation as shown in Eq. (11). However, it turns out that the calculation of  $E_{eq}$  is slightly more complicated than this (*vide infra*). Unfortunately, the use of acid-base buffers in  $CO_2$  reduction studies has been very limited [47, 69], and thus in many cases the pH of the solution under operating conditions is unknown.

$$E_{\text{eq}} = E^{\circ} - \left(\frac{2.303RT}{2F}\right) \cdot 2 pH \tag{11}$$

$$CO_{2(g)} + 2H^{+}_{(CH3CN)} + 2e^{-} \rightleftharpoons CO_{(g)} + H_{2}O_{(CH3CN)}$$
  $E^{\circ} = -0.13 \text{ V vs. Fc}^{+/0}$  (12)

$$CO_{2(g)} + H_2O_{(CH3CN)}$$
  $\Rightarrow$   $H^+_{(CH3CN)} + HCO_3^-_{(CH3CN)}$   $pK_{a(app)} = 23.4 (1 M H_2O)$  (13)

$$3CO_{2(g)} + H_2O_{(CH3CN)} + 2e^- \rightleftharpoons CO_{(g)} + 2HCO_3^-_{(CH3CN)}$$
  $E^{\circ} = -1.55 \text{ V vs. Fc}^{+/0} (1 \text{ M H}_2O)$  (14)

The situation becomes more complicated when H<sub>2</sub>O is added to an organic solvent as a proton source for CO<sub>2</sub> reduction. In this case, an apparent acid-base equilibrium is setup between the dissolved CO<sub>2</sub> and H<sub>2</sub>O (Eq. (13)), releasing protons, the concentration of which depends on

the concentration of added H<sub>2</sub>O. The net CO<sub>2</sub> reduction reaction in the presence of H<sub>2</sub>O (Eq. (14)) is thus a combination of the electrode reaction in Eq. (12) and the CO<sub>2</sub> + H<sub>2</sub>O apparent acid-base equilibrium (Eq. (13)), with bicarbonate (HCO<sub>3</sub><sup>-</sup>) as a byproduct. Savéant and coworkers made initial estimates of E° for this CO<sub>2</sub> reduction reaction in wet CH<sub>3</sub>CN and DMF [75], which involved the use of a DFT-calculated value of a water transfer energy to estimate the apparent p $K_a$  for Eq. (13). However, using the technique of isothermal titration calorimetry (ITC), this apparent  $pK_a$  was experimentally-determined by Matsubara et al. in wet  $CH_3CN$ containing 1 M H<sub>2</sub>O (p $K_a = 23.4 \pm 0.1$ ), permitting a more accurate value of  $E^{\circ}$  to be estimated for this particular concentration of H<sub>2</sub>O in CH<sub>3</sub>CN, i.e.,  $E^{\circ}_{Eq~(14)~(1M~H_2O)} = -1.55~V~vs.~Fc^{+/0}~[73].$ Unfortunately though, researchers have used a wide range of H<sub>2</sub>O concentrations for CO<sub>2</sub> reduction studies in wet CH<sub>3</sub>CN. To address this, Matsubara very recently applied the concept of the unified pH scale to allow an estimation of  $E^{\circ}$  for Eq. (14) in wet CH<sub>3</sub>CN over a wide range of  $H_2O$  concentrations, from 0.50 - 55.3 M (1–100 vol %  $H_2O$ ) [73]. As can be seen in Fig. 9,  $E^{\circ}$  is very sensitive to the water content, spanning a range of 0.5 V. In addition, Matsubara formulated an equation that allows  $E_{eq}$  to be estimated for the electrocatalytic reduction of  $CO_2$  to CO in wet CH<sub>3</sub>CN (Eq. (14)) by bulk electrolysis using a homogeneous catalyst in solution when the applied potential (E) is sufficiently more negative than  $E_{\text{cat/2}}$  (Eq. (15)). As can be seen in Eq. (15),  $E^{\circ}$  is modified by an expression that contains parameters that include the concentration of the catalyst  $(c_0^*)$ , the concentration of CO in the solution when equilibrated with CO at 1 bar in the gas phase ( $c_{CO}^{eq}$ ), and the diffusion coefficients (D) of CO, HCO $_3$ -, CO $_2$  and the catalyst. For situations where E is similar to  $E_{cat/2}$ , a more complex form of Eq. (15) should be used (see Eq. (S20) in ref. [73]). A similar equation was also developed for bulk electrolysis with a surfaceimmobilized catalyst.

$$E_{eq} \approx E^{o} + \frac{RT}{2F} ln \left[ \frac{27}{32} \frac{c_{CO}^{eq}}{(c_{O}^{*})^{3}} \frac{D_{CO}(D_{HCO_{3}^{-}})^{2}}{(D_{O}D_{CO_{2}})^{3/2}} \right]$$
(15)

Matsubara's work has now opened up the possibility of making fair comparisons of the catalytic efficiencies of CO<sub>2</sub>-to-CO reduction catalysts under various solution conditions in wet CH<sub>3</sub>CN, and such a comparison that includes some Mn-based catalysts was made in ref. [73]. In principle, an equation similar to Eq. (15) could be developed for the reduction of CO<sub>2</sub> to CO in dry CH<sub>3</sub>CN in the presence of an acid-base buffer (Eq. (12)), allowing for an accurate estimation of overpotentials under these conditions. We expect that the standard potentials for other types of CO<sub>2</sub> reduction reactions in various aqueous organic solvents will be estimated in the future using Matusbara's method, finally allowing a true comparison of the efficiencies of all reported and future CO<sub>2</sub> reduction electrocatalysts.

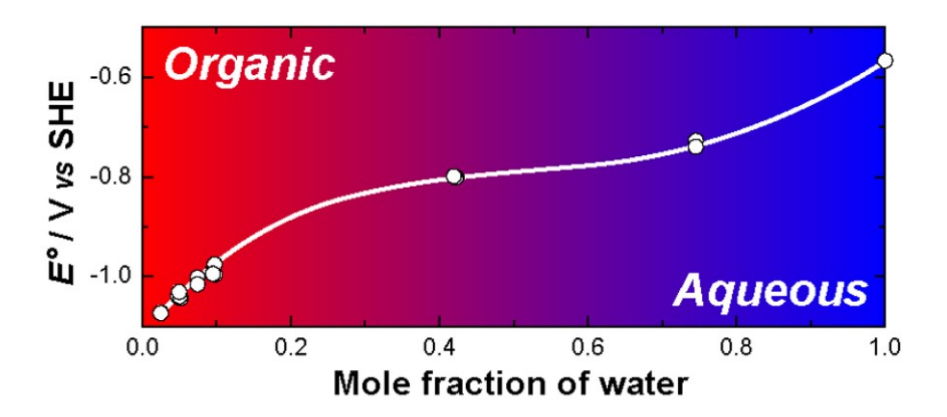


**Figure 9:** Plot of the standard electrode potential for the reduction of CO<sub>2</sub> to CO in wet CH<sub>3</sub>CN (Eq. (15)) as a function of the water content. The potentials are shown here versus the standard hydrogen electrode (SHE), but they are also reported versus Fc<sup>+/0</sup> in the original publication. Reproduced with permission from ref. [73]. Copyright 2017 American Chemical Society.

3.1 Case study: A comparison of overpotentials for analogous Mn- and Re-based CO<sub>2</sub> reduction catalysts

Taking advantage of Matsubara's approach, we have included below a direct comparison of the Re and Mn complexes **5** and **6** for the electrocatalytic reduction of CO<sub>2</sub> to CO in a 0.1 M Bu<sub>4</sub>NPF<sub>6</sub> CH<sub>3</sub>CN electrolyte with 2.78 M (5%) added H<sub>2</sub>O (Fig. 10).

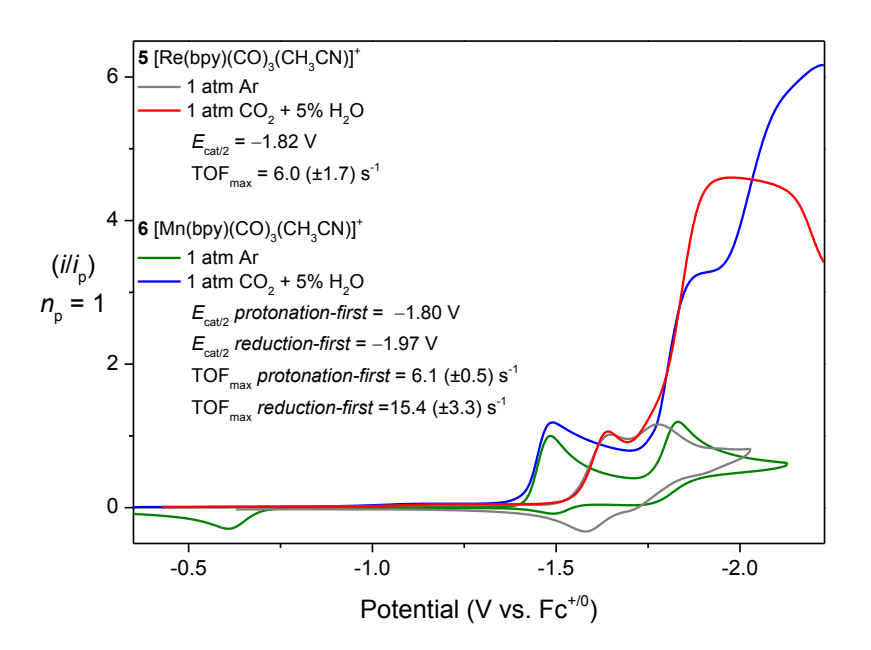


**Figure 10:** Plot of linear sweep voltammetry data under 1 atm of CO<sub>2</sub> in a 0.1 M Bu<sub>4</sub>NPF<sub>6</sub> acetonitrile electrolyte with 2.78 M (5%) added H<sub>2</sub>O for **5** (–) and **6** (–). All data was recorded at a scan rate of  $\upsilon = 0.10$  V s<sup>-1</sup> and calibrated internally using the Fc<sup>+/0</sup> pseudo-reference. Also included are reference cyclic voltammetry data under 1 atm of argon in a 0.1 M Bu<sub>4</sub>NPF<sub>6</sub> acetonitrile electrolyte for **5** (–;  $E_{pc} = -1.65$  V & -1.78 V) and **6** (–;  $E_{pc} = -1.48$  V & -1.83 V). Both *protonation-first* ( $E_{cat/2} = -1.80$  V) and *reduction-first* ( $E_{cat/2} \approx -1.97$  V) catalytic waves are exhibited by **6**;  $E_{cat/2}$  for the Mn *reduction-first* pathway was estimated by deconvolution of both catalytic waves. A single catalytic wave is exhibited by **5** ( $E_{cat/2} = -1.82$  V). Maximum turnover

frequencies (TOF<sub>max</sub>) were determined following scan-rate analysis and identification of steadystate catalytic conditions, apart from the TOF<sub>max</sub> value for the *protonation-first* pathway of  $\bf 6$  which was estimated by foot-of-the-wave analysis.

Comparing just the reference cyclic voltammetry data, recorded under argon, the first one-electron reduction of the Mn complex **6** at -1.48 V vs. Fc<sup>+/0</sup> occurs 0.17 V more positive than that of the Re(I) analogue. While both reductions are formally assigned to the bpy/bpy<sup>--</sup> reduction, the positive shift of **6** is attributed to the lower-lying energy of the adjacent valence *d*-shell of the Mn(I) center relative to Re(I). This reduction is irreversible for **6** due to rapid dissociation of the CH<sub>3</sub>CN ligand and formation of the neutral pentacoordinate Mn(0) metalloradical species, [Mn(bpy)(CO)<sub>3</sub>], which subsequently undergoes rapid dimerization to form [Mn(bpy)(CO)<sub>3</sub>]<sub>2</sub> whose oxidation is observed upon the reverse scan in Fig. 10 at -0.61 V vs. Fc<sup>+/0</sup>. In contrast, the first one-electron reduction wave for **5** is quasi reversible, characterized by a redox couple of -1.61 V vs. Fc<sup>+/0</sup> ( $E_{pc} = -1.65$  V,  $\Delta E_p = 0.080 \pm 0.005$  V) consistent with the predicted stability of the neutral six-coordinate, Re(bpy)(CO)<sub>3</sub>(CH<sub>3</sub>CN) intermediate (see Section 2.1). Subsequent reduction to the five-coordinate, two-electron reduced active catalytic species, [M(bpy)(CO)<sub>3</sub>]<sup>-</sup> is evident by a second irreversible one-electron cathodic wave at -1.83 V and -1.78 V vs. Fc<sup>+/0</sup> for Mn and Re, respectively.

Under 1 atm of CO<sub>2</sub> in the absence of any added proton source, no catalytic current is observed for either complex. While this is unusual for such Re-based polypyridyl complexes, it is consistent with the electron deficient character of **5** relative to its neutral chloride analogue and complexes containing more electron rich polypyridyl ligands [12, 25-27, 76]. Under

electrocatalytic conditions (1 atm CO<sub>2</sub> and 2.78 M (5%) added H<sub>2</sub>O), catalytic current is observed for both the Mn and Re complexes. The Mn complex **6** exhibits both *protonation-first* ( $E_{\text{cat/2}} = -1.80 \text{ V}$ ) and *reduction-first* ( $E_{\text{cat/2}} \approx -1.97 \text{ V}$ ) catalytic waves, while just a single catalytic wave is exhibited by **5** ( $E_{\text{cat/2}} = -1.82 \text{ V}$ ). Under these catalytic conditions with 1 mM catalyst concentration, having determined diffusion coefficients of 3.71 x 10<sup>-5</sup> cm<sup>2</sup> s<sup>-1</sup> and 1.89 x 10<sup>-5</sup> cm<sup>2</sup> s<sup>-1</sup> for **6** and **5**, respectively,  $E_{\text{eq}}$  was calculated to be -1.21 V and -1.20 V vs. Fc<sup>+/0</sup>, respectively using Eq. (S20) in ref. [73] and a value of  $E^{\circ} = -1.43 \text{ V}$  vs. Fc<sup>+/0</sup> obtained from a fit of the  $E^{\circ}$  data reported in ref. [73].

Using Eq. (10), the overpotentials for the *protonation-first* and *reduction-first* pathways for **6** are therefore  $\eta = 0.59$  V and 0.76 V, respectively, representing a saving of 0.17 V by following the *protonation-first* pathway. In contrast, **5** exhibits an overpotential of  $\eta = 0.62$  V, which is just 0.03 V more than for the *protonation-first* pathway for the Mn-based catalyst. It should be noted that these overpotentials are specific to the experimental conditions applied in Fig. 10 and may likely vary with p $K_a$  of the proton source and pH of the solution, as discussed above.

# 4. Experimental mechanistic investigations of CO2 reduction by Mn-based complexes

All catalysts operate through a series of reaction steps that involve intermediates in various oxidation states, and their reactions with substrate molecules (CO<sub>2</sub> in the case of this review), and sometimes with other species such as Brønsted acids. In order to develop catalysts that enhance a desired reactivity while suppressing unwanted side reactions and decomposition pathways, it is critically important that the catalytic mechanism is fully understood, including the structure and reactivity of individual catalytic intermediates. The knowledge gained from such

mechanistic investigations can then be applied to the design of improved catalysts. Often, a combined theoretical and experimental approach is the most successful strategy, with theoretical predictions guiding experiments. A discussion of theoretical methods applied to CO<sub>2</sub> reduction catalysis was provided in Section 2. In this section, we will highlight a variety of powerful experimental techniques that are often employed to obtain mechanistic information about CO<sub>2</sub> reduction catalysis by Mn-based complexes. We will begin with a brief overview of voltammetric techniques, and then focus on spectroscopic methods that can be used to identify and directly monitor the reactivity of catalytic intermediates. Selected examples related to CO<sub>2</sub> reduction catalysis with Mn-based complexes will be highlighted, with an emphasis on infrared (IR) spectroscopic techniques, and other structurally-sensitive methods.

#### 4.1 Electrochemical methods

A powerful and commonly used method for mechanistic investigations of CO<sub>2</sub> reduction catalysis is electrochemistry. A large variety of electrochemical techniques are available, ranging from cyclic voltammetry and bulk electrolysis to more advanced experiments such as rotating disk electrode (RDE) and rotating ring-disk electrode (RRDE) electrochemistry. These techniques can be used to obtain both thermodynamic and kinetic information about catalytic reaction steps, and can also be used to help identify catalytic intermediates and products.

#### 4.1.1 Voltammetry

The accurate determination of an electrocatalyst's overpotential ( $\eta$ ) at a given applied potential (E) from voltammetry data has already been discussed in Section 3. In addition to elucidating the basic thermodynamic properties of a catalyst, time-dependent voltammetric

sweep methods, specifically cyclic and linear sweep voltammetries, are also a powerful tool for extracting kinetic information about a catalytic cycle. This topic has been covered in significant detail in recent articles, some of which are specifically focused on the reduction of CO<sub>2</sub> [21, 71, 77]. Thus, the major concepts are simply summarized here with specific reference to Mn-based catalysts.

Prior to electrocatalysis studies, cyclic voltammetry is initially used to determine the reduction potentials and non-catalytic Faradaic current responses  $(i_p)$  of homogeneous complexes under inert conditions. For homogeneous Mn-based molecular catalysts, this typically requires an inert atmosphere of argon or nitrogen and a non-protic electrolyte solvent, such as 0.1 M tetrabutylammonium hexafluorophosphate (Bu<sub>4</sub>NPF<sub>6</sub>) in dry CH<sub>3</sub>CN. Commonly, for the majority of Mn(I) tricarbonyl polypyridyl complexes, the observed current-voltage profile follows an electrochemical-electrochemical (ECE) mechanism as described in the catalyst activation steps of Scheme 1, i.e., two sequential irreversible one-electron reduction steps are often observed, ultimately generating a pentacoordinate anion, e.g., [Mn<sup>0</sup>(bpy•– )(CO)<sub>3</sub>]<sup>-</sup>. In the case of complexes with 6,6'-disubstituted bipyridine ligands [47, 64] and some other systems [78-80], the same ECE mechanism occurs but it is condensed into a single, concerted two-electron event. Upon replacing the inert gas with 1 atm of CO<sub>2</sub>, but in the absence of a proton source no change in the current-voltage response is observed. Only upon introduction of the CO<sub>2</sub> substrate with concurrent addition of an external Brønsted acid co-reagent is catalytic current ( $i_{cat}$ ) observed, initiated by two-electron reduction of the Mn complex.

Kinetic analysis of the peak  $i_{\text{cat}}$  value is required to extract the maximum turnover frequency (TOF<sub>max</sub> – sometimes referred to as the observed ( $k_{\text{obs}}$ ), or apparent ( $k_{\text{app}}$ ) rate constant) of the catalyst. According to Scheme 1, the rate equation for the electrocatalytic reduction of CO<sub>2</sub> to CO by a homogeneous Mn-based molecular catalyst can be represented by Eq. (16) where  $k_{\text{cat}}$  represents the intrinsic rate constant of the catalyst.

$$rate = TOF_{max} = k_{cat}[CO_2][H^+]^2$$
 (16)

The direct measurement of  $k_{\text{cat}}$  by voltammetry is not possible. However, under pseudo first-order conditions, where an excess of CO<sub>2</sub> and Brønsted acid exist at low catalyst loading (typically 1 mM), TOF<sub>max</sub> can be determined. Unfortunately, despite the fact that the solubility of CO<sub>2</sub> in CH<sub>3</sub>CN ( $\sim 0.28$  M / atm [81]) is much greater than in water, it is still limited, which can hinder the establishment of pseudo first-order conditions for an efficient catalyst due to a depletion of [CO<sub>2</sub>] within the electrochemical double layer at the electrode surface during analysis. Thus, to determine TOF<sub>max</sub> for an efficient electrocatalyst for CO<sub>2</sub> reduction by voltammetry, an appropriate scan rate threshold must be identified, above which any dependence on the mass transfer diffusion of CO<sub>2</sub> from the bulk electrochemical solution is negated. This requires the characterization of TOF<sub>max</sub> at increasing scan rates until a steady-state current plateau is reached and the catalytic rate becomes independent of the applied scan rate (Fig. 11). Under these ideal steady-state conditions, an *s*-shaped current response is observed in cyclic voltammetry where the catalytic current of the reverse-scan almost overlays that of the forward scan. For example, the steady-state voltammetric response of catalyst 13 [47] is presented in Fig.

11 at a scan rate of  $0.10~V~s^{-1}$  in a  $0.1~M~Bu_4NPF_6~CH_3CN$  electrolyte under 1 atm  $CO_2$  in the presence of  $6.33~M~H_2O$ .

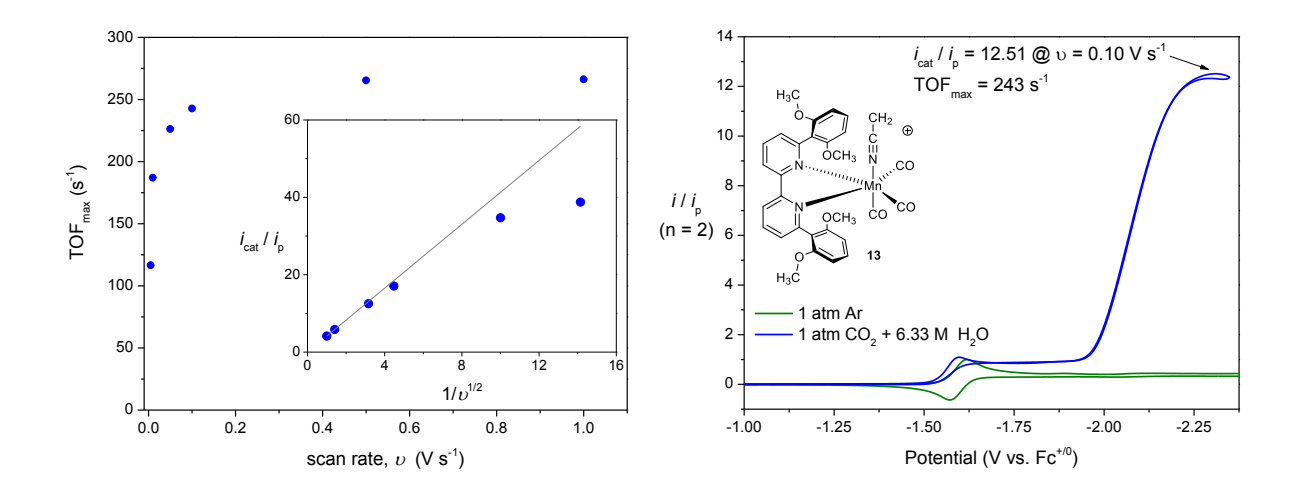


Figure 11: (Left) Scan-rate dependence of the maximum turnover frequency (TOF<sub>max</sub>) observed for 13 recorded in a 0.1 M Bu<sub>4</sub>NPF<sub>6</sub> CH<sub>3</sub>CN electrolyte under 1 atm CO<sub>2</sub> in the presence of 6.33 M H<sub>2</sub>O. Steady-state kinetic conditions are identified above a threshold scan rate of  $\upsilon = 0.10 \text{ V s}^{-1}$  by a plateau of the TOF<sub>max</sub> response. The inset shows the predicted linear plot of ' $i_{cat}/i_p$  vs.  $1/\upsilon^{1/2}$  where the data deviates from linearity at scan rates of  $\upsilon < 0.10 \text{ V s}^{-1}$ . (Right) An overlay of the Faradaic and catalytic responses for 13 recorded in a 0.1 M Bu<sub>4</sub>NPF<sub>6</sub> CH<sub>3</sub>CN electrolyte under 1 atm of argon (–) and 1 atm of CO<sub>2</sub> + 6.33 M H<sub>2</sub>O (–), respectively. Both voltammograms were recorded at a scan rate of  $\upsilon = 0.10 \text{ V s}^{-1}$ . Note the *s*-shaped curve of the catalytic response indicative of steady-state catalysis conditions. A maximum  $i_{cat}/i_p$  ratio of 12.51 is exhibited, corresponding to a TOF<sub>max</sub> of 243 s<sup>-1</sup> consistent with the adjacent plots.

When characterizing a catalyst, we recommend the calculation of  $TOF_{max}$  at multiple scan rates beyond the threshold for steady-state conditions and reporting the mean  $TOF_{max}$  with a standard deviation. To calculate  $TOF_{max}$  at any given scan rate which exhibits steady-state conditions, the ratio of  $i_{cat}/i_p$  need only be measured and the following equation can be used,

$$TOF_{max} = 0.1992 \left(\frac{Fv}{RT}\right) \left(\frac{n_p^3}{n_{cat}^2}\right) \left(\frac{i_{cat}}{i_p}\right)^2$$
 (17)

where F is the Faraday constant (96,485 s A mol<sup>-1</sup>),  $\upsilon$  is the scan rate (V s<sup>-1</sup>), R is the universal gas constant (8.3145 V A s K<sup>-1</sup> mol<sup>-1</sup>), T is the temperature (K),  $n_p$  is the number of electrons involved in the non-catalytic Faradaic current response (responsible for  $i_p$ ), and  $n_{cat}$  is the number of electrons required for catalysis (2 electrons for the reduction of CO<sub>2</sub> to CO). It should be strongly emphasized that the application of Eq. 17 must be validated by establishing steady-state catalytic conditions, as discussed above and illustrated in Fig. 11, otherwise the calculated TOF does not represent a maximum value and is likely severely underestimated. In fact, Eq. 17 is derived only by assuming steady-state conditions consistent with an  $E_rC_{cat}$  mechanism describing only the rate-determining step of the catalytic cycle under pseudo first-order conditions [71, 82, 83]. It should also be appreciated that when extracting TOF<sub>max</sub> using voltammetry data in this manner the value obtained is representative of only the small portion of activated catalysts within the diffusion layer at the electrode surface.

Thus, where steady-state catalytic conditions cannot be established,  $TOF_{max}$  cannot be experimentally determined. In the specific case of characterizing a very efficient catalyst where pseudo first-order conditions cannot be established, as the depletion of  $[CO_2]$  in the

electrochemical double layer cannot be ignored, Saveant and co-workers developed the foot-of-the-wave analysis (FOWA) method to estimate TOF<sub>max</sub> [21, 71, 75, 84]. FOWA effectively extrapolates the slope of the catalytic current onset (quite literally the foot of the catalytic wave) to estimate TOF<sub>max</sub>, which is otherwise unattainable due to the rate limiting CO<sub>2</sub> concentration. Practically, FOWA requires a plot of ' $i_{cat}/i_p$  vs.  $1/(1 + \exp\left[\frac{F}{RT}(E - E_{cat}^0)\right])$ ', according to Eq. 18 where E is the applied potential, i.e. the entire x-axis of a voltammetry plot, and  $E_{cat}^0$  is the standard reduction potential for activation of the active catalyst (determined under inert non-catalytic conditions). This gives rise to a linear plot consisting of a slope (m) described by Eq. 19, from which TOF<sub>max</sub> can be extracted.

$$\frac{i_{cat}}{i_p} = \frac{2.24\sqrt{\left(\frac{RT}{Fv}\right)\text{TOF}_{max}}}{1 + \exp\left[\left(\frac{F}{RT}\right)(E - E_{cat}^0)\right]} \left(\frac{n_{cat}}{n_p^{3/2}}\right)$$
(18)

$$m = 2.24 \sqrt{\left(\frac{RT}{Fv}\right) \text{TOF}_{\text{max}}} \left(\frac{n_{\text{cat}}}{n_p^{3/2}}\right)$$
 (19)

We recently applied FOWA to estimate TOF<sub>max</sub> for the *protonation-first* pathway of catalyst 13 as discussed above. In the presence of a Brønsted acid that has a p $K_a$  in CH<sub>3</sub>CN lower than that of H<sub>2</sub>O, such as phenol, the *protonation-first* pathway is evident as a more positive catalytic wave overlapping with that of the *reduction-first* pathway. A pure value of  $i_{cat}$  solely for the *protonation-first* pathway cannot be determined due to the underlying current onset for the more negative *reduction-first* catalytic response. FOWA allowed TOF<sub>max</sub> to be estimated as a mean value of  $138 \pm 4$  s<sup>-1</sup> over a range of scan rates from 0.5 to 1.0 V s<sup>-1</sup>. An example of the FOWA analysis for 13 recorded at 0.75 V s<sup>-1</sup> is presented in Fig. 12.

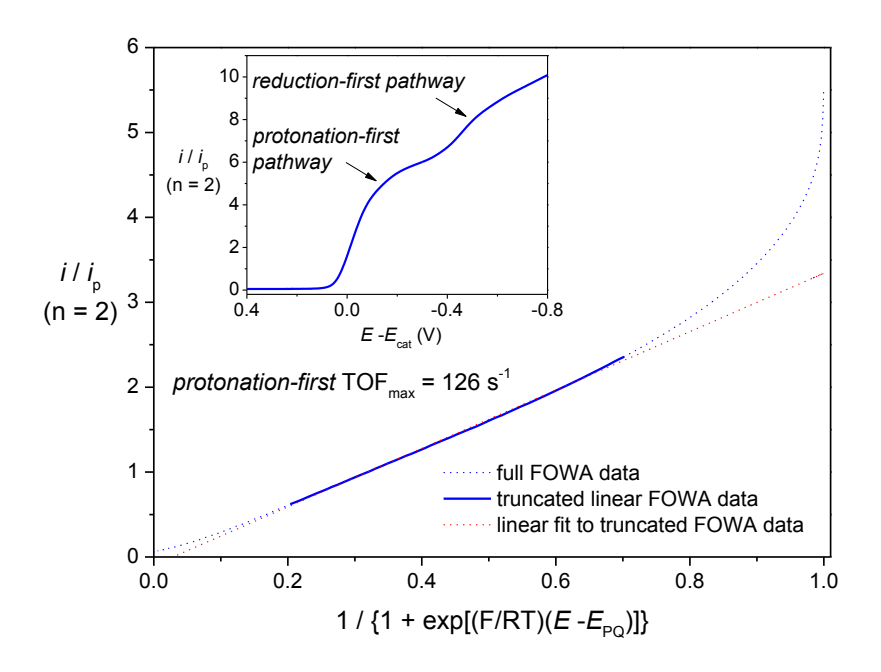


**Figure 12.** Foot-of-the-wave analysis (FOWA) for the *protonation-first* pathway of catalyst **13** recorded in a 0.1 M Bu<sub>4</sub>NPF<sub>6</sub> CH<sub>3</sub>CN electrolyte under 1 atm CO<sub>2</sub> in the presence of 1.37 M phenol at a scan rate of  $\upsilon = 0.75$  V s<sup>-1</sup>. A positive hysteresis of the FOWA plot (full FOWA data) is attributed to the underlying onset current for the *reduction-first* catalytic pathway. Truncating the FOWA data to a linear portion and extrapolating a linear fit allows estimation of TOF<sub>max</sub> from the linear slope. The inset shows the  $i_p$  normalized current response plotted vs  $E - E_{\text{cat}}^0$  where distinct catalytic current waves can be identified for both the *protonation-first* and *reduction-first* catalytic pathways.

#### 4.1.2 Controlled potential (bulk) electrolysis

After voltammetric techniques have been used to identify the applied potential(s) at which CO<sub>2</sub> reduction catalysis is believed to occur, it is critically important that these are followed up with controlled potential (bulk) electrolysis (CPE or BE) experiments with product analysis. Without a CPE experiment, it is impossible to claim from CV data alone that the observed

catalytic current is generated by a specific catalyzed reaction, e.g. the reduction of CO<sub>2</sub> to CO or HCO<sub>2</sub>H, since other competing processes, including H<sub>2</sub> production, could be occurring. In a typical CPE experiment, a two-compartment electrochemical cell is used so that the oxidative processes occurring at the counter electrode does not contribute to the products formed at the working electrode in the main compartment, and these desired reduction products are not oxidized at the counter electrode. The cell is purged with CO<sub>2</sub>, sealed, and then the working electrode is held at a fixed potential for a given amount of time.

The products of catalytic CO<sub>2</sub> reduction are quantitatively analyzed by various means during and/or after CPE. For example, samples of the head space gas are often analyzed by gas chromatography (GC) to quantify CO and H<sub>2</sub> production. Liquid-phase products, e.g. HCO<sub>2</sub>H, are often analyzed by NMR, GC-MS, or ion chromatography methods. Once the amount of each product is quantified, the TON can be calculated based on the initial concentration of the precatalyst (see Section 5.2.4 for a definition of TON, which is the same for both electro- and photocatalytic processes). The amount of charge (Q) that passes through the cell during CPE is also recorded, and from the amount of each product formed, a Faradaic efficiency (FE) for each product can then be determined based on the CO<sub>2</sub> reduction reaction that is occurring. For example, for the two-electron reduction of CO<sub>2</sub> to CO (Eq. (4)), a 100% FE for CO would correspond to 1 mole of CO produced per 2 moles of charge passed. Finally, we would strongly encourage readers to perform control CPE experiments with isotopically labeled <sup>13</sup>CO<sub>2</sub> to determine that the labeled carbon carries through to the reduction products observed, thus confirming that the products are indeed derived from the added CO<sub>2</sub>. This is particularly important for immobilized catalysts where more exotic electrode materials, such as Nafion®

membranes or various forms of carbon-based or metal oxide supports, are often used, since in these cases it is conceivable that even small amounts of carbon-based impurities could be responsible, at least in part, for the CO<sub>2</sub> reduction products observed. We note that since CO is ultimately produced by ejection from the tetracarbonyl intermediate (Scheme 1), some isotopic scrambling could possibly occur. However, this would only ever be a potential issue if the TON is very low (<~10).

#### 4.1.3 Infrared spectroelectrochemistry (IR-SEC)

If catalytic intermediates are easily prepared, for example by chemical synthesis, reaction with chemical oxidants/reductants, or by electrolysis, and they are sufficiently long lived, then conventional spectroscopy techniques, such as IR, UV/Vis, NMR, etc. can be applied. One such method that has proved to be particularly powerful for investigating CO<sub>2</sub> reduction catalysis is infrared spectroelectrochemistry (IR-SEC). In this technique, stable or metastable species generated at a working electrode held at a particular potential are probed in-situ by fouriertransform infrared (FTIR) spectroscopy in a specially designed IR cell containing working, counter, and reference electrodes. In some cases, the working electrode is a metallic mesh inside a transmission IR cell, through which the IR beam can transmit (a so-called optically transparent thin layer electrochemical or OTTLE cell), while in other cases it is a metallic or glassy carbon disc, off which the IR beam is reflected in a specular reflectance-type cell [32]. IR-SEC takes advantage of the structural specificity of IR spectroscopy and the ability to prepare successive catalytic intermediates simply by gradually stepping the potential of the working electrode. We note that in some cases, UV/Vis-SEC has also proved to be a powerful technique for monitoring CO<sub>2</sub> reduction processes.

Early pioneering IR-SEC work on the well-known family of  $[Re(\alpha\text{-diimine})(CO)_3L]^{0/+}$  CO<sub>2</sub> reduction catalyst precursors, in some instances in combination with UV/Vis-SEC experiments [33, 85, 86], provided a comprehensive picture of the initial reduction events, including the loss of ligand L upon one-electron reduction and the existence of one- and two-electron pathways for the CO<sub>2</sub> reduction process, involving key intermediates such as  $[Re(\alpha\text{-diimine})(CO)_3]^*$ ,  $[Re(\alpha\text{-diimine})(CO)_3]^-$ , and the metallocarboxylic acid species,  $[Re(\alpha\text{-diimine})(CO)_3]$  (CO<sub>2</sub>H)]. However, in the case of the Re-CO<sub>2</sub>H species,  $\nu$ (OCO) bands of the bound CO<sub>2</sub> moiety could not be assigned due to overlap with the strong IR band of carbonate ion,  $CO_3^{2-}$ . These experiments were made possible by the sensitivity of the  $\nu$ (CO) frequencies of the carbonyl ligand stretching vibrations to both the electron density and the structural arrangement of ligands at the metal center, permitting relatively facile identification of intermediates.

Various first-row transition metal complex  $CO_2$  reduction catalyst precursors have also been studied by IR-SEC [87, 88]. Even the Mn-based versions of the Re-based catalyst precursors, i.e., the  $[Mn(\alpha\text{-diimine})(CO)_3L]^{0/+}$  complexes, were the subject of early IR-SEC investigations [89, 90], with intermediates such as the Mn–Mn bonded dimer,  $[Mn(\alpha\text{-diimine})(CO)_3]_2$ , and the two-electron reduced species,  $[Mn(\alpha\text{-diimine})(CO)_3]_-$ , having been observed. An important mechanistic difference between the Mn- and Re-based complexes that was highlighted by the various IR-SEC studies [90, 91] is that in the case of the Re complexes, one-electron reduction results in an observable six-coordinate anion, e.g.,  $[ReCl(bpy^-)(CO)_3]_-$ , which slowly ejects the sixth ligand, e.g.,  $Cl_-$ , to form an observable neutral radical intermediate, which will be in equilibrium with a Re–Re bonded dimer to varying degrees depending on the functionalization

of the bpy ligand. Further reduction ultimately results in the [Re(bpy)(CO)<sub>3</sub>]<sup>-</sup> active catalyst. However, for the Mn complexes, ejection of the sixth ligand upon one-electron reduction, and subsequent Mn–Mn dimerization, both occur on such a fast timescale that no intermediates prior to the dimer are observed by IR-SEC. In addition, the dimerization is quantitative in the case of Mn, whereas the radicals and dimer are in equilibrium in the case of Re (see Section 2.1).

At the time that the Mn-based complex **4** was originally studied by IR-SEC, it was thought not to be capable of acting as a CO<sub>2</sub> reduction catalyst [33], since electrochemical experiments in the presence of Brønsted acids were never attempted. This discovery was finally made some years later by Chardon-Noblat, Deronzier, and co-workers in their study of the reduction of CO<sub>2</sub> by catalysts **2** and **3** in CH<sub>3</sub>CN in the presence of 5% H<sub>2</sub>O [35]. In this pioneering work, it was actually UV/Vis-SEC that was used to characterize the formation of the dimer, [Mn (α-diimine)(CO)<sub>3</sub>]<sub>2</sub> upon one-electron reduction, followed by the production of the two-electron reduced [Mn(α-diimine)(CO)<sub>3</sub>]<sup>-</sup> active catalytic species after reduction of the dimer at more negative potential. This opened the door for a number of recent investigations of Mn-based CO<sub>2</sub> reduction catalyst precursors, with IR-SEC being a key mechanistic tool.

Kubiak's group has made a major contribution to this field, developing a series of Mn-based  $CO_2$  reduction electrocatalyst precursors. Their initial work on the dtbpy complex 7 demonstrated the power of IR-SEC for identifying the various reduced forms of the catalyst via the  $\nu(CO)$  vibrations, up to the two-electron reduced active catalytic species, [Mn(dtbpy)(CO)<sub>3</sub>]<sup>-</sup> (see Fig. 13) [57]. This latter species was also sufficiently stable in the presence of a potassium crown ether to allow an X-ray crystal structure to be obtained.

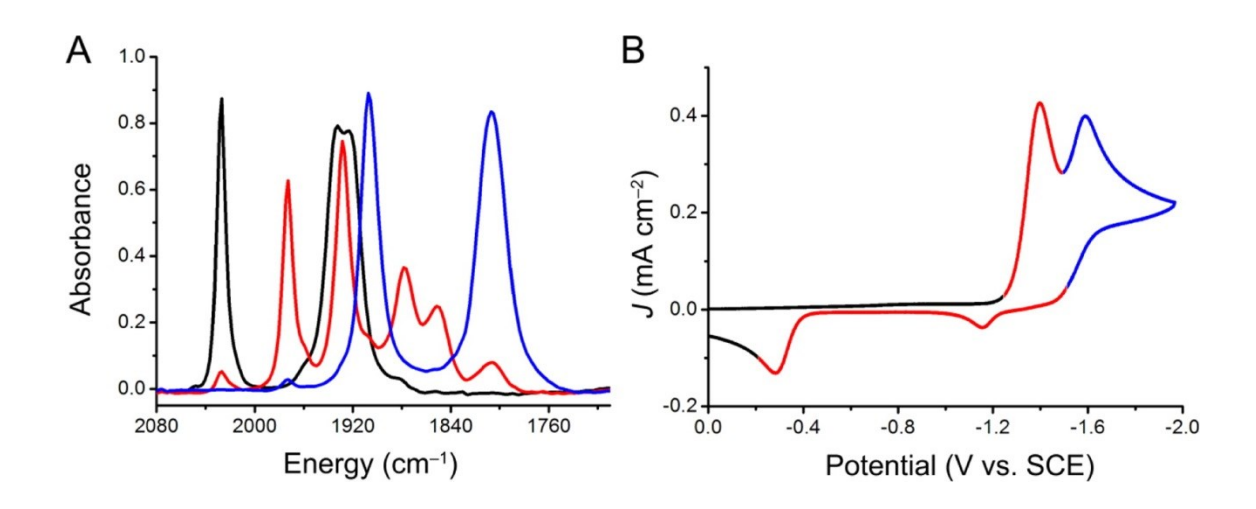


**Figure 13:** (A) IR-SEC of **7** (black) under N<sub>2</sub> in CH<sub>3</sub>CN, showing two major species as the potential is increased cathodically: [Mn(dtbpy)(CO)<sub>3</sub>]<sub>2</sub> (red), and [Mn(dtbpy)(CO)<sub>3</sub>]<sup>-</sup> (blue). (B) CV of **7** under Ar in CH<sub>3</sub>CN, showing correlation to the species seen in the IR-SEC experiment. Reproduced with permission from ref. [57]. Copyright 2014 American Chemical Society.

Later, Kubiak and co-workers added sterically demanding mesityl groups at the 6,6′-positions of the bpy ligand (Fig. 6) [64]. The presence of these groups prevented Mn–Mn dimerization from occurring from **14** and **15**, promoting disproportionation of the one-electron reduced intermediate, [Mn(mes<sub>2</sub>bpy)(CO)<sub>3</sub>]<sup>0</sup>, to produce the two-electron reduced [Mn(mes<sub>2</sub>bpy)(CO)<sub>3</sub>]<sup>-</sup> active catalytic species at the potential of the first reduction. In addition to both of these species being observed by IR-SEC, in the presence of CO<sub>2</sub> and methanol as a Brønsted acid, v(CO) bands at 2006 and 1907 cm<sup>-1</sup> were assigned to the metallocarboxylic acid intermediate, Mn(mes<sub>2</sub>bpy)(CO)<sub>3</sub>(CO<sub>2</sub>H) that results from the reaction of [Mn(mes<sub>2</sub>bpy)(CO)<sub>3</sub>]<sup>-</sup> with CO<sub>2</sub>/H<sup>+</sup>. Unfortunately though, the v(OCO) vibration of the bound CO<sub>2</sub>H moiety (expected to appear between 1700 and 1500 cm<sup>-1</sup>) could not be observed, presumably due to either a small

accumulation of the species or spectral interference by methanol. Despite the fact that the Mn–CO<sub>2</sub>H species is formed at the potential of the first reduction, the IR-SEC data indicated that catalysis does not occur until this species is reduced at ~400 mV more negative potential, which induces the ejection of OH<sup>-</sup> (in the form of H<sub>2</sub>O upon reaction with H<sup>+</sup>), and subsequent CO elimination from the resulting tetracarbonyl species. In related work, IR-SEC was used to characterize the intermediates generated during CO<sub>2</sub> reduction with **14** and **15** in the presence of Mg<sup>2+</sup> cations that act as a Lewis acid, which promotes catalysis at much lower overpotential and a change in mechanism to that of reductive disproportionation of CO<sub>2</sub> (eq. 20) [92]. In this case, spectral activity in the 1600 – 1700 cm<sup>-1</sup> region was assigned to the formation of CO<sub>3</sub><sup>2-</sup> and HCO<sub>3</sub><sup>-</sup> species, in addition to a [Mn(mes<sub>2</sub>bpy)(CO)<sub>3</sub>(CO<sub>2</sub>Mg)]<sup>+</sup> intermediate.

$$2 \text{ CO}_2 + 2e^- \rightarrow \text{CO} + \text{CO}_3^{2-}$$
 (20)

In other work, Kubiak appended methyl acetamidomethyl groups at the 4,4'-positions of the bpy ligand in the dacbpy ligand (dacbpy = 4,4'-bis(methyl acetamidomethyl)-2,2'-bipyridine) for both Mn- (16) and Re-based (17) CO<sub>2</sub> reduction catalysts (Fig. 14) [93]. Catalysis with mixtures of the Mn and Re catalysts resulted in slightly better catalytic performance than with the individual catalysts alone. This was interpreted as being due to the formation of non-covalent hydrogen bonding interactions between the amide groups leading to the assembly of supramolecular catalytically active species (Fig. 14, 18). IR-SEC was used to characterize the usual one- and two-electron reduced species, and also indicated that the Re and Mn centers interact during the reduction mechanism, potentially even forming heterobimetallic bonds in the absence of CO<sub>2</sub>.

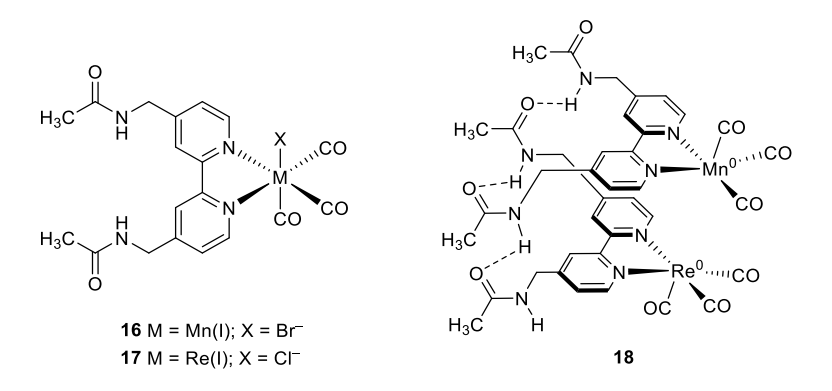


**Figure 14.** Molecular structure of the [Mn(X)(dacbpy)(CO)<sub>3</sub>] monomeric pre-catalysts **16** and **17** reported by Machan et al. alongside the H-bonded active dimer catalyst **18** [93].

Gobetto, Nervi and co-workers also used IR-SEC to characterize the intermediates generated upon the reduction of MnBr(bpy')(CO)<sub>3</sub> catalysts **20** and **21** in which the bpy' ligand was substituted at the 6-position with a phenyl ring containing either two (pdbpy = 4-phenyl-6-(phenyl-3,4,5-triol)-2,2'-bipyridine) or three (ptbpy = 4-phenyl-6-(phenyl-3,4,5-triol)-2,2'-bipyridine) hydroxyl groups, respectively, which can act as a local proton source during CO<sub>2</sub> reduction catalysis (Fig. 15) [94]. The behavior was understandably more complex than that observed with catalysts that lack local OH groups. For the catalyst containing OH groups in the *ortho* positions of the phenyl ring, Mn–Mn dimerization is suppressed by reductive deprotonation of one of the OH groups and coordination of the resulting phenolate to the Mn center. In addition, a Mn-hydride species was also observed as a minor intermediate. At more negative potentials, further reduced species were observed, up to the two-electron reduced, doubly deprotonated active catalyst. Reductive deprotonation has also been observed by IR-SEC in CH<sub>3</sub>CN for the Mn-based catalyst containing the 4,4'-dihydroxy-2,2'-bipyridyl (dhbpy) ligand in MnBr(dhbpy)(CO)<sub>3</sub> (22) [95].

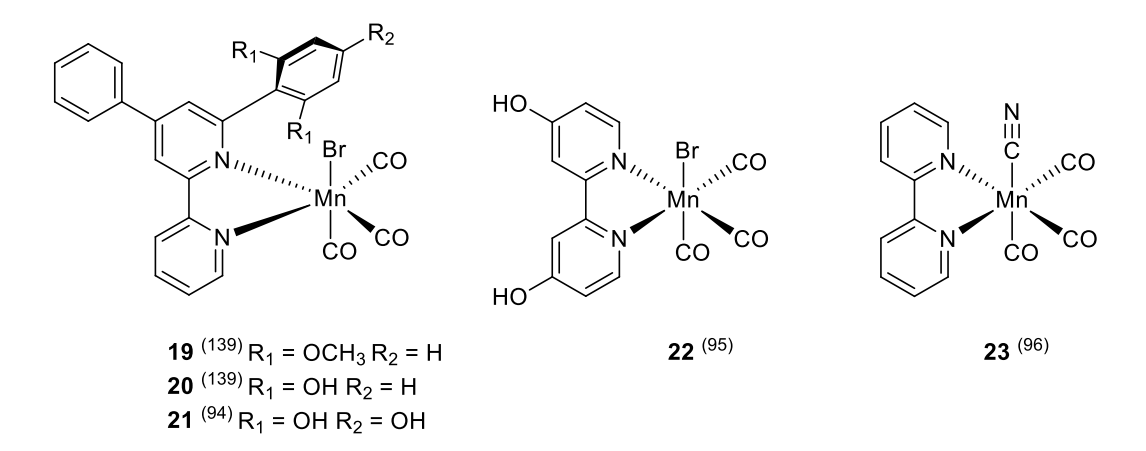


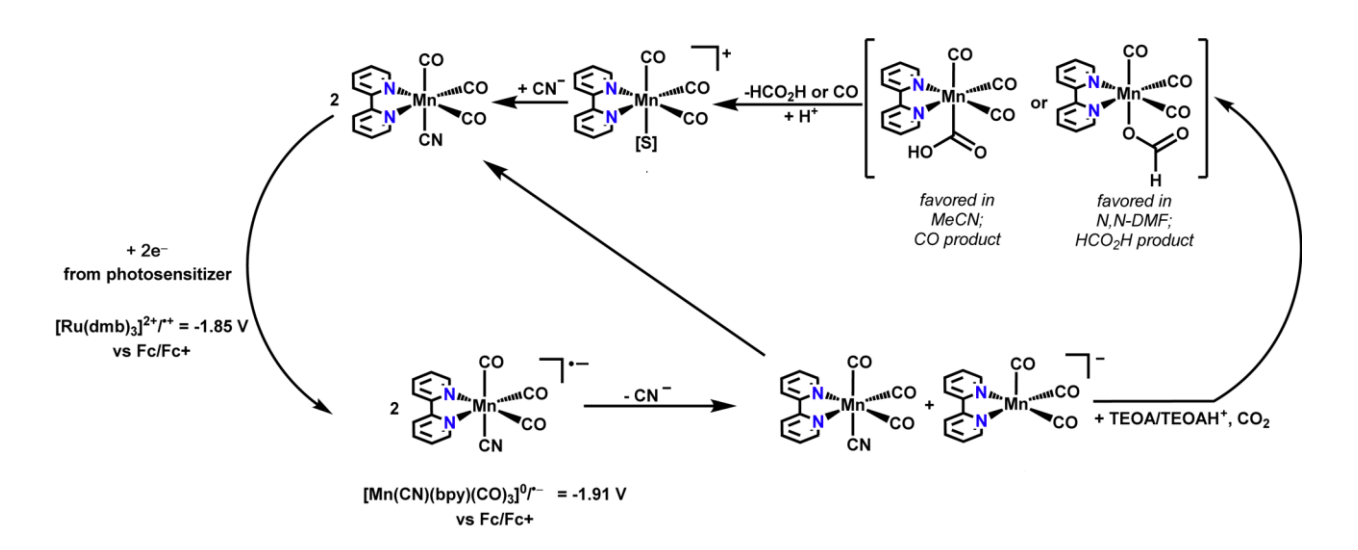
**Figure 15.** Molecular structures of the dimethoxy (19), dihydroxy (20) and trihydroxy (21) substituted complexes reported by Gobetto, Nervi and co-workers alongside complexes 22 and 23 reported independently by Cowan and Kubiak, respectively. Citations are provided in parentheses.

An interesting study that involved the replacement of the bromide ligand in 2 by cyanide, i.e., Mn(CN)(bpy)(CO)<sub>3</sub> (Fig. 15, 23), made use of IR-SEC as supporting evidence for an additional mechanistic pathway that takes place at the potential of the first reduction of the catalyst, involving disproportionation of the one-electron reduced [Mn(CN)(bpy)(CO)<sub>3</sub>]<sup>--</sup> species to generate the two-electron reduced active catalyst, [Mn(bpy)(CO)<sub>3</sub>]<sup>-</sup> [96]. This behavior is attributed to the strong-field nature of the CN<sup>-</sup> ligand that prevents its rapid dissociation upon one-electron reduction, and thus suppresses Mn–Mn dimer formation. Spectral observations in the 1600 cm<sup>-1</sup> region in the presence of CO<sub>2</sub> and 0.5 M phenol as a Brønsted acid resulted in the assignment of a new band at 1587 cm<sup>-1</sup> to phenoxide (PhO<sup>-</sup>) and another at 1654 cm<sup>-1</sup> to H<sub>2</sub>O, which would be the by-product of the proton-coupled two-electron reduction of CO<sub>2</sub> to CO (eq.

4). However, clarification of this band assignment may be required since it is known that  $H_2O$  in  $CH_3CN$  exhibits a characteristic  $\delta(H-O-H)$  bending vibration at ~1631 cm<sup>-1</sup> [97], which is >20 cm<sup>-1</sup> away from the 1654 cm<sup>-1</sup> band observed in the IR-SEC experiment.

In follow-up work, Kubiak and co-workers investigated the photocatalytic reduction of CO<sub>2</sub> to CO and HCO<sub>2</sub>H using 23 as the catalyst precursor and [Ru(dmbpy)<sub>3</sub>]<sup>2+</sup> as a visible lightabsorbing photosensitizer that receives an electron from the sacrificial reductant, 1-benzyl-1,4dihydronicotinamide (BNAH), upon irradiation with 470 nm light [98]. This experiment takes advantage of the fact that one-electron reduction of 23 by the reduced photosensitizer ([Ru(dmbpy)<sub>3</sub>]\*+), results in disproportionation of [Mn(CN)(bpy)(CO)<sub>3</sub>]\*- to generate one equivalent of the active catalyst, [Mn(bpy)(CO)<sub>3</sub>]<sup>-</sup>. Two different solvent systems were employed, DMF/TEOA (4:1 v/v) and CH<sub>3</sub>CN/TEOA (4:1 v/v). TEOA was used as a base to deprotonate the oxidized BNAH, i.e., BNAH<sup>++</sup>, thus preventing back-electron transfer. It was found that in CH<sub>3</sub>CN/TEOA, the favored reduction product was CO, whereas in DMF/TEOA it was HCO<sub>2</sub>H (see Section 5.2). IR-SEC experiments in the  $\nu$ (CO) region were performed in the two solvent systems. In both cases, at the first reduction potential of 23, IR bands at 1911 and 1810 cm<sup>-1</sup> corresponding to the two-electron reduced [Mn(bpy)(CO)<sub>3</sub>] disproportionation product were observed to grow in. However, in the case of CH<sub>3</sub>CN/TEOA, the [Mn(CN)(bpy)(CO)<sub>3</sub>] intermediate was not observed, while in DMF/TEOA a significant amount of it could be seen from bands at 2003, 1909, and 1893 cm<sup>-1</sup> that appear and then decay as the two-electron reduced product forms. It was proposed that this difference in the stability of [Mn(CN)(bpy)(CO)<sub>3</sub>] between the two solvent systems might account for the different product selectivities. Thus, in CH<sub>3</sub>CN/TEOA, [Mn(bpy)(CO)<sub>3</sub>] is rapidly generated, resulting in the

formation of a Mn-CO<sub>2</sub>H intermediate and CO production, while in DMF/TEOA there is sufficient time available for a competing reaction involving H-atom abstraction by [Mn(CN)(bpy)(CO)<sub>3</sub>]<sup>\*-</sup> from TEOA or perhaps BNAH<sup>\*+</sup>, to generate a hydride such as Mn(H)(bpy)(CO)<sub>3</sub>, which could then react by insertion of CO<sub>2</sub> into the Mn–H bond to generate a Mn-OC(O)H intermediate, and ultimately HCO<sub>2</sub>H (see Scheme 4).



**Scheme 4:** Proposed mechanism for the formation of HCO<sub>2</sub>H and CO products in the photocatalytic reduction of CO<sub>2</sub> with Mn(CN)(bpy)(CO)<sub>3</sub> (**23**) as the catalyst precursor and [Ru(dmbpy)<sub>3</sub>]<sup>2+</sup> as the photosensitizer. CO is favored in CH<sub>3</sub>CN/TEOA while HCO<sub>2</sub>H is favored in DMF/TEOA. Reproduced with permission from ref. [98]. Copyright 2016 American Chemical Society.

IR-SEC mechanistic investigations of Mn-based CO<sub>2</sub> reduction catalyst precursors have not been restricted to bpy-based systems. For example, Hartl and co-workers have studied MnBr(<sup>i</sup>Pr-DAB)(CO)<sub>3</sub> **24**, which contains the non-aromatic 1,4-diazabuta-1,3-diene (DAB) ligand substituted with <sup>i</sup>Pr groups (Fig. 16) [99]. Similar to Kubiak's mes<sub>2</sub>bpy system, the two-electron

five-coordinate reduced anion, [Mn(iPr-DAB)(CO)<sub>3</sub>] is generated at the two-electron reduction potential of the parent complex. However, in the presence of H<sub>2</sub>O, this anion converts into a stable bicarbonate complex, [Mn( $^{i}$ Pr-DAB)(CO)<sub>3</sub> ( $\eta^{1}$ -OCO<sub>2</sub>H] which must be further reduced to produce another intermediate that is then reduced to initiate catalysis at ~650 mV more negative potential than the initial reduction potential of the parent complex. The IR-SEC data also revealed that the high concentration of the CO reduction product produced in the thin-solution layer of the IR-SEC cell resulted in the production of [Mn(CO)<sub>5</sub>] by displacement of the DAB ligand by CO. Replacement of the Pr substituents by p-tolyl groups in the DAB ligand resulted in a shutdown of the catalytic activity, highlighting the fact that subtle electronic changes can be used to tune catalytic performance for this series of catalysts. Related Mn-DAB complexes bearing bulky groups such as mesityl as N-substituents in the DAB ligand were also studied by IR-SEC for  $CO_2$  reduction (Fig. 16, 26 - 29) [100]. In this case, the intact one-electron reduced complex (prior to Br<sup>-</sup> loss) was observable by IR, which contrasts with the very rapid ejection of Br<sup>-</sup> from the one-electron reduced form of the Mn-bpy complexes. Furthermore, no Mn–Mn dimer was produced, with only the five-coordinate anion active catalyst being observed. It should be noted that this series of complexes promoted the reductive disproportionation of CO<sub>2</sub> to CO and CO<sub>3</sub><sup>2-</sup> (Eq. 20), as a consequence of the Mn center being less nucleophilic than in the Mn-bpy complexes. Thus, a band at 1650 cm<sup>-1</sup> due to CO<sub>3</sub><sup>2-</sup> was observed in these IR-SEC experiments.

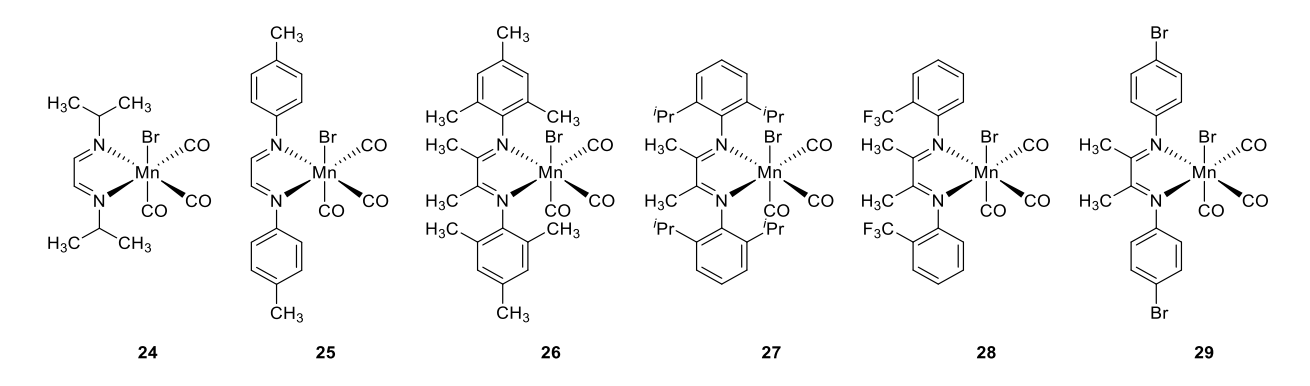


**Figure 16.** Molecular structures of the MnBr(DAB)(CO)<sub>3</sub> complexes reported by Hartl (24, 25) [99] and Kubiak (26 – 29) [100] where DAB is a N,N'-disubstituted 1,4-diazabutadiene ligand.

Other notable examples of the use of IR-SEC to probe catalytic mechanisms of CO<sub>2</sub> reduction by Mn-based catalyst precursors containing non-bpy ligands include complexes containing *m*-terphenyl isocyanide ligands [101], a new class of Mn complexes containing asymmetric 2-iminopyridine ligands that have allowed steric and electronic properties to be decoupled and independently tuned [80], complexes containing terpyridine ligands [102], and complexes containing the phenanthroline-5,6-dione ligand [103].

Finally, we note that all of the investigations highlighted so far in this section have been performed in organic solvent (CH<sub>3</sub>CN) using homogeneous catalyst precursors dissolved in solution. However, there is strong interest in performing this type of CO<sub>2</sub> reduction catalysis in aqueous solution. One promising way to go about this is to immobilize homogeneous catalysts on an electrode surface, thus eliminating water solubility issues, with the added benefit that immobilized catalysts are often more robust and may even exhibit enhanced catalytic activity compared to in homogeneous solution. Spectroscopic studies of immobilized catalysts are

generally more challenging. However, we note one such recent study with a Mn-bpy catalyst precursor that was appended with a pyrene moiety on the bpy ring using the 4-methyl-4'-(5-(pyren-1-yl)pentyl)-2,2'-bipyridine) ligand (bpy<sub>pyr</sub>, Fig. 17), which permitted immobilization of the complex onto a carbon nanotube electrode [104]. In-situ attenuated total reflection (ATR) IR spectroscopy was performed, which helped to understand the change in product selectivity with catalyst loading. Thus, at higher surface loading a Mn–Mn dimer formed, which led to preferential formation of CO as the reduction product, whereas at lower catalyst loading a Mn–H intermediate was observed, resulting in enhanced production of formate as the reduction product by insertion of CO<sub>2</sub> into the Mn–H bond. Such surface-sensitive SEC methods, together with other more advanced surface-sensitive spectroscopic techniques [105] will likely play important roles in future mechanistic investigations of CO<sub>2</sub> reduction by immobilized catalysts, and for the investigation of electrode-catalyst interactions in general.

**Figure 17.** Molecular structure of the MnBr(bpy<sub>pyr</sub>)(CO)<sub>3</sub> pre-catalyst reported by Reisner and co-workers for immobilization on MWCNT electrodes [104].

#### 4.2 Electron paramagnetic resonance (EPR) spectroscopy

We have so far focused mainly on IR-SEC as a mechanistic tool for characterizing CO<sub>2</sub> reduction intermediates. However, other structurally sensitive techniques have also been applied, such as electron paramagnetic resonance (EPR) spectroscopy. For example, Kubiak and

Walensky used EPR to confirm that the unpaired electron in the Re(MesDABMe•-) (CO)<sub>3</sub>(CH<sub>3</sub>CN) intermediate is largely localized on the DAB ligand [100]. A recent notable example of the application of EPR to Mn-based CO<sub>2</sub> reduction catalysts was the use of advanced pulsed-EPR methods for the discovery of an unusual low-spin, paramagnetic [Mn<sup>II</sup>-CO<sub>2</sub>H]<sup>+</sup> metallocarboxylic acid intermediate and thus a possible alternative catalytic pathway for CO<sub>2</sub> reduction [106]. For the catalyst precursor 3 in the presence of CO<sub>2</sub> and H<sub>2</sub>O, it was noted that in addition to the usual catalytic current observed in the CV at the second reduction potential of the complex (where the Mn<sup>0</sup>–Mn<sup>0</sup> dimer is reduced to the two-electron reduced [Mn(dmbpy)(CO)<sub>3</sub>]<sup>-</sup> species), additional current enhancement was also observed at the first reduction potential of the complex [35]. At this more positive potential, the Mn<sup>0</sup>-Mn<sup>0</sup> dimer is generated but cannot be further reduced to [Mn(dmbpy)(CO)<sub>3</sub>], thus implying that an alternative catalytic pathway exists involving the reaction of CO<sub>2</sub> and H<sup>+</sup> with the Mn<sup>0</sup>-Mn<sup>0</sup> dimer. Such a possibility was explored by UV/Vis-SEC and pulsed-EPR methods (2P-ESEEM and HYSCORE), resulting in the characterization of [mer-Mn<sup>II</sup>(dmbpy)(CO)<sub>3</sub>(CO<sub>2</sub>H)]<sup>+</sup> as the product of oxidative addition of CO<sub>2</sub> and H<sup>+</sup> to the Mn<sup>0</sup>-Mn<sup>0</sup> dimer. This is a low-spin, paramagnetic Mn<sup>II</sup> species, hence the utility of EPR for its characterization. Completion of the catalytic cycle was proposed to occur by the oneelectron reduction of the [Mn<sup>II</sup>-CO<sub>2</sub>H]<sup>+</sup> intermediate together with its reaction with H<sup>+</sup> and a solvent molecule, resulting in the elimination of H<sub>2</sub>O and CO products (blue pathway in Scheme 5). However, we believe it is unlikely that one-electron reduction / protonation will result in the spontaneous ejection of both  $H_2O$ and CO. One-electron reduction of [Mn<sup>II</sup>(dmbpy)(CO)<sub>3</sub>(CO<sub>2</sub>H)]<sup>+</sup> would produce Mn<sup>I</sup>(dmbpy)(CO)<sub>3</sub>(CO<sub>2</sub>H), which is the same metallocarboxylic acid intermediate that is in the currently accepted catalytic cycle for CO<sub>2</sub> reduction with this family of catalysts (Scheme 1). Subsequent protonation would generate

[Mn<sup>I</sup>(dmbpy)(CO)<sub>4</sub>]<sup>+</sup> via H<sub>2</sub>O elimination. This type of species is a stable, isolable molecule (vide infra) [107-111] that is unlikely to undergo spontaneous ejection of CO (as implied by the blue pathway in Scheme 5). We therefore suggest that an alternative pathway at this applied potential might involve an additional one-electron reduction of [Mn<sup>I</sup>(dmbpy)(CO)<sub>4</sub>]<sup>+</sup> to [Mn<sup>I</sup>(dmbpy<sup>-</sup>)(CO)<sub>4</sub>]<sup>0</sup>, which should be unstable with respect to CO ejection, producing [Mn(dmbpy)(CO)<sub>3</sub>]<sup>+</sup> radicals that will dimerize to regenerate the Mn<sup>0</sup>–Mn<sup>0</sup> dimer and complete the catalytic cycle without returning to the original Mn<sup>I</sup> catalyst precursor (red pathway in Scheme 5). However, perhaps the fact that the [Mn<sup>II</sup>-CO<sub>2</sub>H]<sup>+</sup> intermediate was predicted [106] to have *mer* isomer structure, geometry might also play a role in the proposed reactivity.

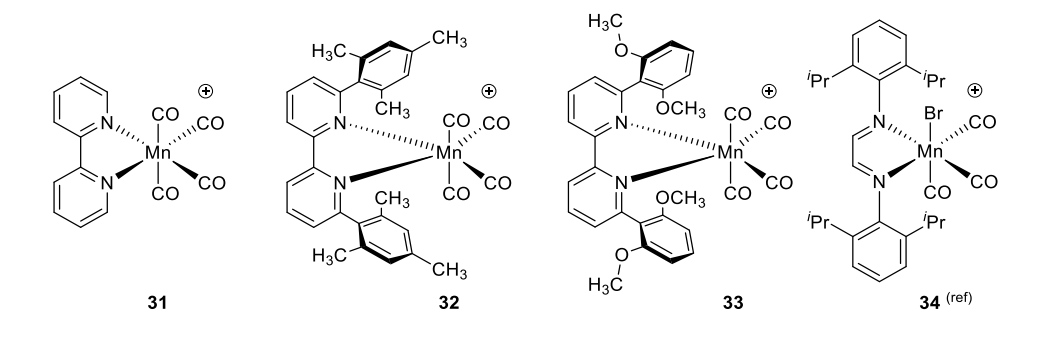
Scheme 5: Starting from the solvento complex, [Mn<sup>I</sup>(dmbpy)(CO)<sub>3</sub>(CH<sub>3</sub>CN)]<sup>+</sup>, the mechanism for the electrocatalytic reduction of CO<sub>2</sub> to CO in CH<sub>3</sub>CN in the presence of 5% H<sub>2</sub>O that occurs at the first reduction potential of the complex, proposed by Orio, Chardon-Noblat, and coworkers [106], is depicted by the black and blue arrows. Note that although their experiments were performed with 3, one-electron reduction of these complexes results in the ejection of either CH<sub>3</sub>CN or Br<sup>-</sup> and the formation of identical products, so which starting complex is used is inconsequential. Shown by the black and red arrows is an alternative mechanism that we suggest might be more viable, not requiring the spontaneous ejection of CO from [Mn<sup>I</sup>(dmbpy)(CO)<sub>4</sub>]<sup>+</sup> (as implied by the blue pathway).

## 4.2.1 Comments on the tetracarbonyl intermediates

In the catalytic cycle of  $CO_2$  reduction to CO by  $[MnL(\alpha-diimine)(CO)_3]^{+/0}$  complexes (Scheme 1), both the *protonation-first* and *reduction-first* pathways converge at a common  $Mn^I(\alpha-diimine^-)(CO)_4$  intermediate following the prior rate determining C–OH bond cleavage and  $H_2O$  elimination steps. There has been little attention paid to these final steps of the catalytic cycle and the properties of this neutral tetracarbonyl intermediate have not yet been studied, thus knowledge of its stability is still up for question. For example, does CO spontaneously dissociate to generate the five coordinate  $Mn^0(\alpha-diimine)(CO)_3$  radical, prone to rapid dimerization, followed by a reduction step to regenerate the active catalyst,  $[Mn^0(\alpha-diimine^-)(CO)_3]^{-?}$  Or, alternatively, is one-electron reduction of  $Mn^I(\alpha-diimine^-)(CO)_4$  kinetically favored over CO loss to enhance the rate of CO evolution and directly regenerate the active catalyst in a typical EC electrochemical mechanism? We speculate that CO dissociation from the neutral  $Mn^I(\alpha-diimine^-)(CO)_4$  intermediate is possible but under the experimental conditions often employed

during electrocatalysis with large overpotentials, initial one-electron reduction to evolve CO and directly regenerate the active catalyst is a more likely pathway. These are questions which are likely best addressed in the future using techniques such as IR-SEC. At least, from the perspective of the *protonation-first* pathway, we can state that the cationic tetracarbonyl species  $[Mn^I(\alpha-diimine)(CO)_4]^+$  is very stable and even isolable [107-111]. Notably, this could allow access to the neutral  $Mn^I(\alpha-diimine^+)(CO)_4$  intermediate via the aforementioned IR-SEC studies. In either case, whether studying the *protonation-first* or *reduction-first* pathway, formation of these manganese tetracarbonyl species is directly related to the prior rate determining steps and therefore their characterization and spectroscopic information carry significant importance in the further understanding and optimization of the catalytic reduction of  $CO_2$  to CO.

Focusing on the protonation-first pathway, we have recently synthesized some cationic manganese tetracarbonyl species, namely [Mn(bpy)(CO)<sub>4</sub>]<sup>+</sup> (31), [Mn(mes<sub>2</sub>bpy)(CO)<sub>4</sub>]<sup>+</sup> (32), and {Mn[(MeO<sub>2</sub>Ph)<sub>2</sub>bpy](CO)<sub>4</sub>}<sup>+</sup> (33), starting from their manganese tricarbonyl bromide forms, MnBr(α-diimine)(CO)<sub>3</sub>, stirring with 1.1 equivalents of AgBF<sub>4</sub> under a bubbling stream of CO gas for 4 hours in dichloromethane (DCM) solvent at room temperature. v(CO) IR data for these complexes, and a related Mn-based tetracarbonyl cation (34), dissolved in DCM, are presented in Table 1, and the IR spectrum of 31 is shown in Fig. 18. These species will be the subject of future IR-SEC investigations, as discussed above.



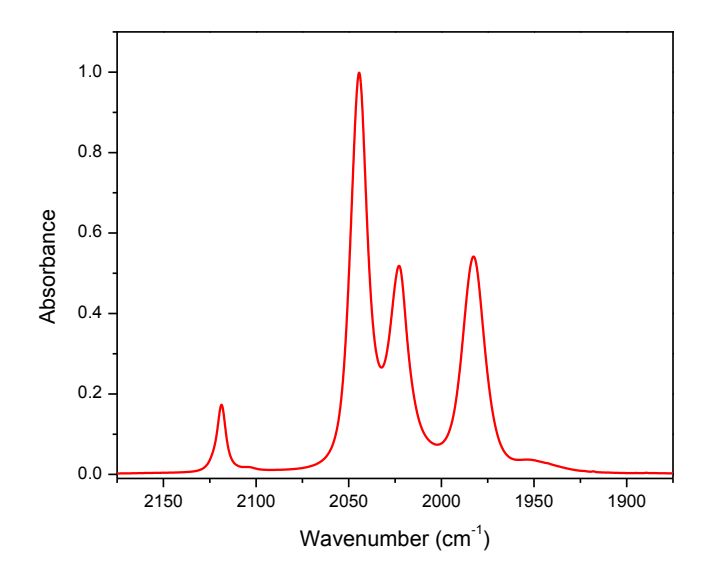


**Figure 18.** (top) Molecular structures of isolated  $[Mn(\alpha\text{-diimine})(CO)_4]^+$  cations. (bottom) FTIR spectrum of the  $[Mn(bpy)(CO)_4](BF_4)$  complex recorded in dichloromethane.

Table 1. IR data for Mn-based tetracarbonyl cations

Compound	ν(CO) (cm <sup>-1</sup> )	Solvent	Ref.
[Mn(CO) <sub>4</sub> (bpy)]BF <sub>4</sub>	2119, 2044, 2023, 1983	DCM	[107] & this review
[Mn(CO) <sub>4</sub> (mes <sub>2</sub> bpy)]BF <sub>4</sub>	2106, 2026, 2018 <sub>sh</sub> , 1982	DCM	This review
$\{Mn(CO)_4[(MeO_2Ph)_2bpy\}BF_4$	2110, 2036, 2009, 1968	DCM	This review
$[Mn(CO)_4(^iPr_2Ph-DAB)]PF_6$	2109, 2042, 2027, 2006	DCM	[111]

 $<sup>^{1}</sup>$ Pr<sub>2</sub>Ph-DAB = (N,N'-bis(2,6-diisopropylphenyl)-1,4-diaza-1,3-butadiene)

## 4.3 Stopped-flow techniques

When catalytic intermediates are too short-lived to be monitored by steady-state spectroscopic methods, faster time-resolved techniques are required. One such technique that can be used to study the kinetics of reactions on the milli- to sub-millisecond timescale is stoppedflow mixing [112]. Typically, two solutions held in syringes are rapidly mixed in a mixing chamber, initiating a chemical reaction and then the mixed solution flows into a spectroscopic cell where it is suddenly stopped and monitored by a fast spectroscopic technique. Although to the best of our knowledge, stopped-flow has not been used to investigate CO<sub>2</sub> reduction processes with Mn-based catalysts, Kubiak and co-workers have used stopped-flow with UV/Vis detection to monitor the kinetics of the reaction of the two-electron reduced form of a Re-based CO<sub>2</sub> reduction catalyst, [Re(dtbpy)(CO)<sub>3</sub>] with CO<sub>2</sub>, H<sub>2</sub>O, CH<sub>3</sub>OH, and TFE in THF, monitoring the decay of the characteristic 570 nm absorption band of [Re(dtbpy)(CO)<sub>3</sub>]<sup>-</sup> [113]. This revealed that the Re-based anion reacts with CO<sub>2</sub> about 25 times faster than with H<sub>2</sub>O, and 50 times faster than with CH<sub>3</sub>OH. No reaction with TFE was observed. These results are consistent with the high selectivity of [Re(dtbpy)(CO)<sub>3</sub>]<sup>-</sup> for CO<sub>2</sub> reduction over H<sup>+</sup> reduction. In later work, Kubiak and co-workers made use of stopped-flow with rapid-scan FTIR detection to directly characterize and monitor the kinetics of formation of the metallocarboxylic acid intermediate,  $Re(bpy')(CO)_3(CO_2H)$  (bpy' = bpy or dtbpy) [114]. Similar to before, [Re(bpy')(CO)<sub>3</sub>] was chemically synthesized and a THF solution of it was mixed with CO<sub>2</sub>saturated THF in the presence or absence of either CH<sub>3</sub>OH or H<sub>2</sub>O as Brønsted acid. The Re- $CO_2H$  intermediate was not only characterized by its strong  $\nu(CO)$  vibrations, but also by a pair of v(OCO) bands at 1662 and 1616 cm<sup>-1</sup> due to the bound CO<sub>2</sub>H moiety.

### 4.4 Time-resolved infrared (TRIR) spectroscopy

Laser flash photolysis with UV/vis laser pulses is a well-established technique for rapidly generating the excited state of a chromophore [115]. When coupled with transient absorption spectroscopy in the UV, visible, or near-IR regions, it provides excellent information on the dynamics of various photoinduced processes such as excited state formation, intra- and intermolecular electron or energy transfer, and bond formation / cleavage reactions. Depending on the pulse width of the excitation laser and the transient absorption spectroscopy method used, processes on time scales ranging from femtoseconds to milliseconds or longer can be interrogated. This technique is thus ideally suited to the investigation of fast events involved in photocatalytic CO<sub>2</sub> reduction, such as the quenching of electronic excited states by sacrificial electron donors, intramolecular electron transfer in supramolecular systems, and the generation of catalytic intermediates. However, spectral bands in the UV/vis regions are often broad, which can sometimes make it difficult to assign bands to specific species. The structural characterization of these short-lived species becomes much easier when time-resolved vibrational spectroscopy, such as time-resolved resonance Raman (TR<sup>3</sup>) or time-resolved infrared (TRIR), is employed.

TRIR spectroscopy has a long history, dating back as far as 1958 [116], and it has become a definitive method for the identification of short-lived intermediates, particularly in systems that contain good IR reporter groups (e.g., CO or CN). In terms of its application to CO<sub>2</sub> reduction catalysis, TRIR has been heavily applied to the  $[Re(\alpha\text{-diimine})(CO)_3(L)]^{0/+}$  family of catalysts (as well as others), having been used to identify the nature of photoinduced excited states (through characteristic shifts of the intense v(CO) IR bands) and to probe subsequent inter- and intramolecular electron transfer processes (including interfacial electron transfer), and the

formation of catalytic intermediates. There have been many examples of such studies, and rather than attempt a comprehensive review here, the reader is referred to several excellent review articles that have been published over the years [117-122].

Although a number of Mn-based transition metal complexes have been investigated for a variety of reasons by TRIR spectroscopy e.g., [123, 124], to the best of our knowledge, no Mn-based CO<sub>2</sub> reduction catalysts have been studied by TRIR following laser flash photolysis. Reasons for this include the fact that first-row transition metal complexes generally have extremely short-lived excited states that cannot easily be coupled into electron transfer processes, and also the fact that they are quite photosensitive with photolabile ligands. Of course, a separate photosensitizer molecule can be used, the excited state of which is reductively quenched by a sacrificial electron donor (see Section 5.2.1), resulting in electron transfer to the Mn catalyst that could be probed by TRIR. Given the continued interest in and development of new Mn-based CO<sub>2</sub> reduction catalysts, such experiments are likely to be reported in the future.

#### 4.5 Pulse radiolysis coupled with time-resolved infrared spectroscopy (PR-TRIR)

Pulse radiolysis (PR) is a well-established time-resolved technique that strongly complements laser flash photolysis [125]. In PR, a high-energy electron pulse from an accelerator is used to excite a sample, rapidly generating either the one-electron reduced or oxidized form of a dissolved solute, or in some cases its excited state. PR differs fundamentally from laser flash photolysis in that the energy of the electron pulse is deposited in the medium (i.e., the solvent) as opposed to being absorbed directly by solute molecules, as is the case with pulsed laser excitation. Generally, the incident electron pulse passes through the sample, ionizing solvent molecules along the way, producing energetic electrons and holes (radical cations of

solvent molecules). Many of these electron-hole pairs geminately recombine, but a certain proportion of the electrons escape the so-called Onsager radius, causing further ionizations in a cascade process. Secondary reactions then occur between the electrons, holes, and solvent molecules, producing a homogeneous mixture of solvated electrons ( $e_s^-$ ), cations (generally solvated protons), and various solvent-derived radicals on a timescale of <100 ns. For example, in water the final mixture is shown in Eq. (21) [126], where the numbers in parentheses are the radiation chemical yields (G values) in units of molecules/100 eV of absorbed energy, and  $e_{aq}^-$  represents the solvated electron in water.

$$H_2O \longrightarrow e_{aq}^-(2.7), H^{\bullet}(0.55), {^{\bullet}OH}(2.8), H_2(0.45), H_2O_2(0.7), H_3O^{+}(2.7)$$
 (21)

The utility of PR lies in the fact that the overall redox conditions of the solution can be controlled to be either oxidizing or reducing through the judicious addition of additives that scavenge particular radicals, while leaving others, including new secondary radicals, to react with dissolved solutes. There are many such "tricks of the trade" that have been well documented, particularly for aqueous solutions [126]. For example, oxidizing radicals can be eliminated by the addition of *tert*-butanol, leaving  $e_{aq}^-$  to reduce solutes, while 'OH radicals can be left to oxidize solutes after the scavenging of  $e_{aq}^-$  by N<sub>2</sub>O. Another example is the strongly reducing carbon dioxide radical anion (CO<sub>2</sub><sup>-</sup>) that can be produced by H-atom transfer from added formate (HCO<sub>2</sub><sup>-</sup>) to 'H and 'OH radicals.

When combined with time-resolved spectroscopy, PR becomes a powerful mechanistic tool for investigating redox catalysis, and it has been widely applied to both homogeneous and heterogeneous catalytic systems that are used in artificial photosynthesis processes [127]. Since PR does not involve the direct excitation of a solute, it is particularly suited to the study of

catalysts that have short excited state lifetimes, or which are too photosensitive for direct study by laser flash photolysis. It is also invaluable for mechanistic studies of electrocatalysts since specific redox intermediates can be rapidly prepared and their reactivity can be monitored. Indeed, it has the time resolution to allow the detection of short-lived intermediates that cannot be observed by spectroelectrochemistry (SEC). As in laser flash photolysis, improved characterization of intermediates generated by PR can be obtained through the use of TRIR detection, in a so-called PR-TRIR experiment. Until recently, PR-TRIR had only ever been applied to gas-phase samples [128, 129]. However, taking advantage of developments in tunable, high power quantum-cascade IR laser technology, Grills and co-workers successfully coupled, for the first time, nanosecond TRIR detection with the PR of condensed-phase samples [130, 131]. More recently, they coupled the complementary TRIR method of time-resolved step-scan FTIR spectroscopy with PR, for the rapid acquisition of broadband TRIR spectra following PR [47]. Most PR-TRIR work so far has been performed in organic solvents such as CH<sub>3</sub>CN, THF, and DMF [130, 132]. However, the detection of transient metal-hydride species was demonstrated in aqueous solution [127].

An example of the application of PR-TRIR to understand the mechanism of reactivity of a Mn-based CO<sub>2</sub> reduction electrocatalyst comes from the study of the mononuclear catalyst precursor, Mn(dtbpy)(CO)<sub>3</sub>(OC(O)H) in CH<sub>3</sub>CN (OC(O)H<sup>-</sup> = formate, added to the solution as a radiolytic solvent radical scavenger and which displaced the original Br<sup>-</sup> ligand upon dissolution) [55]. As discussed above, one-electron reduction of the MnL(bpy')(CO)<sub>3</sub> (L = Br<sup>-</sup>, OTf<sup>-</sup>) family of catalyst precursors results in the formation of a Mn–Mn bonded dimer intermediate. However, very few mechanistic details were available from IR-SEC experiments due to the short lifetimes

of the intermediates. One-electron reduction by  $e_s^-$  in CH<sub>3</sub>CN permitted the initial observation of the fully intact radical anion, [Mn(dtbpy\*-)(CO)<sub>3</sub>(OC(O)H)]<sup>-</sup> (black TRIR spectrum in Fig. 19), followed by formate dissociation ( $\tau = 77$  ns) and the production of the neutral Mn-based radical, Mn<sup>0</sup>(dtbpy)(CO)<sub>3</sub> (red TRIR spectrum in Fig. 19). Finally, dimerization of this radical to form the Mn–Mn dimer **8** (blue spectrum in Fig. 19) was monitored, and a second-order kinetic analysis revealed a dimerization rate constant of  $2k_{\text{dim}} = (1.3 \pm 0.1) \times 10^9 \text{ M}^{-1} \text{ s}^{-1}$ . The almost diffusion-controlled rate constant indicated that the neutral radical remains as a five-coordinate species before dimerization, with no solvent binding to the metal center at the vacant coordination site, which correlates with computational results on similar systems (see Section 2.1).

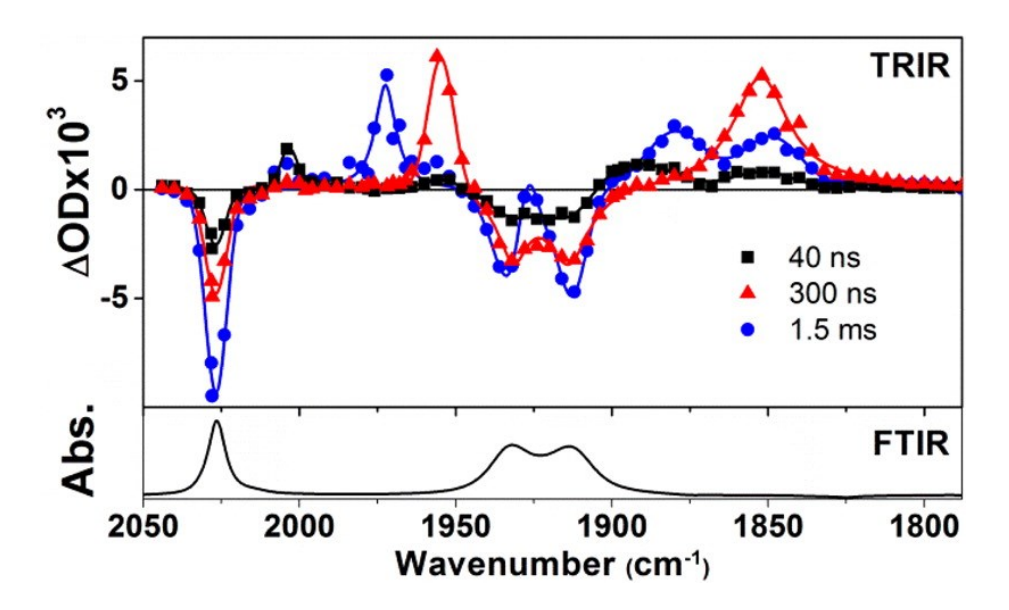


**Figure 19:** IR spectrum of a 1.5 mM solution of Mn(dtbpy)(CO)<sub>3</sub>(OC(O)H) in CH<sub>3</sub>CN containing 50 mM [<sup>n</sup>Bu<sub>4</sub>N][HCO<sub>2</sub>] (bottom) and TRIR spectra recorded 40 ns, 300 ns, and 1.5 ms after pulse radiolysis of this argon-purged solution (top). Reproduced with permission from ref. [55]. Copyright 2014 American Chemical Society.

In more recent work, PR-TRIR was applied to the one-electron reduction of Mn-based CO<sub>2</sub> reduction catalyst precursors containing extremely sterically bulky bpy ligands that prevent dimerization from occurring, e.g., 14 [47]. In those cases, the Mn-based five-coordinate radical, e.g., Mn<sup>0</sup>(mes<sub>2</sub>bpy)(CO)<sub>3</sub> was observed, and confirmed by PR-TRIR not to dimerize. However, more recently, we repeated the PR-TRIR experiment with a higher radiation dose, i.e., under conditions where a higher concentration of the Mn-radical is produced, and the two v(CO) IR bands of the two-electron reduced, [Mn(mes<sub>2</sub>bpy)(CO)<sub>3</sub>] species were observed to grow in on the microsecond timescale at 1806 and ~1905 cm<sup>-1</sup> (see Fig. 20). The observation of a single two-electron reduction wave in the CV of 14, together with the results of previous IR-SEC experiments [64, 92], implied that a disproportionation process takes place upon one-electron reduction of this catalyst precursor, generating the two-electron reduced active catalyst, [Mn(mes<sub>2</sub>-bpy)(CO)<sub>3</sub>]. These PR-TRIR data have confirmed the disproportionation process and have allowed it to be monitored in real time. Additional peaks in Fig. 20 observed at 1854 and ~1945 cm<sup>-1</sup> are assigned to the, as yet unidentified, other product of disproportionation, or a derivative of it.

PR-TRIR is clearly a powerful new way to unravel mechanistic details of catalytic processes, including CO<sub>2</sub> reduction catalysis, which complements the well-established method of laser flash photolysis with UV/vis transient absorption or TRIR detection. It is particularly suited to the study of photosensitive electrocatalysts, and we therefore expect an increasing use of this technique in the coming years with Mn-based and other first-row transition metal complex-based catalysts. In particular, it is anticipated that CO<sub>2</sub>-bound intermediates deeper in the catalytic cycle will be able to be probed by PR-TRIR.

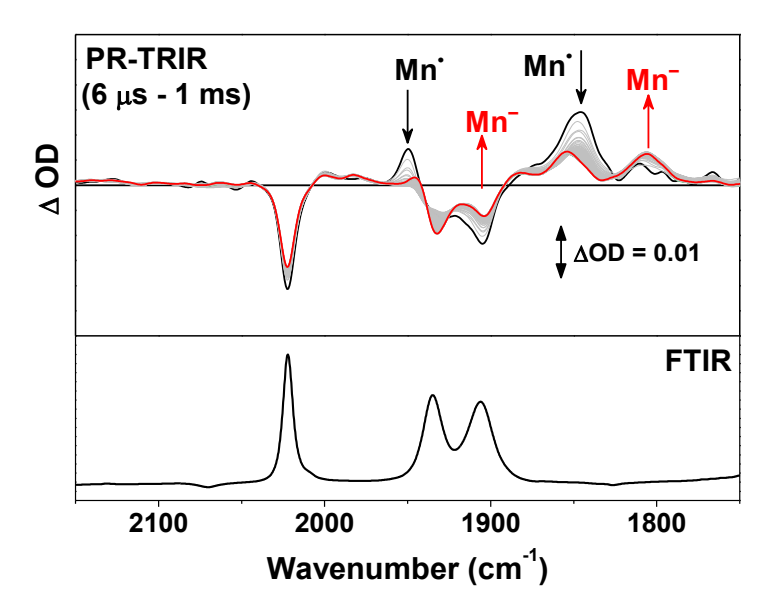


**Figure 20:** Lower panel: FTIR spectrum of Mn(mes<sub>2</sub>bpy)(CO)<sub>3</sub>(OC(O)H) in argon-saturated CH<sub>3</sub>CN in the presence of 50 mM [Bu<sub>4</sub>N][HCO<sub>2</sub>]. Top panel: Step-scan FTIR spectra recorded between 6 μs and 1 ms after PR of this solution with 4 μs pulsewidth electron pulses at the BNL 2MeV Van de Graaff accelerator. **Mn**• = Mn(mes<sub>2</sub>bpy)(CO)<sub>3</sub>, **Mn**- = [Mn(mes<sub>2</sub>bpy)(CO)<sub>3</sub>]<sup>-</sup>. Note that the band of [Mn(mes<sub>2</sub>bpy)(CO)<sub>3</sub>]<sup>-</sup> around 1905 cm<sup>-1</sup> is obscured by a negative bleach band of the starting complex. However, it is clearly evident by the change in intensity ratio of the two lower frequency bleach bands with increasing time delay.

Finally, in light of the important role infrared detection has played, and is likely to play, in the investigation of  $MnX(\alpha\text{-diimine})(CO)_3$   $CO_2$  reduction catalysts, a reference database of  $\nu(CO)$  IR stretches for reported precatalysts, as well as (where available) their one-electron reduced, dimeric, and two-electron reduced derivatives has been provided in Table 2.

**Table 2.**  $\nu(CO)$  infrared stretches for reported MnX( $\alpha$ -diimine)(CO)<sub>3</sub> precatalysts, and their one-electron reduced, dimeric and two-electron reduced derivatives, obtained by a variety of methods including IR-SEC and TRIR spectroscopy.

				v (CO) unless noted otherwise, cm <sup>-1</sup>				
Catalyst Number	$L_2$	X	Medium	MnX(L <sub>2</sub> )(CO) <sub>3</sub>	One-electron reduced	[Mn(L <sub>2</sub> )(CO) <sub>3</sub> ] <sub>2</sub> <sup>a</sup>	$[\mathbf{Mn}(\mathbf{L}_2)(\mathbf{CO})_3]^{-a}$	Reference
2	bpy	Br-	CsI pellet	2024(m), 1932(br)				[35]
			KBr pellet	2019, 1941, 1917				[103]
			CH <sub>3</sub> CN	2027, 1933, 1924			1911, 1811	[94] [95]
		H-	CH <sub>3</sub> CN	1991, 1817, 1804(sh)				[94]
6	bpy	CH <sub>3</sub> CN <sup>b</sup>	CsI pellet	2021(w), 1953(br), 1942(w), \(\nu(CN)\) 2055(m)				[35]
23	bpy	(CN) <sup>-</sup>	0.1 M Bu <sub>4</sub> PF <sub>6</sub> CH <sub>3</sub> CN	ν(CN) 2115, 2029, 1942, 1928			1911, 1837, 1811	[96]
3	dmbpy	Br-	CsI pellet	2021(s), 1951(m), 1927(w), 1995(s)				[35]
	dmbpy	CH <sub>3</sub> CN $^b$	CsI pellet	2020(w), 1952(m), 1943(s), v(CN) 2048(s)				[35]
7	dtbpy	$\mathrm{Br}^-$	0.1 M Bu <sub>4</sub> PF <sub>6</sub> CH <sub>3</sub> CN	2028, 1933, 1923		1973, 1928, 1878, 1850	1907, 1807	[57]
			CH₃CN	2025, 1930, 1921				[95]
			CH₃CN	2026, 1932, 1920				[55]
	dtbpy	OC(O)H <sup>-</sup>	CH <sub>3</sub> CN + 50 mM ["Bu <sub>4</sub> N][HCO <sub>2</sub> ]	2026, 1932, 1914	2004, 1892 <sup>1</sup> 1955, 1853 <sup>m</sup>	1973, 1927, 1880, 1849		[55]
	dtbpy	CH <sub>3</sub> CN <sup>b</sup>	CH <sub>3</sub> CN	2047, 1955				[57]
22	dhbpy	Br-	CH <sub>3</sub> CN	2024, 1930, 1915				[95]
	dhbpy	CH <sub>3</sub> CN <sup>b</sup>	0.1 M Bu <sub>4</sub> PF <sub>6</sub> CH <sub>3</sub> CN	2044, 1955, 1944	2039, 1944, 1932 <sup>c</sup>		2024, 1927, 1903 <sup>d</sup>	[95]
35	dcbpy	Br-	CH <sub>3</sub> CN (5% H <sub>2</sub> O v/v)	2030, 1940, 1931				[95]
55	bpabpy	Br-	ATR	2031, 1918(br), ν(P=O) 1156				[133]
			EtOH	2030, 1946, 1930				[133]
30	$bpy_{pyr}$	Br-	ATR	2016, 1900(br)				[104]
			e	2022, 1930, 1912		1968, 1921, 1870, 1844		[104]
	$bpy_{pyr}$	$H_2O^b$	e	2025, 1938 <sup>f</sup> , 1903 <sup>f</sup>				[104]
	$bpy_{pyr}$	H-	e	1991, 1880				[104]
64	apbpy	Br <sup>-</sup>	ATR	2016(s), 1914(s), 1895(s)				[134]
	$N_2^+$ -pbpy $g$	Br <sup>-</sup>	ATR	ν(N <sub>2</sub> <sup>+</sup> ) 2264(m), 2024(s), 1907(s),				[134]

16	dacbpy	$\mathrm{Br}^-$	CH₃CN	2027, 1933, 1924		1970, 1926, 1898, 1871, 1846	1911, 1811	[93]
49	κ³-tpy <sup>h</sup>	$\mathrm{Br}^-$	CH₃CN	1925, 1853				[102]
	κ³-tpy <sup>h</sup>	CH <sub>3</sub> CN $^b$	0.1 M Bu <sub>4</sub> PF <sub>6</sub> CH <sub>3</sub> CN	1949, 1878		1911, 1882, 1860, 1836, 1798	1830, 174	[102]
50	κ²-tpy	$\mathrm{Br}^-$	CH₃CN	2025, 1935, 1919				[102]
	κ²-tpy	CH <sub>3</sub> CN <sup>b</sup>	0.1 M Bu <sub>4</sub> PF <sub>6</sub> CH <sub>3</sub> CN	2025, 1935, 1919		1921, 1883, 1860, 1798	1830, 1765 <sup>i</sup>	[102]
38	phen	$\mathrm{Br}^-$	KBr pellet	2019, 1946, 1920				[103]
36	phen-dione	$\mathrm{Br}^-$	KBr pellet	2040, 1942, 1925, ν(C=O) 1697				[103]
			0.1 M Bu <sub>4</sub> PF <sub>6</sub> CH <sub>3</sub> CN	2032, 1941, 1931, ν(C=O) 1708	2025, 1929, 1919			[103]
37	phen-dione	CH <sub>3</sub> CN <sup>b</sup>	KBr pellet	2051, 1967, 1950, 1702				[103]
14	mes2bpy	$\mathrm{Br}^-$	THF	2021, 1940, 1906				[64]
			0.1 M Bu <sub>4</sub> PF <sub>6</sub> CH <sub>3</sub> CN	2023, 1936, 1913	1973, 1883, 1866		1909, 1808	[64]
15	mes2bpy	CH <sub>3</sub> CN <sup>b</sup>	THF	2038, 1956, 1926				[64]
			0.1 M Bu <sub>4</sub> PF <sub>6</sub> CH <sub>3</sub> CN + 0.1 M Mg(OTf) <sub>2</sub>	2039, 1949	1984, 1883		1907, 1805	[92]
			CH₃CN	2039, 1948(br)	1950, 1848 <sup>k</sup>		1907, 1806	[47]
	mes2bpy	OC(O)H-	CH <sub>3</sub> CN + 50 mM ["Bu <sub>4</sub> N][HCO <sub>2</sub> ]	2022, 1935, 1906	1950, 1848 <sup>k</sup>		1905, 1806 <sup>k</sup>	This work
9	HOPhbpy	$\mathrm{Br}^-$	ATR	2019(s), 1920(br)				[42]
10	MeOPhbpy	$\mathrm{Br}^-$	ATR	2021(s), 1934(s), 1882(s)				[42]
13	6,6'-bis(2,6- (MeO) <sub>2</sub> Ph)bp y	CH <sub>3</sub> CN <sup>b</sup>	CH <sub>3</sub> CN	2038, 1954, 1941	1947, 1846 <sup>k</sup>		1904, 1805	[47]
20	pdbpy	Br-	0.1 M Bu <sub>4</sub> PF <sub>6</sub> CH <sub>3</sub> CN	2026, 1935, 1925(sh)				[94]
	pdbpy	CH <sub>3</sub> CN <sup>b</sup>	0.1 M Bu <sub>4</sub> PF <sub>6</sub> CH <sub>3</sub> CN	2044, 1961				[94]
21	ptbpy	Br-	0.1 M Bu <sub>4</sub> PF <sub>6</sub> CH <sub>3</sub> CN	2023, 1936, 1914				[94]
	ptbpy	CH <sub>3</sub> CN <sup>b</sup>	0.1 M Bu <sub>4</sub> PF <sub>6</sub> CH <sub>3</sub> CN	2044, 1958		1932, 1880, 1868, 1847	1912, 1817, 1804 <sup>n</sup>	[94]
24	<sup>i</sup> Pr-DAB	Br-	0.1 M Bu <sub>4</sub> PF <sub>6</sub> CH <sub>3</sub> CN	2026, 1930(br)		1975, 1945, 1886(br)	1921, 1811(br)	[99]
	<sup>i</sup> Pr-DAB	$\mathrm{H}_2\mathrm{O}^{\ b}$	0.1 M Bu <sub>4</sub> PF <sub>6</sub> CH <sub>3</sub> CN	2048(s), 1963(m), 1951(sh)				[99]
25	<i>p</i> Tol-DAB	Br-	0.1 M Bu <sub>4</sub> PF <sub>6</sub> THF	2028, 1951, 1925			1946, 1842	[99]
26	MesDAB <sup>Me</sup>	$\mathrm{Br}^-$	KBr pellet	2022, 1949, 1910, ν(C=N) 1383				[100]
26	Mes DAB <sup>Me</sup>	$\mathrm{Br}^-$	0.1 M Bu <sub>4</sub> PF <sub>6</sub> CH <sub>3</sub> CN	2027, 1951, 1913	2011,1923, 1905 °		1924, 1815	[100]
27	<sup>2,6-iPr2</sup> DAB <sup>Me</sup>	$\mathrm{Br}^-$	KBr pellet	2024, 1947, 1922, ν(C=N) 1384				[100]
28	<sup>2-CF3</sup> DAB <sup>Me</sup>	Br-	KBr pellet	2032, 1964, 1937, ν(C=N) 1384				[100]
	•		•					

29	$^{\mathrm{Br}}\mathrm{DAB^{Me}}$	Br <sup>-</sup>	KBr pellet	2027, 1944, 1930, ν(C=N) 1383			[100]
39	N-methyl- N'-2- pyridylimida zol-2-ylidine	Br <sup>-</sup>	ATR	2012(s), 1906(br)			[78]
40	N-methyl- N'-2- pyridylbenzi midazol-2- ylidine	Br <sup>-</sup>	ATR	2015(s), 1927(m,sh), 1897(s)			[78]
42	N-ethyl-N'-2- pyrimidylben zimidazol- 2-ylidene	Br <sup>-</sup>	ATR	2017, 1930, 1889			[79]
43	IMP	$\mathrm{Br}^-$	CH <sub>3</sub> CN	2029, 1941, 1926	1994, 1949, 1902, 1875	1930, 1826	[80]
	IMP	$H_2O^b$	CH <sub>3</sub> CN	2051, 1964, 1958 <sup>f</sup>			[80]
44	IPIMP	$\mathrm{Br}^-$	CH <sub>3</sub> CN	2029, 1943, 1923	1981, 1949, 1901, 1882, 1862	1929, 1824	[80]
	IPIMP	$_{\mathrm{H_2O}}{}^{b}$	CH <sub>3</sub> CN	2049, 1959(br) <sup>f</sup>			[80]
45	DIPIMP	Br <sup>-</sup>	CH <sub>3</sub> CN	2028, 1944, 1922		1929, 1829/1822	[80]
	DIPIMP	$H_2O^b$	CH <sub>3</sub> CN	2050, 1960(br) <sup>f</sup>			[80]
46	TBIMP	Br <sup>-</sup>	CH <sub>3</sub> CN	2029, 1945, 1923		1928, 1823	[80]
47	TBIEP	Br <sup>-</sup>	CH <sub>3</sub> CN	2028, 1943, 1917		1922, 1814(br)	[80]
	TBIEP	$_{\mathrm{H_2O}}{}^{b}$	CH <sub>3</sub> CN	2048, 1960, 1954			[80]
61	PNP		CH <sub>3</sub> CN	1852, 1930, 1973			[135]
62	PN	Br <sup>-</sup>	CH₃CN	1880, 1903, 1936			[135]

m = medium, w = wide, br = broad, s = sharp (a) recorded in 0.1 M Bu<sub>4</sub>NPF<sub>6</sub> CH<sub>3</sub>CN electrolyte unless otherwise noted (b) cation (c) reductively deprotonated Mn(bpy(OH(O<sup>-</sup>)(CO)<sub>3</sub>(CH<sub>3</sub>CN)) (d) doubly deprotonated [Mn(bpy(O<sup>-</sup>)<sub>2</sub>(CO)<sub>3</sub>(CH<sub>3</sub>CN)]<sup>-</sup> (e) adsorbed on MWCT electrodes in aq. KHCO<sub>3</sub> electrolyte (0.5 M, pH 8.2) (f) estimated (g) diazonium salt derivative (h) [MnBr( $\kappa^3$ -tpy)(CO)<sub>2</sub>] (i) [Mn( $\kappa^3$ -tpy)(CO)<sub>2</sub>]<sup>-</sup> (j) phen-dione ligand CO<sub>2</sub> adduct (k) confirmed by pulse-radiolysis TRIR (l) 6-coordinate one-electron reduced anion [Mn(OC(O)H)(dtbpy)(CO)<sub>3</sub>]<sup>-</sup> (m) 5-coordinate one-electron reduced radical [Mn(dtbpy)(CO)<sub>3</sub>]<sup>-</sup> (n) in THF (o) 6-coordinate one-electron reduced

## 5. Summary of Mn-based CO<sub>2</sub> reduction catalysts

To summarize the current state-of-the-art in catalytic CO<sub>2</sub> reduction by Mn based molecular catalysts a number of key experimental parameters should be compared to establish a clearly identifiable structure-property relationship to help guide future studies towards an improved understanding and optimization of catalyst properties. Ideally this would require a compilation of such properties as  $TOF_{max}$ , TON,  $\eta$ , protonation-first versus the reduction-first pathway, and product selectivity (CO vs. HCO<sub>2</sub>H vs. H<sub>2</sub>). Unfortunately, only rarely are all desired data reported in a single study but more critically, due to the relative emergent nature of this research topic, researchers are still mastering these criteria. For example, catalyst TOF's are often reported incorrectly as TOF<sub>max</sub> without establishing steady-state state electrocatalytic conditions (Section 4.1.1), and with recent improvements in the understanding of non-aqueous pH equilibria [73] many reports of  $\eta$  need revising (Section 3). The goal of this manuscript has not only been to review our current understanding of the mechanistic aspects and spectroscopic properties of Mn catalyzed CO<sub>2</sub> reduction reactions, but also to highlight the standard experimental methods required to accurately report the above list of catalyst properties to enable a cross-literature examination of these catalysts side-by-side. We acknowledge that this is an already recognized challenge, not only in the field of CO<sub>2</sub> reduction catalysis, which a number of our peers have already addressed with some success [15, 69, 72-74, 84, 136]. With this in mind, this summary section is designed to highlight the major findings in both electrochemical and photochemical driven CO<sub>2</sub> reduction catalysis by Mn-based catalysts with a comprehensive set of tabulated data to be used as a reference for experimental conditions employed with a specific catalyst. Only where accurately determined, as set out in Section 4.1.1 will TOF<sub>max</sub> be tabulated.

### 5.1. Electrocatalysis

In 2011, Chardon-Noblat, Deronzier, and co-workers first reported the electrocatalytic activity of MnBr(bpy')(CO)<sub>3</sub> (where bpy' = 2,2'-bipyridine or 4,4'-dimethyl-2,2'-bipyridine) for the selective reduction of CO<sub>2</sub> to CO in CH<sub>3</sub>CN, with the pioneering discovery that the stoichiometric addition of a Brønsted acid is required to observe catalytic current [35]. This work has since inspired a number of researchers to further pursue MnX( $\alpha$ -diimine)(CO)<sub>3</sub> catalysts as a greener alternative to their traditionally more popular Re congeners by taking a variety of approaches such as (i)  $\alpha$ -diimine ligand modification, (ii) monodentate ligand 'L' modification, (iii) protic and aprotic Lewis acid dependence, (iv) supramolecular assembly, and (v) catalyst immobilization, each of which are discussed below.

# 5.1.1 $\alpha$ -diimine ligand modification

The MnBr(bpy)(CO)<sub>3</sub> precatalyst (**2**) is commonly reported as a baseline for comparison to a variety of structural analogues, or often just variations in electrocatalytic conditions. Early studies of MnBr(α-diimine)(CO)<sub>3</sub> precatalysts have ranged from the investigation of simple inductive effects at the bpy ligand using the commercially available dmb or dtbpy ligands in **3** and **7** [35, 57], to the introduction of protic functionality on the bpy backbone with the dhbpy ligand in **22** and the 4,4'-dicarboxy-2,2'-bipyridine (dcbpy) ligand in **35** (Fig. 21) [95].

**Figure 21.** Molecular structures of the MnBr(dcbpy)(CO)<sub>3</sub> pre-catalyst reported by Cowan and co-workers [95].

The strong inductive influence of the dtbpy ligand had earlier gained recognition for stabilizing the five-coordinate Re'(dtbpy)(CO)<sub>3</sub> radical. While dtbpy does not hinder [Mn<sup>0</sup>(dtbpy)(CO)<sub>3</sub>]<sub>2</sub> formation, it does appear to induce a significant increase in catalytic current density relative to bpy and dmbpy, albeit at the cost of a cathodic shift in overpotential (Table 3, entry 7) [57]. From the numerous examples of electrocatalytic CO<sub>2</sub> reduction available for the bpy-based pre-catalyst 2, the greatest selectivity (FE<sub>CO</sub> = 100%, TON<sub>CO</sub> = 13) was reported by Chardon-Noblat, Deronzier and co-workers (Table 3, entry 1) [35], whereas the best stability was later reported by Cowan and co-workers (FE<sub>CO</sub> = 51%, TON<sub>CO</sub> = 471) albeit immobilized in a Nafion membrane with an aqueous electrolyte (Table 3, entry 52) [137]. The dmbpy-based precatalyst 3 exhibits a comparable selectivity with a slightly improved stability (FE<sub>CO</sub> = 100%,  $TON_{CO} = 34$ ) in homogeneous conditions (Table 3, entry 6) [35]. The dtbpy-based pre-catalyst 7 also exhibits quantitative CO formation (FE<sub>CO</sub> = 100%) [57]; unfortunately TON<sub>CO</sub> was not reported under homogeneous conditions for comparison, but when immobilized in a Nafion film with an aqueous electrolyte,  $TON_{CO} = 46.1$  was obtained albeit with a reduced selectivity (FE<sub>CO</sub> = 71%) due to competitive formation of HCO<sub>2</sub>H (Table 3, entry 54) [95]. 22 and 35 were primarily investigated for catalytic CO<sub>2</sub> reduction post immobilization by Cowan and co-workers in the same study with a Nafion membrane and aqueous electrolyte, but suffered from very low TONs for CO (Table 3, entries 55 & 56) [95].

Compain, Chardon-Noblat, and co-workers have reported on the electrocatalytic activity of two [Mn(phen-dione)(CO)<sub>3</sub>L]<sup>n</sup> complexes (**36** and **37**) for CO<sub>2</sub> reduction, where phen-dione is the non-innocent 1,10-phenanthroline-5,6-dione ligand and L = Br<sup>-</sup> (n = 0) or CH<sub>3</sub>CN (n = +1,

PF<sub>6</sub><sup>-</sup> salt) [103]. Both **36** and **37** exhibit two sequential reversible one-electron reduction events under 1 atm Ar at -0.55 V, -1.31 V and -0.40 V, -1.14 V vs Ag/AgNO<sub>3</sub>, respectively. In contrast to traditional MnX( $\alpha$ -diimine)(CO)<sub>3</sub> complexes, these redox couples were assigned to the non-innocent phen-dione ligand which is comparable to the *o*-quinone/*o*-semiquinone/*o*-hydroquinone system (Scheme 6).

**Scheme 6.** Sequential one-electron reductions of the phen-dione ligand in complexes **36** and **37** reported by Compain, Chardon-Noblat and co-workers [103].

Consistent with the ligand-based redox chemistry of **36** and **37**, distinct reactivity is observed under 1 atm of CO<sub>2</sub> where coupling of the oxyanion of the one-electron reduced and two-electron reduced ligand with CO<sub>2</sub> results in the formation of a mono- and bis-carbonate ligand, respectively (Scheme 7).

**Scheme 7.** Sequential one-electron reductions of the phen-dione ligand in complexes **36** and **37** under 1 atm of CO<sub>2</sub> in the absence of a proton source reported by Compain, Chardon-Noblat, and co-workers [103].

While the latter appears to be non-catalytic, consistent with prior reports of the free phendione ligand [138], further reduction at more negative potential gives rise to a catalytic wave at – 1.50 V vs. Ag/AgNO<sub>3</sub>, likely due to activation of the Mn center towards CO<sub>2</sub> reactivity. Further voltammetry studies under 1 atm of CO<sub>2</sub> but in the presence of 2.78 M H<sub>2</sub>O showed that the first two reduction steps merge to a concerted two-electron process (likely due to proton-coupled reduction of the phen-dione ligand), with catalytic current observed at –1.80 V vs Ag/AgNO<sub>3</sub> attributed to formation of the [Mn(phen(OC(O)(OH)<sub>2</sub>)(CO)<sub>3</sub>]<sup>-</sup> active catalyst. Controlled potential electrolysis experiments in 0.1 M BuN<sub>4</sub>PF<sub>6</sub> + 2.78 M H<sub>2</sub>O CH<sub>3</sub>CN electrolyte under 1 atm of CO<sub>2</sub> at an applied potential of –1.70 V vs Ag/AgNO<sub>3</sub> (Table 3, entries 15 & 16) exhibited a high selectivity for CO for the first 7 h (FE<sub>CO</sub> = 100%), whereas an increased H<sub>2</sub>O concentration of 5.56 M resulted in FE<sub>CO</sub> dropping to 40%.

For reference in the latter study, the authors also reported the MnBr(phen)(CO)<sub>3</sub> complex **38** (Fig. 22) which exhibits the more typical voltammetry of MnX( $\alpha$ -diimine)(CO)<sub>3</sub> complexes, with an irreversible Mn(0/I) couple occurring at -1.52 V vs. Ag/AgNO<sub>3</sub> resulting in [Mn(phen)(CO)<sub>3</sub>]<sub>2</sub> dimer formation ( $E_{pa} = -0.48$  V vs Ag/AgNO<sub>3</sub>), followed by a second irreversible one-electron reduction at -1.81 V vs Ag/AgNO<sub>3</sub>. Attempts to prepare the [Mn(phen)(CO)<sub>3</sub>]<sub>2</sub> dimer by in-situ controlled potential electrolysis were unsuccessful, leading the authors to conclude that instability of the dimer is responsible for a poor Faradaic efficiency for CO production in the presence of CO<sub>2</sub> and H<sub>2</sub>O (Table 3, entry 14) [103].

**Figure 22.** Molecular structures of the MnBr(phen)(CO)<sub>3</sub> pre-catalyst **38** reported by Compain, Chardon-Noblat and co-workers [103].

With the limited commercial availability of bpy ligands, researchers have also explored the synthesis of novel bpy derivatives where functionality has been tailored to explore different facets of Mn redox chemistry and/or aspects of the CO<sub>2</sub> reduction catalytic cycle itself. For example, Sampson et al. demonstrated how the steric bulk of the mes<sub>2</sub>bpy ligand in **14** and **15** prevents competitive formation of the Mn<sup>0</sup>–Mn<sup>0</sup> dimer complex (see Section 4.1.3), enhancing the TOF<sub>max</sub> for CO formation (Table 3, entries 17 - 19) [64]. In contrast to earlier protic functionality on the backside of the bpy ligand, distant from the catalytic center in **22** and **35**, Franco et al. [139] and Agarwal et al. [42] have both independently reported on the introduction of a pendant hydroxyphenyl group in the second coordination sphere of the Mn center using the pdbpy and HOPhbpy ligands in pre-catalysts **20** (Fig. 15) and **9** (Fig. 3), respectively.

Interestingly, in addition to a 70% Faradaic efficiency for CO (FE<sub>CO</sub>), **20** exhibits a FE<sub>HCO2H</sub> = 22% for formic acid in CH<sub>3</sub>CN electrolyte in the absence of any added Brønsted acid, suggesting the formation of an intermediate Mn–H intermediate via the pendant hydroxyl group in close proximity to the Mn active site (Table 3, entry 32) [139]. While the related study by Agarwal et al. only reported on CO production (FE<sub>CO</sub> = 86%) by **9** (Table 3, entry 26), they provided computational evidence for intramolecular hydrogen bonding in the rate-determining

transition state between the second-coordination sphere hydroxyl group of the HOPhbpy ligand and the Mn-COOH intermediate that was predicted to lower the activation energy for critical C-OH bond cleavage via proton-assisted dehydration of Mn-COOH (see Section 2.1). More recently, Ngo et al. reported similarly on the electrocatalytic reduction of CO<sub>2</sub> to CO by 13, which enhanced the TOF<sub>max</sub> of the lower overpotential protonation-first pathway (see Section 2.1) [47]. In the this case, the presence of a pendant methoxy Lewis base functionality, in combination with a Brønsted acid of suitable  $pK_a$  (TFE or PhOH) in CH<sub>3</sub>CN located in close proximity to the Mn-COOH intermediate, enables weak hydrogen bonding, effectively lowering the activation free energies of the rate-determining C-OH bond cleavage step. This study also confirmed that growth of catalytic current for the *protonation-first* pathway occurs directly from the two-electron reduced active catalyst, whereas an added overpotential (0.55 V) is required for observation of catalytic current for the reduction-first pathway. In hindsight, it can also be postulated that the low-overpotential protonation-first pathway was also accessed by precatalysts 9 and 20 with respect to CO evolution via the local availability of an intramolecular proton source [42, 139]. Controlled potential electrolysis studies by Ngo et al. for both 13 and 15 were conducted in the presence of a variety of Brønsted acids and are discussed in detail in Section 5.1.3 (Table 3, entries 22 - 25 & 28 - 31) [47].

A select few studies have deviated from the traditional 2,2-bipyridyl ligand scaffold by investigating asymmetric ligands in their catalyst design. The MnBr(N-C)(CO)<sub>3</sub> class of precatalysts, where N-C = N-methyl-N'-2-pyridylbenzimidazol-2-ylidine (**39**) or N-methyl-N'-2-pyridylimidazol-2-ylidine (**40**), were first reported by Agarwal et al. in 2014 (Fig. 23) [78]. Both catalysts exhibit selective CO formation in CH<sub>3</sub>CN electrolyte with 5% H<sub>2</sub>O albeit with poor

Faradaic efficiencies (FE<sub>CO</sub> < 35%, Table 3, entry 40). To counter the strong electron donation influence of the NHC ligand, the same authors later improved upon this catalytic activity by replacing pyridine with the more  $\pi$ -acidic pyrimidine ring in **42** (Fig. 23), leading to a 0.16 V anodic shift in catalyst activation which serendipitously also improved upon the selectivity for CO production (FE<sub>CO</sub> = 72 %, Table 3, entry 43) [79].

**Figure 23.** Molecular structures of asymmetric MnBr(N-C)(CO)<sub>3</sub> CO<sub>2</sub> reduction catalysts **39** – **42** reported by Agarwal and co-workers where N-C is a pyridyl or pyrazine containing *N*-heterocyclic carbene ligand [78, 79].

Hartl, Weinstein, and co-workers more recently reported on the electrocatalytic  $CO_2$  reduction properties of a series of asymmetric  $MnBr(IP)(CO)_3$  complexes 43 - 47, where IP is a 2-(phenylimino)pyridine ligand (Fig. 24) [80]. Imine substituents were here used to tune the redox properties of the Mn(I) center while 2,6-phenyl substituents at the  $\alpha$ -diimine were used to introduce steric bulk to inhibit  $Mn^0$ – $Mn^0$  dimer formation. Both CO and  $HCO_3$ <sup>-</sup> were observed as products of electrocatalysis in wet (4.7 %  $H_2O$ )  $CH_3CN$  (Table 3, entries 44 - 48).

**Figure 24.** Molecular structures of the MnBr( $\alpha$ -diimine)(CO)<sub>3</sub> CO<sub>2</sub> reduction precatalysts reported by Hartl, Weinstein and co-workers where  $\alpha$ -diimine is an asymmetric 2-iminopyridyl (IP) ligand [80].

In two related but independent studies it was demonstrated that the absence of aromatic character in the α-diimine ligand of MnL(α-diimine)(CO)<sub>3</sub> precatalysts can cause rapid catalyst decomposition or even turn off catalyst activity altogether (see Section 4.1.3, Fig. 16) [99, 100]. It is also worth noting that in a 2015 study by Mukhopadhyay et al. of the MnBr(Ph2PPrPDI)(CO)<sub>3</sub> precatalyst **48** (Fig. 25), where Ph2PPrPDI is a pentachelating phosphine-substituted pyridine diimine ligand, only quanitative H<sub>2</sub> evolution was observed, attributed to a lowering of the electrolyte pH due to carbonic acid formation by dissolved CO<sub>2</sub> [140].

The Kubiak group later succeeded in attaching the  $\kappa^3$ -tpy ligand in **49** which exhibits a moderate activity for CO evolution alongside the analogous  $\kappa^2$ -tpy complex **50** (Fig. 25) [102]. Both **49** and **50** exhibited selective CO production, with the  $\kappa^2$ -tpy also evolving a bound CO ligand (perhaps forming the  $\kappa^3$ -complex in-situ), resulting in a Faradaic efficiency of 129%. This anomaly is explained by the large impact CO ligand loss can have on FE<sub>CO</sub> when the TON is very low due to poor catalyst stability (Table 3, entries 12 & 13).

In contrast, Richeson and co-workers later demonstrated selective CO production (FY = 96%) for a MnBr(PNP)(CO)<sub>3</sub> precatalyst **51** (Fig. 25), where PNP is the tridentate N,N'-bis(diphenylphosphino)-2,6-di(methylamino)pyridine pincer ligand (Table 3, entry 49) [135]. Interestingly, catalytic current grows-in upon just one-electron reduction of **51**, quantitatively producing CO and  $CO_3^{2-}$  in anhydrous 0.1 M Bu<sub>4</sub>NPF<sub>6</sub> CH<sub>3</sub>CN electrolyte. It is conceivable that the two-electron reduction of CO<sub>2</sub> here occurs via disproportionation of the one-electron reduced Mn<sup>\*</sup>(PNP)(CO)<sub>3</sub> intermediate. However, the mechanism or active catalyst species was not probed in any detail. Addition of 5% H<sub>2</sub>O to this system resulted in a decrease in product selectivity due to competitive H<sub>2</sub> evolution (FE<sub>H2</sub>= 41%), consistent with formation of a Mn–H intermediate under acidic conditions. The related MnBr(PN)(CO)<sub>3</sub> catalyst **52**, where PN is the asymmetric *N*-(diphenylphosphino)-2-(methylamino)pyridine bidentate ligand, only exhibited catalytic current in wet (5% H<sub>2</sub>O) CH<sub>3</sub>CN electrolyte, again with competitive H<sub>2</sub> evolution (Table 3, entry 51) [135].

**Figure 25.** Molecular structure of the MnBr( $\kappa^5$ -NNN-PP)(CO) pincer complex **48** reported by Mukhopadhyay et al. [140] alongside the MnBr( $\kappa^3$ -tpy)(CO)<sub>2</sub> (**49**) and MnBr( $\kappa^2$ -tpy)(CO)<sub>3</sub> (**50**)

complexes reported by Kubiak and co-workers [102], and the [Mn(PNP)(CO)<sub>3</sub>](Br) and [MnBr(PN)(CO)<sub>3</sub>] complexes reported by Richeson and co-workers [135].

## 5.1.2 Monodentate ligand 'L' modification.

While 2 is by far the most often utilized Mn-based pre-catalyst due to its ease of preparation from commercially available MnBr(CO)<sub>5</sub>, we want to take this opportunity to encourage researchers the alternative cationic CH<sub>3</sub>CN solvated to use pre-catalyst,  $[Mn(bpy)(CO)_3(CH_3CN)]^+$ , or  $\alpha$ -dimine derivatives thereof, for reference studies (e.g., Section 3.1, Fig. 10). Previous reports have shown that the bromide ligand in MnBr( $\alpha$ -diimine)(CO)<sub>3</sub> is typically replaced by CH<sub>3</sub>CN via solvolysis, generating a mixture of Faradaic responses due to the additional presence of  $[Mn(\alpha-diimine)(CO)_3(CH_3CN)]^+$  [35, 80]. Preparation of  $[Mn(\alpha-diimine)(CO)_3(CH_3CN)]^+$ diimine)(CO)<sub>3</sub>(CH<sub>3</sub>CN)] $^{+}$ X $^{-}$ complexes is relatively straightforward via the  $[Mn(CO)_5(CH_3CN)]^+X^-$  intermediate [47, 107], where  $X^-$  = triflate  $(OTf^{-})$ hexafluorophosphate (PF<sub>6</sub><sup>-</sup>), and in our experience the extra effort made at this stage of an electrocatalysis investigation saves many complications in the long-term when trying to assign the complex redox chemistry observed in cyclic and linear sweep voltammetry. Reports on substituting the monodentate L ligand to an alternative other than the bromide anion are limited, but this approach can reap significant rewards from a catalytic viewpoint. For example, as discussed earlier (Section 4.1.3), Kubiak, Agarwal, and co-workers used IR-SEC studies of 23 to hypothesis disproportionation of the one-electron support their for reduced [Mn(CN)(bpy)(CO)<sub>3</sub>] - species to generate the two-electron reduced active catalyst,  $[Mn(bpy)(CO)_3]^-$ , which exhibited selective CO formation (FE<sub>CO</sub> = 98%, Table 3, entry 4) [96].

Thus, catalytic current grew in upon just one-electron reduction of **23**, priming this system for a subsequent photocatalysis study (see Section 5.2).

#### 5.1.3 Brønsted and Lewis acid dependence

As highlighted throughout this review, addition of a Brønsted acid is typically critical for the generation of catalytic current for CO<sub>2</sub> reduction to CO or HCO<sub>2</sub>H with Mn-based catalysts. While the majority of studies have opted to simply add 5% H<sub>2</sub>O (2.78 M) to a CH<sub>3</sub>CN-based electrolyte, some studies have explicitly investigated the influence of Brønsted acid concentration and  $pK_a$  on the catalytic current density, specifically in the case of selective CO production. In each case, a very strong dependence of TOF<sub>max</sub> has been observed due to the critical role protonation plays in the rate-determining C-OH bond cleavage step from the Mn-COOH intermediate, whether it be via the protonation-first or reduction-first pathway. A detailed thermodynamic discussion of this Brønsted acid dependence has already been presented in Section 2.1. However, it suffices to say enhanced catalytic activity is typically observed, as anticipated, with a greater availability of protons due to either an increased Brønsted acid concentration or use of an acid with lower  $pK_a$ . A major challenge in these studies has been how catalyst solubility (and possibly stability) has restricted investigations to non-aqueous electrolytes and there is only limited knowledge of non-aqueous Brønsted acid p $K_a$  values. In fact, only select pK<sub>a</sub> values have been reported in CH<sub>3</sub>CN and trends are often speculated from Brønsted acid p $K_a$  values reported in DMSO. The most commonly utilized Brønsted acids to date have been  $H_2O$  (p $K_{a(DMSO)} = 31.4$  [141]; p $K_{a(CH3CN)}$  not reported, n.r.), MeOH (p $K_{a(DMSO)} = 29.0$ [141];  $pK_{a(CH3CN)}$  n.r.), TFE ( $pK_{a(DMSO)} = 23.5$  [142];  $pK_{a(CH3CN)} = 35.4$  est. [43]), and PhOH  $(pK_{a(DMSO)} = 18.0 [143]; pK_{a(CH3CN)} = 29.1 [144])$ . Kubiak and co-workers were the first to

investigate MeOH and TFE in combination with 7 following the reduction-first pathway for CO evolution, where they found 5.8 M MeOH to behave similarly to 3.1 M H<sub>2</sub>O [57]. However, a two-fold increase in catalytic current was observed with just 1.4 M TFE, consistent at least with their p $K_a$  trends in DMSO (Table 3, entries 7 - 9). The same group later reported on the Brønsted acid dependence with H<sub>2</sub>O, MeOH and TFE in combination with their bulky 14 and 15 precatalysts, again for the reduction-first CO evolution pathway [64]. MeOH at 3.2 M only showed a slight increase in catalytic current relative to 3.5 M H<sub>2</sub>O, with TFE again surpassing both with an almost two-fold increase in catalytic current at just 1.4 M concentration (Table 3, entries 17 -19). Ngo et al. reported the same 15 pre-catalyst to exhibit yet another two-fold increase in efficiency upon switching to PhOH as a proton source (Table 3, entries 22 - 25) [47]. As highlighted earlier in this review, the focus of the latter study was upon distinguishing the protonation-first and reduction-first pathways for CO evolution by the 13 pre-catlayst, which contains four pendant methoxy groups in its second coordination sphere. In contrast to precatalysts 9, 20 and 21 which have protic hydroxyl groups in their second coordination sphere, use of an aprotic pendant Lewis base appears to avoid a Mn–H intermediate synonymous with HCO<sub>2</sub>H production, thus improving upon CO product selectivity (Table 3, entries 28 - 31). This was however, highly dependent upon the pKa of the Brønsted acid used, with Faradaic efficiencies of CO evolution for the reduction-first pathway reported as FE<sub>CO</sub> = 61%, 99%, 100% and 85% alongside only competitive H<sub>2</sub> evolution, using H<sub>2</sub>O (6.33 M), MeOH (2.09 M), TFE (2.13 M) and PhOH (1.37 M) Brønsted acids, respectively [47]. Under identical conditions for 13, H<sub>2</sub>O and MeOH were ineffective at promoting the lower overpotential protonation-first pathway, which only occurred appreciably in the presence of TFE or PhOH (FE $_{CO}$  = 88%; Table 3, entries 30 & 31) [47].

Gobetto, Nervi, and co-workers recently expanded upon the scope of Brønsted acids (H<sub>2</sub>O plus TFE and PhOH), as well as the number of hydroxyl groups in their earlier catalyst **20**, by introducing a third pendant hydroxyl group on the phenyl substituent in the MnBr(ptbpy)(CO)<sub>3</sub> pre-catalyst **21** [94]. The authors concluded that the Brønsted acid dependence of the different protic sites in the **20** and **21** complexes led to the existence of competing electrocatalytic pathways, reducing product selectivity but with accountable FE's for both CO and HCO<sub>2</sub>H. Water addition favored CO production over HCO<sub>2</sub>H, while the stronger TFE and PhOH Brønsted acids improved turnover of the Mn–H intermediate and enhanced production of HCO<sub>2</sub>H (Table 3, entries 32 - 39). A complex series of reactions were proposed based upon a detailed IR-SEC study of both **20** and **21** (see Section 4.1.3), where evidence for Mn–H formation was presented.

Alternative to Brønsted acid addition to promote CO evolution, and inspired by prior independent studies by Savéant and Fujita [145, 146], Kubiak and co-workers have capitalized on the use of  $Mg^{2+}$  [92] and  $[Zn(cyclam)]^{2+}$  [147] (cyclam = 1,4,8,11-tetraazacyclotetradecane) Lewis acids with their established pre-catalysts **14** and **15**. It was found that the sacrificial  $Mg^{2+}$  co-reagent promotes a low overpotential reductive disproportionation mechanism, second order in  $CO_2$ , to produce one equivalent of CO ( $FE_{CO} = 98\%$ ) and one equivalent of the insoluble  $Mg(CO_3)$  salt, thus requiring a sacrificial elemental CO (CO) and one equivalent of the insoluble turnover (Table 3, entry 20). In contrast, the CO(CO) salt, maintaining the CO(CO) salt in solution to contribute in a co-catalytic fashion, producing CO0 with 80% selectivity (Table 3, entry 21).

## 5.1.4 Supramolecular assembly

Based on an approach more synonymous with photosensitizer-catalyst assemblies for artificial photosynthesis and photocatalysis, Machan et al. used hydrogen-bonding interactions between the acetamidomethyl groups of the dacbpy ligands of both **16** and **17** (Fig. 14) to support non-covalent self-assembly of a heterobimetallic supramolecular Re and Mn dimer for electrocatalytic CO<sub>2</sub> reduction to CO [93]. While only a 10% enhancement in catalytic current was attributed to the self-assembled dimer, voltammetry and IR-SEC studies (Section 4.1.3) provided evidence for a one-electron reduced Re<sup>0</sup>(dacbpy)(CO)<sub>3</sub> center and a two-electron reduced [Mn(dacbpy)(CO)<sub>3</sub>]<sup>-</sup> center in the heterobimetallic dimer. The authors ultimately concluded that CO evolution occurred by the *reduction-first* pathway, however, facilitated at a lower overpotential by intramolecular electron transfer to a Mn<sup>1</sup>-CO<sub>2</sub>H intermediate from the one-electron reduced Re<sup>0</sup> center (Table 3, entries 10 & 11). Such synergistic behavior by a heterometallic dimeric catalyst is rare and may inspire future catalyst design to tackle the high overpotential barriers of CO<sub>2</sub> reduction.

# 5.1.5 Catalyst immobilization

Although there is still some way to go yet with respect to the fundamental development of efficient (high TOF<sub>max</sub>, low  $\eta$ ) and robust (high TON) homogeneous MnX( $\alpha$ -diimine)(CO)<sub>3</sub>-based CO<sub>2</sub> reduction catalysts, there have already been a few reports where these catalysts have been immobilized in a heterogeneous fashion at a solid-state interface. To clarify, our definition of homogeneous and heterogeneous here applies to the relative phases of the catalyst and CO<sub>2</sub>

substrate. All examples discussed thus far in Section 5.1 are considered homogeneous by the latter definition even though diffusion-dependent electron-transfer from the working electrode to the dissolved catalyst is a heterogeneous process.

The first reported example of a heterogeneous electrocatalytic study of a MnX( $\alpha$ diimine)(CO)<sub>3</sub>-based CO<sub>2</sub> reduction catalyst was by Cowan and co-workers in 2014 where 2 was cast into a Nafion® membrane at a glassy carbon working electrode [137]. The hydrophobicity of 2 allowed the authors to utilize an aqueous electrolyte for the first time with this class of catalyst (pH 7, 30 mM Na<sub>2</sub>HPO<sub>4</sub> + 30 mM NaH<sub>2</sub>PO<sub>4</sub>) without any catalyst leaching. Catalytic current attributed to a 1:2 mixture of CO and H<sub>2</sub> gas was initially limited due to the low concentration (0.25%) of 2 in the Nafion® membrane. Interestingly, this fabricated working electrode could be re-used with sustained catalytic current. Although the Faradaic yield of CO declined over time, this was attributed not to catalyst decomposition but to degradation of the glassy carbon/Nafion® membrane contact and a record TON of 471 was reported over a 4 h period, representing an order of magnitude improvement relative to any homogenous Mn-based electrocatalyst reported to date, highlighting a major advantage for this immobilization strategy (Table 3, entry 52). To address the low Mn concentration, the authors introduced multi-walled carbon nanotubes (MWCNTs) in an equimolar concentration with respect to 2, giving rise to a maximum Mn concentration of 11% in their optimum Nafion® membrane. A ten-fold increase in catalytic current was observed by cyclic voltammetry (3 mA cm<sup>-2</sup> at  $v = 0.01 \text{ V s}^{-1}$ ) at an applied potential of -1.4 V vs NHE ( $\eta = 0.88$  V @ pH = 7). A follow-up study by the same group identified that the more hydrophilic debpy and dhbpy ligands caused a decrease in catalytic activity relative to the 2/MWCNT/Nafion® electrode, the latter even outperforming the more electron rich dmbpy

analogue 3 and exhibiting the best catalytic current density (J = 4.38 mA cm<sup>-2</sup>) at an applied potential of -1.5 V vs NHE ( $\eta = 0.98$  V @ pH = 7) with product selectivities of FE<sub>CO</sub> = 52% and FE<sub>H2</sub> 11% (Table 3, entries 53 - 57) [95].

In 2017, Nervi and co-workers succeeded in the covalent attachment of both **53** and **54** (Fig. 26) to the surface of a glassy carbon electrode using the 4-(4-aminophenyl)-2,2'-bipyridine (apbpy) ligand [134]. Both **53** and **54** pre-catalysts could be incorporated onto modified glassy carbon electrodes by formation of either a new interfacial C–N bond via electrochemical oxidation of the pendent amine group or alternatively by diazonium salt derivatization of the amino group and subsequent electrochemical reduction to form a new interfacial C–C bond. Subsequent CV studies under an inert atmosphere proved the C–C bond to be more stable, especially in the case of the Mn-based catalyst. Using a glassy carbon electrode of 6.24 mm<sup>2</sup> area (2.82 mm diameter), under 1 atm of CO<sub>2</sub> in a 0.1 M Bu<sub>4</sub>NPF<sub>6</sub> + 4.94 M MeOH (20%) CH<sub>3</sub>CN electrolyte, a maximum  $i_{cat}/i_p$  ratio of 24 was observed with a maximum TON of 360 for CO production (FE<sub>CO</sub> = 75%) recorded upon controlled potential electrolysis at –1.75 V vs Fc<sup>0/+</sup> (Table 3, entries 62 - 65). Again, this represents a significant improvement over the homogeneous catalysts discussed above. The Re analogue performed slightly better in the absence of a Brønsted acid, with a TON of 402 (FE<sub>CO</sub> = 75%).

Reisner and co-workers have recently reported on the fabrication and electrochemical characterization of FTO/MO/55 electrodes using the 4,4'-bis(phosphonic acid)-2,2'-bipyridine ligand (bpabpy, Fig. 26), where FTO is a conductive fluorine-doped tin oxide glass surface, MO (metal oxide) is a semiconducting *n*-type TiO<sub>2</sub> or a conducting ITO (tin-doped indium oxide)

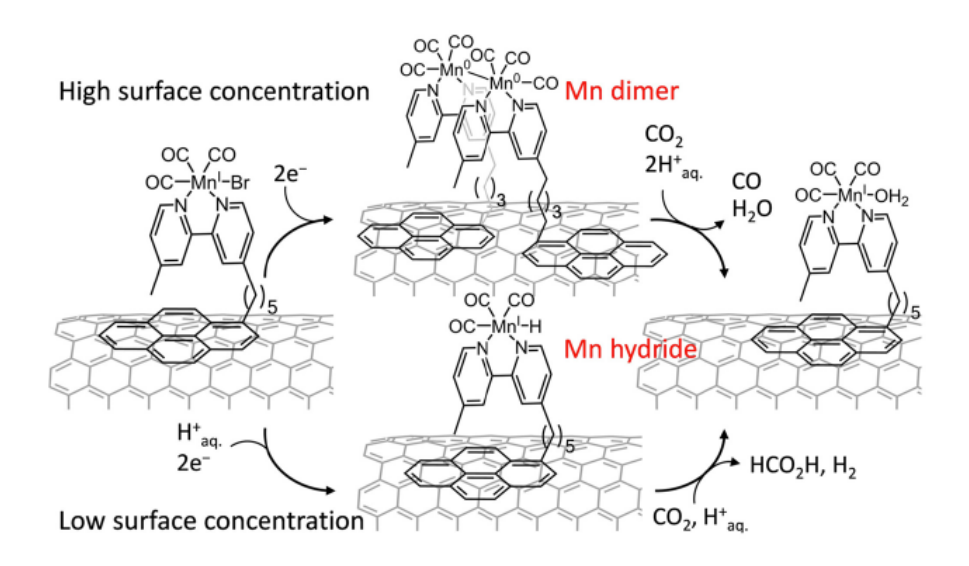
*mesoporoous* nanoparticle metal oxide thin film (6-7 μm thickness, 1.0 cm<sup>2</sup> area) [133]. Only the FTO/TiO<sub>2</sub>/**55** electrode was investigated for CO<sub>2</sub> reduction properties. With a pre-catalyst surface coverage of 34 nmol cm<sup>-2</sup> at the TiO<sub>2</sub> interface, a four-fold enhancement in current was observed at -1.7 V vs Fc<sup>+/0</sup> under 1 atm CO<sub>2</sub> in 0.1 M Bu<sub>4</sub>NPF<sub>6</sub> + 2.78 M H<sub>2</sub>O (5%) CH<sub>3</sub>CN electrolyte. Controlled potential electrolysis, also conducted at -1.7 V vs Fc<sup>+/0</sup> under identical electrolyte conditions for a 2 h period, resulted in a TON of 112 (± 17) for CO production, with yields of FE<sub>CO</sub> = 67 (± 5)% and FE<sub>H2</sub> = 12.4 (± 1.4)% (Table 3, entry 59). UV-Vis-SEC and IR-SEC studies indicated the Mn<sup>0</sup>–Mn<sup>0</sup> dimer to be the active catalyst at the surface (see Section 4.1.3). Impressively, this system could also be driven photo-electrochemically (see Section 5.2).

$$H_2N$$
 $H_2N$ 
 $H_3P$ 
 $H_3P$ 

**Figure 26.** Molecular structures of the MX(apbpy)(CO)<sub>3</sub> pre-catalysts **53** and **54** reported by Nervi and co-workers [134] for immobilization on glassy carbon electrodes, alongside the MnBr(bpabpy)(CO)<sub>3</sub> (**55**) structure reported by Reisner and co-workers [133] for immobilization on mesoporous TiO<sub>2</sub>.

Reisner and co-workers later used a modified glassy carbon multiwall carbon nanotube (MWCNT) electrode, taking advantage of established  $\pi$ - $\pi$  self-assembly of pyrene at the CNT surface, to immobilize pre-catalyst **30** using the bpy<sub>pyr</sub> ligand (Fig. 17, Scheme 8) [104]. Using a

CO<sub>2</sub> saturated aqueous 0.5 M KHCO<sub>3</sub> (pH = 7.4) electrolyte, electrocatalytic reduction of CO<sub>2</sub> exhibited both CO and HCO<sub>2</sub>H evolution with product selectivity tuned by the surface coverage of the Mn complex (Table 3, entry 61). UV-Vis-SEC and IR-SEC studies (see Section 4.1.3) indicated how at high-surface loading, a Mn<sup>0</sup>-Mn<sup>0</sup> dimer was implicit in CO evolution, while at reduced surface loading a Mn-H intermediate prevailed, which is active for HCO<sub>2</sub>H production (Scheme 8). Most impressive for this system was the improved stability of the catalyst, with maximum TON<sub>CO</sub> = 1790 ± 290 and TON<sub>HCO2H</sub> = 3920 ± 230 at an applied potential of -1.1 V vs SHE ( $\eta_{CO} = 0.55$ V,  $\eta_{HCO2H} = 0.59$ V).



**Scheme 8.** Concentration-dependent Mn–Mn dimerization of precatalyst **30** at carbon nanotubes was used by Reisner and co-workers to control CO versus HCO<sub>2</sub>H product selectivity [104].

**Table 3:** A summary of electrochemical and controlled potential electrolysis data for reported  $MnX(\alpha$ -diimine)(CO)<sub>3</sub> CO<sub>2</sub> reduction catalysts.

					Voltamme	try	Controlled Potential Electrolysis <sup>b</sup>						
		MnX(L <sub>2</sub> )(CO) <sub>3</sub>		1 atm of N2 or Ar			1 atm CO <sub>2</sub> a						
Table Entry	Catalyst Number	$L_2$	X	Conditions	Reference	$E_{pc}$ (V) $^c$	Acid (M)	$i_{\text{cat}}/i_{\text{p}}$ (v, V s-1)	TOF <sub>max</sub> d (s <sup>-1</sup> )	Parameters (time, potential)	FE (%) (CO:HCO <sub>2</sub> H:H <sub>2</sub> )	TON (CO:HCO <sub>2</sub> H: H <sub>2</sub> )	Reference
1	2	bpy	Br <sup>-</sup>	1 mM Mn; 0.1 M Bu <sub>4</sub> NClO <sub>4</sub> in CH <sub>3</sub> CN	Ag/AgNO <sub>3</sub>	-1.56, -1.80	H <sub>2</sub> O (2.78)	nr	nr	4 h + 18 h -1.70 V	100:nr:0 (85:15 after 4 h)	13:nr:0	[35]
2				1 mM Mn; 0.1 M Bu <sub>4</sub> NClO <sub>4</sub> in CH <sub>3</sub> CN; pH adjusted to 3.7 (HClO <sub>4</sub> )	SCE	-1.09, -1.36 <sup>e</sup>	H <sub>2</sub> O (2.78)	2.7 (0.01)	f	nr	nr	nr	[78]
3				1 mM Mn; 0.1 M Bu <sub>4</sub> NClO <sub>4</sub> + 2.78 M H <sub>2</sub> O in CH <sub>3</sub> CN	SCE	-1.15, -1.40	H <sub>2</sub> O (2.78)	1.6 (0.10)	f	4 h -1.5 V	75:nr:nr	2.7:nr:nr	[42]
4	23	bpy	(CN)-	1 mM Mn; 0.1 M Bu <sub>4</sub> NClO <sub>4</sub> in CH <sub>3</sub> CN	$Fc^{+/0}$	-1.94, -2.51	H <sub>2</sub> O (2.78)	1.2, 5.7 (0.10)	nr	nr	nr	nr	[96]
5							PhOH (1.50)	7.2, n.o. (0.10)	f	nr <sup>h</sup> -2.2 V	98:nr:1	4:nr:0	[96]
6	3	dmbpy	Br <sup>-</sup>	1 mM Mn; 0.1 M Bu <sub>4</sub> NClO <sub>4</sub> in CH <sub>3</sub> CN	Ag/AgNO <sub>3</sub>	-1.64, -1.89	H <sub>2</sub> O (2.78)	n.r.	nr	18 h -1.70 V	100:nr:0	34:nr:0	[35]
7	7	dtbpy	Br <sup>-</sup>	1 mM Mn; 0.1 M Bu <sub>4</sub> NPF <sub>6</sub> in CH <sub>3</sub> CN	SCE	-1.39, -1.57	H <sub>2</sub> O (3.1)	25 (0.10)	f	nr	nr	nr	[57]
8							MeOH (5.80)	26 (0.10)	f	nr	nr	nr	[57]
9							TFE (1.40)	42 (0.10)	f	3 h <sup>i</sup> -2.2 V	100:nr:0	nr	[57]
10	16	dacbpy	Br <sup>-</sup>	1 mM Mn; 0.1 M Bu <sub>4</sub> NPF <sub>6</sub> in CH <sub>3</sub> CN	$Fc^{+/0}$	-1.65, -1.88	PhOH (0.70)	nr	nr	nr -1.75 V	100:nr:0	4.14:nr:0	[93]
11							PhOH (0.75) + <b>18</b>	nr	nr	nr -1.75 V	86:nr:0	4.15:nr:0	[93]
12	49	$\kappa^3$ -tpy $q$	Br <sup>-</sup>	1 mM Mn; 0.1 M Bu <sub>4</sub> NPF <sub>6</sub> in CH <sub>3</sub> CN	$Fc^{+/0}$	-1.56, -1.75	PhOH (2.50)	nr	nr	4 h ° -2.2 V	93:nr:6	4:nr:0.3	[102]
13	50	κ²-tpy	Br <sup>-</sup>	1 mM Mn; 0.1 M Bu <sub>4</sub> NPF <sub>6</sub> in CH <sub>3</sub> CN	$Fc^{+/0}$	-1.56, -1.77	PhOH (2.40)	nr	nr	4 h ° -2.2 V	129 <sup>p</sup> :nr:0	4:nr:0	[102]
14	38	phen	Br <sup>-</sup>	1 mM Mn; 0.1 M Bu <sub>4</sub> NPF <sub>6</sub> in CH <sub>3</sub> CN	Ag/AgNO <sub>3</sub>	-1.52, -1.81	H <sub>2</sub> O (8.34)	nr	nr	7 h -1.90 V	57:nr:33	nr	[103]
15	36	phen-dione	Br <sup>-</sup>	1 mM Mn; 0.1 M Bu <sub>4</sub> NPF <sub>6</sub> in CH <sub>3</sub> CN	Ag/AgNO <sub>3</sub>	-0.58, -1.35	H <sub>2</sub> O (2.78)	nr	nr	7 h -1.70 V	100:nr:nr	nr	[103]

16	37		CH <sub>3</sub> CN (PF <sub>6</sub> ) <sup>-</sup>	1 mM Mn; 0.1 M Bu <sub>4</sub> NPF <sub>6</sub> in CH <sub>3</sub> CN	Ag/AgNO <sub>3</sub>	-0.44, -1.18	H <sub>2</sub> O (2.78)	nr	nr	7 h -1.70 V	100:nr:nr	nr	[103]
6- or 6'-substituted bpy ligands													
17	15	mes2bpy	CH₃CN (OTf)⁻	1 mM Mn; 0.1 M Bu <sub>4</sub> NPF <sub>6</sub> in CH <sub>3</sub> CN	$Fc^{+/0}$	-1.55(2e), -2.25	H <sub>2</sub> O (3.5)	20 (0.10)	700	nr	nr	nr	[64]
18							MeOH (3.2)	30 (0.10)	2000	nr	nr	nr	[64]
19							TFE (1.4)	50 (0.10)	5000	1.17 h <sup>k</sup> -2.2 V	100:nr:0	nr	[64]
20							Mg(OTf) <sub>2</sub> (0.12 M)	3.5 (0.10)	20	1.17 h <sup>/</sup> -1.6 V	98:nr:1	36:nr:0	[92]
21							[Zn(cyclam)] <sup>2+</sup> (0.03 M)	1.5 (3.2)	105	6 h <sup>m</sup> -1.6 V	80:nr:0	nr	[147]
22				1 mM Mn; 0.1 M Bu <sub>4</sub> NPF <sub>6</sub> in CH <sub>3</sub> CN	$Fc^{+/0}$	-1.60(2e), -3.01	H <sub>2</sub> O (5.95)	3.5 (0.50)	93	1 h -2.25 V	73:nr:27	10:nr:4	[47]
23							MeOH (2.09)	3.8 (0.50)	115	1 h -2.26 V	80:nr:6	15:nr:0.4	[47]
24							TFE (2.00)	7.7 (0.50)	1; 453 <sup>n</sup>	1 h <sup>n</sup> -1.65 V -2.32 V	97:nr:2 80:nr:0	n 11:nr:0.2 4:nr:0.4	[47]
										1 h "	n	n	
25							PhOH (2.03)	10.8 (0.50)	3; 910 <sup>n</sup>	-1.75 V -2.77 V	74:nr:21 91:nr:1	1:nr:0.3 7:nr:0.1	[47]
26	9	HOPhbpy	Br <sup>-</sup>	1 mM Mn; 0.1 M Bu <sub>4</sub> NClO <sub>4</sub> + 2.78 M H <sub>2</sub> O in CH <sub>3</sub> CN	SCE	-1.14, -1.30, -1.76	H <sub>2</sub> O (2.78)	10.9 (0.10)	f	4 h -1.5 V	76:nr:nr	2.7:nr:nr	[42]
27	10	MeOPhbpy	Br <sup>-</sup>	1 mM Mn; 0.1 M Bu <sub>4</sub> NClO <sub>4</sub> + 2.78 M H <sub>2</sub> O in CH <sub>3</sub> CN	SCE	-1.21, -1.30	H <sub>2</sub> O (2.78)	2.1 (0.10)	f	4 h -1.5 V	67:nr:nr	0.9:nr:nr	[42]
28	13	6,6'-bis(2,6- (MeO) <sub>2</sub> Ph)bpy	CH <sub>3</sub> CN (OTf) <sup>-</sup>	1 mM Mn; 0.1 M Bu <sub>4</sub> NPF <sub>6</sub> in CH <sub>3</sub> CN	$Fc^{+/0}$	-1.63(2e), -3.10	H <sub>2</sub> O (6.33)	5.9 (0.50)	1; 258 <sup>n</sup>	1 h -2.34 V	61:nr:38	7:nr:4	[47]
29							MeOH (2.09)	5.7 (0.50)	5; 259 <sup>n</sup>	1 h -2.36 V	99:nr:0	18:nr:0	[47]
30							TFE (2.13)	9.4 (0.50)	82; 694 <sup>n</sup>	1 h " -1.63 V -2.36 V	88:nr:13 100:nr:0	2:nr:0.3 9:nr:0	[47]
31							PhOH (1.37)	12.6 (0.50)	138; 1257 <i><sup>n</sup></i>	1 h <sup>n</sup> -1.64 V	n 88:nr:5	4:nr:0.2	[47]
							(1.37)			-2.40 V	85:nr:6	5:nr:0.1	
32	20	pdbpy	Br <sup>-</sup>	1 mM Mn; 0.1 M Bu <sub>4</sub> NPF <sub>6</sub> in CH <sub>3</sub> CN	SCE	-1.20, -1.51, -1.66	none	nr	nr	4 h -1.8 V	70:22:1	19:6:0.3	[139]
33				0.5 mM Mn; 0.1 M Bu <sub>4</sub> NPF <sub>6</sub> in CH <sub>3</sub> CN	SCE	-1.21, -1.50, -1.66	H <sub>2</sub> O (2.70)	nr	nr	2 h -1.5 V	90:4:2	28:1.4:0.7	[94]

34							TFE (2.70)	nr	nr	2 h -1.5 V	48:36:3	11:9:0.8	[94]
35							PhOH (2.70)	nr	nr	2 h -1.5 V	15:39:21	4:12:5.5	[94]
36	21	ptbpy	Br <sup>-</sup>	0.5 mM Mn; 0.1 M Bu <sub>4</sub> NPF <sub>6</sub> in CH <sub>3</sub> CN	SCE	-1.30, -1.64(2e)	none	nr	nr	nr	nr	nr	[94]
37							H <sub>2</sub> O (2.70)	nr	nr	3 h -1.5 V	74:4:2	7:0.5:0.2	[94]
38							TFE (2.70)	nr	nr	0.83 h -1.5 V	74:10:1	2:0.3:0.04	[94]
39							PhOH (2.70)	nr	nr	3 h -1.5 V	56:15:17	2:0.8:0.9	[94]
Non-bpy	ligands	•		•		•				,		'	
40	39	N-methyl-N'-2- pyridylimidazol- 2-ylidine	Br <sup>-</sup>	1 mM Mn; 0.1 M Bu <sub>4</sub> NClO <sub>4</sub> in CH <sub>3</sub> CN; pH adjusted to 3.7 (HClO <sub>4</sub> )	SCE	-1.46, -1.72 <sup>e</sup>	H <sub>2</sub> O (2.78)	1.9 (0.01)	nr	4 h -1.46 V	35:nr:0	nr	[78]
41	40	N-methyl-N'-2- pyridylbenzimid azol-2-ylidine	Br <sup>-</sup>	1 mM Mn; 0.1 M Bu <sub>4</sub> NClO <sub>4</sub> in CH <sub>3</sub> CN; pH adjusted to 3.7 (HClO <sub>4</sub> )	SCE	-1.35 (2e), -1.64 <sup>e</sup>	H <sub>2</sub> O (2.78)	2 (0.01)	0.08	nr	nr	nr	[78]
42			Br <sup>-</sup>	1 mM Mn; 0.1 M Bu <sub>4</sub> NClO <sub>4</sub> in CH <sub>3</sub> CN	$Fc^{+\!/0}$	-1.93 (2e)	H <sub>2</sub> O (2.78)	1.7 (0.10)	0.08	nr	48:nr:0	4:nr:0	[78]
43	42	N-ethyl-N'-2- pyrimidylbenzi midazol- 2-ylidene	Br <sup>-</sup>	1 mM Mn; 0.1 M Bu <sub>4</sub> NClO <sub>4</sub> in CH <sub>3</sub> CN	$Fc^{+/0}$	-1.77 (2e)	H <sub>2</sub> O (2.78)	5.2 (0.10)	nr	4 h -1.46 V	72:nr:0	>4:nr:0	[79]
44	43	IMP	Br <sup>-</sup>	2 mM; 0.2 M Bu <sub>4</sub> NPF <sub>6</sub> in CH <sub>3</sub> CN	$Fe^{+/0}$	-1.41, -1.54	H <sub>2</sub> O (2.61)	2.4 (0.10)	f	nr	nr	nr	[80]
45	44	IPIMP	Br <sup>-</sup>	2 mM; 0.2 M Bu <sub>4</sub> NPF <sub>6</sub> in CH <sub>3</sub> CN	$Fc^{+\!/0}$	-1.49	H <sub>2</sub> O (2.61)	1.8 (0.10)	f	nr	nr	nr	[80]
46	45	DIPIMP	Br <sup>-</sup>	2 mM; 0.2 M Bu <sub>4</sub> NPF <sub>6</sub> in CH <sub>3</sub> CN	$Fe^{+\!/0}$	-1.44	H <sub>2</sub> O (2.61)	2.4 (0.10)	f	nr	nr	nr	[80]
47	46	TBIMP	Br <sup>-</sup>	2 mM; 0.2 M Bu <sub>4</sub> NPF <sub>6</sub> in CH <sub>3</sub> CN	$Fe^{+/0}$	-1.45	H <sub>2</sub> O (2.61)	1.6 (0.10)	f	nr	nr	nr	[80]
48	47	TBIEP	Br <sup>-</sup>	2 mM; 0.2 M Bu <sub>4</sub> NPF <sub>6</sub> in CH <sub>3</sub> CN	$Fc^{+/0}$	-1.53 (2e)	H <sub>2</sub> O (2.61)	2.1 (0.10)	f	nr	nr	nr	[80]
49	61	PNP		1 mM Mn; 0.1 M Bu <sub>4</sub> NPF <sub>6</sub> in CH <sub>3</sub> CN	$Fc^{+/0}$	-2.01, -2.31	none	8 (0.10)	f	2 h -2.30 V	96:nr:0	3:nr:0	[135]
50							H <sub>2</sub> O (2.78)	8 (0.10)	f	1.67 h -2.50 V	33:nr:32	1.9:nr:1.8	[135]
51	62	PN	Br <sup>-</sup>	1 mM Mn; 0.1 M Bu <sub>4</sub> NPF <sub>6</sub> in CH <sub>3</sub> CN	$Fc^{+/0}$	-2.43, -2.69	H <sub>2</sub> O (2.78)	1.7 (0.10)	f	3.3 h -2.50 V	61:nr:38	1.7:nr:1	[135]
Immobili	zed catalysts	s											

52		bpy	Br <sup>-</sup>	Mn immobilized in Nafion® film at GCE (0.25% active); 30 mM phosphate buffer (pH 7)	Ag/AgCl	-1.24, -1.46	H <sub>2</sub> O (55.5, neat)	na	na	4 h -1.50 V	51:nr:24	471:nr:221	[137]
53				1 mM Mn; 0.1 M Bu <sub>4</sub> NPF <sub>6</sub> in CH <sub>3</sub> CN	SCE	-1.24, -1.46	H <sub>2</sub> O (2.78)	nr	nr	4 h <sup>g</sup> -1.50 V	52:nr:11	35.9:nr:7.6	[95]
54		dtbpy	Br <sup>-</sup>	1 mM Mn; 0.1 M Bu <sub>4</sub> NPF <sub>6</sub> in CH <sub>3</sub> CN	SCE	-1.39, -1.57	H <sub>2</sub> O (2.78)	nr	nr	4 h <sup>g</sup> -1.50 V	71:nr:23	46.1:nr:14.9	[95]
55	22	dhbpy	Br <sup>-</sup>	1 mM Mn; 0.1 M Bu <sub>4</sub> NPF <sub>6</sub> in CH <sub>3</sub> CN	SCE	-1.38, -1.73, -2.01, -2.20	none	nr	nr	4 h <sup>j</sup> -2.1 V	6:nr:45	nr	[95]
56	35	debpy	Br <sup>-</sup>	1 mM Mn; 0.1 M Bu <sub>4</sub> NPF <sub>6</sub> + 2.78 M H <sub>2</sub> O in CH <sub>3</sub> CN	SCE	-1.07, -1.41	H <sub>2</sub> O (2.78)	nr	nr	4 h -2.1 V	89:nr:0	0.6:nr:0	[95]
57							H <sub>2</sub> O (2.78)	nr	nr	4 h <sup>g</sup> -1.40 V	40:nr:1	0.3:nr:0	[95]
58	55	bpabpy	Br <sup>-</sup>	Mn adsorbed on ITO film (7μm); 0.1 M Bu <sub>4</sub> NBF <sub>4</sub> in CH <sub>3</sub> CN	$Fc^{+\!/0}$	-1.6	none	na	na	nr	nr	nr	[133]
59				Mn adsorbed (34 nmol cm <sup>-2</sup> ) on TiO <sub>2</sub> film (6μm); 0.1 M Bu <sub>4</sub> NPF <sub>6</sub> + 2.78 M H <sub>2</sub> O in CH <sub>3</sub> CN	$Fc^{+/0}$	nr	H <sub>2</sub> O (2.78)	na	na	8 h -1.7 V	67:nr:12	112:nr:20	[133]
60	30	bpy <sub>pyr</sub>	Br <sup>-</sup>	1 mM Mn; 0.1 M Bu <sub>4</sub> NPF <sub>6</sub> in CH <sub>3</sub> CN	$Fc^{+/0}$	-1.68, -1.86	H <sub>2</sub> O (2.78)	nr	nr	nr	nr	nr	[104]
61				Mn immobilized at MWCNTs; aq. 0.5 M KHCO <sub>3</sub> (1 atm Ar, pH 8.2; 1 atm CO <sub>2</sub> , pH 7.4)	SHE	-1.0 shoulder	$H_2O^{bb}$ $pH = 5.2$	na	na	8 h -1.1 V	25:8:59 high Γ low Γ	1400:460:3304 CO = 1500-2000 HCO <sub>2</sub> H = 3920	[104]
62	64	apbpy	Br⁻	1 mM Mn; 0.1 M Bu <sub>4</sub> NPF <sub>6</sub> in CH <sub>3</sub> CN	$Fc^{+/0}$	-1.52, -1.76	H <sub>2</sub> O (4.45)	16 (0.20)	f	1.5 h; -1.73 V 2 h; -1.85 V	93:nr:nr 56.5:nr:nr	12:nr:nr 10.9:nr:nr	[134]
63				1 mM Mn; 0.1 M Bu <sub>4</sub> NPF <sub>6</sub> in CH <sub>3</sub> CN	$Fc^{+/0}$		MeOH (1.98)	6 (0.20)	f	2 h -1.85 V	96:nr:nr	3.6:nr:nr	[134]
64				Mn electrochemically grafted (C-C bond) at	$Fe^{+/0}$		H <sub>2</sub> O (4.45)	na	na	1.18 h -1.75 V	75:nr:nr	359.6:nr:nr	[134]
65				GCE (area = 0.72 mm²); 0.1 M Bu <sub>4</sub> NBF <sub>4</sub> in CH <sub>3</sub> CN	Fc <sup>+/0</sup>		MeOH (1.98)	na	na	0.4 h -1.95 V	66.1:nr:nr	145.2:nr:nr	[134]

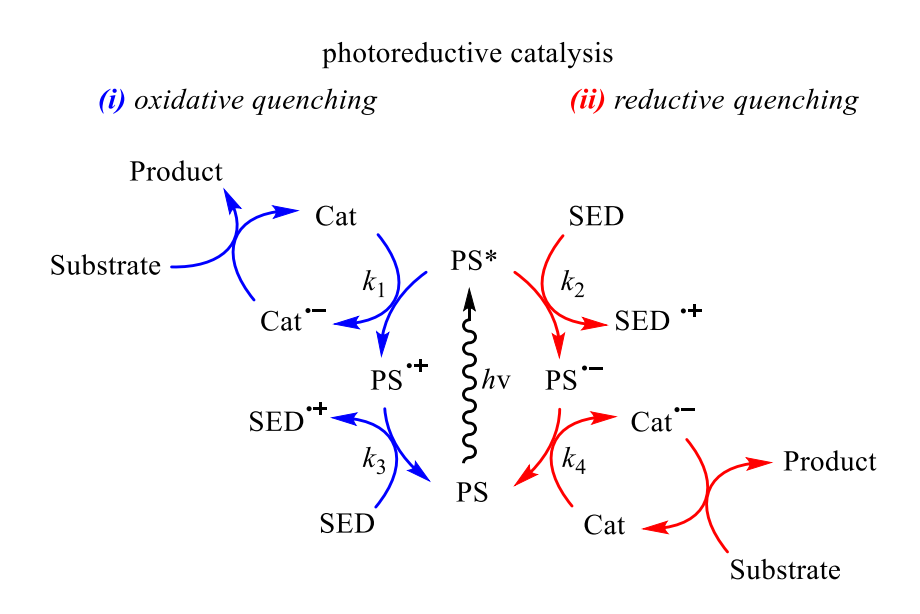
nr = not reported; na = not applicable (a) same electrolyte and Mn concentration as tabulated but with added acid as noted (b) identical to voltammetry conditions unless otherwise noted (c) recorded at  $\upsilon=0.1~V~s^{-1}$  unless noted otherwise (d) TOF<sub>max</sub> calculated from  $i_{cat}/i_p$  after confirmation of stead-state conditions using Eq. 17 (e)  $\upsilon=0.01~V~s^{-1}$  (f) steady-state (pure-kinetic) conditions not confirmed to determine TOF<sub>max</sub> (g) precatalyst immobilized in Nafion®/MWCNT film at glassy carbon electrode, pH 7, 0.1 M phosphate buffer (h) [Mn] = 0.0009 M, [PhOH] = 0.5, 0.1 M Bu<sub>4</sub>NPF<sub>6</sub> in CH<sub>3</sub>CN electrolyte (i) [Mn] = 0.005 M, [TFE] = 0.8 M (j) [Mn] = 0.002 M (k) [Mn] = 0.005 M, [TFE] = 0.3 M (l) [Mn] = 0.005 M, [Mg<sup>2+</sup>] = 0.2 M, Mg counter electrode, 1 equivalent of Mg(CO<sub>3</sub>) ppt formed (m) [Mn] = 0.005 M, [Zn(cyclam)]<sup>2+</sup> = 0.03 M (n) data for *protonation-first* and *reduction-first* pathways (o) [PhOH] = 0.5 M (p) includes CO loss from catalyst (q) [MnBr(κ<sup>3</sup>-tpy)(CO)<sub>2</sub>] (r) [Mn] = 0.00017 M, [H<sub>2</sub>O] = 5.56 M

#### 5.2 Photocatalysis

# 5.2.1 Introduction to photocatalytic CO<sub>2</sub> reduction

Following the pioneering study of electrocatalytic reduction of CO<sub>2</sub> to CO by MnBr(α-diimine)(CO)<sub>3</sub> complexes in 2011 [35], it was not until 2014 that the first complementary photocatalytic system was reported by Ishitani and co-workers [148]. While there is a rich literature on the photophysical and photochemical properties of MnBr( $\alpha$ diimine)(CO)<sub>3</sub> complexes (for example see references [124, 149-154]), unfortunately, and in contrast to their Re(I) analogues, their lowest-energy triplet states are too short lived for them to be used directly as photocatalysts. Furthermore, MnBr(α-diimine)(CO)<sub>3</sub> complexes are prone to photoinduced decomposition, including photoisomerization and ligand loss [124]. Hence, the very limited number of reports of successful photocatalytic CO<sub>2</sub> reduction utilizing MnBr(αdiimine)(CO)<sub>3</sub> precatalysts have all used a separate redox photosensitizer typically with caution to only irradiate the photosensitizer absorption bands. Unlike the recent tremendous interest and growth in Mn-based electrocatalytic systems, the scope of MnBr(α-diimine)(CO)<sub>3</sub> structures investigated for photocatalytic applications has been much more limited. More promising, however, and refreshingly ambitious considering the nascent nature of this field, has been the recent transition to a photo-electrocatalytic approach [133, 155]. However, we will start with a brief introduction to the fundamental requirements and characterization criteria for homogeneous photocatalytic systems.

As mentioned above, photocatalytic  $CO_2$  reduction systems using a MnBr( $\alpha$ -diimine)( $CO_3$ ) precatalyst require a redox photosensitizer (PS) to harness the input photon energy, typically combined with a large excess of a chemical reductant, also known as a sacrificial electron donor (SED). Scheme 9 shows the two possible pathways toward the generation of an active reduced catalyst ( $Cat^-$ ) via photosensitization.



**Scheme 9.** Generic mechanisms for the photoinitiation of reductive catalysis illustrated for *(i)* oxidative quenching and *(ii)* reductive quenching pathways, where PS = redox photosensitizer, SED = sacrificial electron donor, Cat = pre-catalyst. Electron transfer rate constants (k) are indicated where appropriate to facilitate discussion in the main text.

Briefly, reductive photocatalysis is initiated upon light absorption by PS to generate its lowest-energy thermally equilibrated excited state (PS\*). PS\* should be sufficiently long-lived to facilitate a subsequent bimolecular electron-transfer reaction via either oxidative quenching [Scheme 9(i)] or reductive quenching [Scheme 9(ii)] of PS\*. Oxidative quenching of PS\* to PS\*+

is facilitated by the pre-catalyst (denoted as Cat in Scheme 9), which is itself reduced to (or en route to) the active catalyst (denoted as Cat in Scheme 9). Thermodynamically, for this electron-transfer reaction to be exergonic, the  $E(PS^{\bullet+}/PS^{*})$  reduction potential should be more negative than the E(Cat/Cat<sup>\*-</sup>) reduction potential. However, this is quite a rare situation for CO<sub>2</sub> reduction precatalysts which generally have very negative reduction potentials (re. Scheme 10). Alternatively, reductive quenching of PS\* to PS\*- can occur via oxidation of SED to SED\*+. Similarly, from a thermodynamic perspective, for this reaction to be exergonic, the E(PS\*/PS\*-) reduction potential of the redox photosensitizer should be more positive than the  $E(SED^{\bullet+}/SED)$ reduction potential. The reductive quenching mechanism is typically also kinetically favored since the concentration of SED is generally orders of magnitude greater than the catalyst concentration, such that  $k_2 \gg k_1$ . Upon electron transfer from the PS<sup>\*-</sup> reductant to Cat, the ground-state PS is regenerated, in the process generating one-equivalent of the one-electron reduced Cat<sup>-</sup>. In the case of typical MnX(α-diimine)(CO)<sub>3</sub> pre-catalysts, Cat<sup>-</sup> corresponds to the one-electron reduced, pentacoordinate 17-valence electron species, Mn<sup>•</sup>(α-diimine)(CO)<sub>3</sub> (generated upon ejection of  $X^-$ ), which will rapidly dimerize to yield [Mn( $\alpha$ -diimine)(CO)<sub>3</sub>]<sub>2</sub>. The latter dimer absorbs strongly in the visible and will undergo Mn<sup>0</sup>-Mn<sup>0</sup> bond homolysis to generate a dynamic equilibrium with the reactive Mn<sup>•</sup>( $\alpha$ -diimine)(CO)<sub>3</sub> monomer when exposed to a continuous light source. It is generally accepted that the Mn<sup>\*</sup>(α-diimine)(CO)<sub>3</sub> monomer abstracts a H atom (possibly from the oxidized SED+) to generate a Mn-H in-situ, which ultimately produces HCO<sub>2</sub>H (vide infra). Alternatively, the ensuing catalytic mechanism can be described by Scheme 1 in the electrocatalysis discussion above. For example, catalysis may occur slowly via the  $[Mn(\alpha-diimine)(CO)_3]_2$  dimer, or if PS<sup>--</sup> is sufficiently reducing, the twoelectron reduced 18-valence electron active catalyst, [Mn(α-diimine)(CO)<sub>3</sub>] may be generated in-situ and follow either the *protonation-first* or *reduction-first* pathway, depending upon the  $\alpha$ -diimine structural influence as well as the p $K_a$  of any Brønsted acid that is present.

Although we stated that the oxidative quenching mechanism is quite rare for photocatalytic CO<sub>2</sub> reduction, there are examples [156-159]. For example, in the recent work of Wasielewski and co-workers [157, 158] naphthalenediimide (NDI) and perylenediimide (PDI) derivatives were covalently bound to Re(bpy)(CO)<sub>3</sub>-type CO<sub>2</sub> reduction catalysts. The NDI and PDI moieties are easily reduced by chemical or electrochemical means, and the resulting NDI<sup>-</sup> and PDI<sup>-</sup> radical anions absorb in the long wavelength region of the visible, producing highly reducing NDI<sup>-\*</sup> or PDI<sup>-\*\*</sup> excited states that are capable of reducing the Re-based catalyst unit. We anticipate that similar systems using Mn-based catalytic units should be viable.

# 5.2.2 Redox photosensitizers for reductive quenching

The choice of PS for reductive quenching depends on several factors, but a PS should exhibit certain desirable properties. These include: (i) strong light absorption, ideally in the visible region, that avoids competitive absorption by the catalyst and SED, (ii) a sufficiently long-lived excited state to allow reductive electron transfer quenching of PS\* to occur, (iii) a strongly oxidizing excited state (i.e., a high  $E(PS^*/PS^*-)$ ), and (iv) PS\*- should be stable, allowing for efficient electron transfer to Cat. Transition metal complexes are advantageous in this scenario, and the most commonly employed PS is  $[Ru(bpy)_3]^{2+}$  (56) and its bpy-substituted derivatives [160]. For example,  $[Ru(bpy)_3]^{2+}$  exhibits a strong metal-to-ligand charge-transfer ( ${}^1MLCT$ ) visible absorption band ( $\lambda_{max} = 452$  nm,  $\varepsilon = 1.46 \times 10^4 \text{ M}^{-1} \text{ cm}^{-1}$ ), and a long-lived and strongly oxidizing  ${}^3MLCT$  excited state ( ${}^3\tau = 855$  ns and  $E(Ru^{2+*}/Ru^{*+}) = +0.84 \text{ V vs. SCE}$ ). Thus, in the case of PS =  $[Ru(bpy)_3]^{2+}$ , PS\*- represents the strongly reducing  $[Ru(bpy)_3]^{*+}$  radical cation.

Although not yet reported for use with Mn-based systems, Ir(ppy)<sub>3</sub> (ppy = 2-phenylpyridine) is also a commonly-employed PS in homogeneous photocatalysis [161]. Other photosensitizers that have been used for Mn-based photocatalytic CO<sub>2</sub> reduction include, [Ru(dmbpy)<sub>3</sub>]<sup>2+</sup> (57), zinc tetraphenyl porphyrin (ZnTPP, 58) and fluorescein (59, Fig. 27) [162].

**Figure 27.** Molecular structures of the [Ru(bpy)<sub>3</sub>]<sup>2+</sup>, [Ru(dmbpy)<sub>3</sub>]<sup>2+</sup>, fluorescein and ZnTPP photosensitizers.

## 5.2.3 Sacrificial electron donors

While a practical artificial photosynthetic system for  $CO_2$  reduction would ideally generate reducing equivalents from the catalytic oxidation of water, similar to in natural photosystem II, such a system is too complex and impractical for fundamental mechanistic investigations and catalyst development. It is for this reason that SEDs are employed, allowing the  $CO_2$  reduction half-reaction to be studied independently [163]. Desirable properties of a SED include a  $E(SED^{*+}/SED)$  reduction potential that is sufficiently more negative than  $E(PS^*/PS^{*-})$  to allow efficient electron transfer to  $PS^*$  within the excited state lifetime, and a  $SED^{*+}$  species that rapidly decomposes upon formation. Traditionally, various types of tertiary amines have fulfilled these criteria. For example, the original photocatalytic  $CO_2$  reduction studies with  $ReX(\alpha$ -diimine)( $CO_3$ ) photocatalysts employed either triethylamine (TEA;  $E(TEA^{*+}/TEA) = +0.96$  V vs.

SCE in CH<sub>3</sub>CN [164]) or triethanolamine (TEOA;  $E(TEOA^{*+}/TEOA) = +0.80 \text{ V}$  vs. SCE in CH<sub>3</sub>CN [164]). as a SED. TEA\*+ and TEOA\*+ both rapidly react with their neutral counterparts, as shown in Eq. (22) for TEOA. The resulting neutral radicals are also strong reductants. For example, the  $E(Et_2N^+=CHCH_3/Et_2NC^*HCH_3)$  reduction potential is known to be -1.12 V vs. SCE in CH<sub>3</sub>CN, and while that of (HOCH<sub>2</sub>CH<sub>2</sub>)<sub>2</sub>N<sup>+</sup>=CHCH<sub>2</sub>OH is unknown, it should be even more negative than -1.12 V [165]. Thus, these radicals will be able to provide a further reducing equivalent for the CO<sub>2</sub> reduction reaction, as shown in Eq. (23) for TEOA.

$$TEOA^{\bullet+} + TEOA \rightarrow TEOAH^{+} + (HOCH_2CH_2)_2NC^{\bullet}HCH_2OH$$
 (22)

$$(HOCH2CH2)2NC'HCH2OH \rightarrow (HOCH2CH2)2N'=CHCH2OH + e- (23)$$

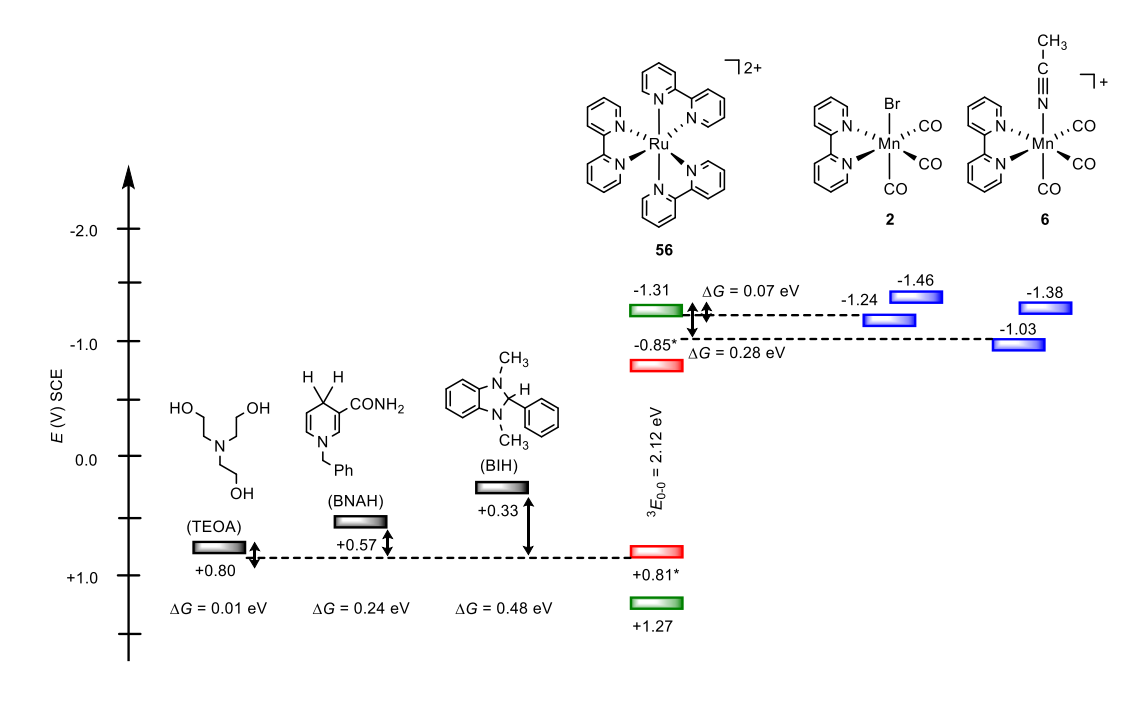
When a PS such as  $[Ru(bpy)_3]^{2+}$  is used, TEOA is a poor choice of SED since the reductive quenching of PS\* is very inefficient due to  $E(TEOA^{++}/TEOA)$  being only slightly more negative than  $E(Ru^{2+*}/Ru^{++}) = +0.84$  V vs. SCE. In these cases, a more strongly reducing SED is preferred. Two such SEDs that have commonly been employed in DMF and CH<sub>3</sub>CN are 1-benzyl-1,4-dihydronicotinamide (BNAH) and 1,3-dimethyl-2-phenyl-2,3-dihydro-1H-benzo[d]imidazole (BIH). BIH is an even stronger reductant than BNAH ( $E(BIH^{++}/BIH) = 0.33$  V, while  $E(BNAH^{++}/BNAH) = 0.57$  V vs. SCE) [164]. When BNAH or BIH are used, it is necessary to add a base to the solution (TEOA is typically used), which promotes rapid deprotonation of the oxidized BNAH\* or BIH\* and prevents back electron transfer. In the case of BNAH, the resulting BNA\* radicals dimerize into two isomers of (BNA)<sub>2</sub> (Eq. (24)). While (BNA)<sub>2</sub> is a strong reductant itself, it is ineffective for CO<sub>2</sub> reduction since the (BNA)<sub>2</sub>\*+ radical cation is too stable, resulting in rapid back electron transfer, which ultimately wastes absorbed

photons. However, in the case of BIH, after deprotonation of BIH<sup>\*+</sup>, the strongly reducing BI<sup>\*</sup> radical does not dimerize and has been shown to donate a second electron into the system (even to the ground state of the PS) (Eq. (25)) [166]. This results in a much more efficient use of photons and a higher rate of catalysis. Indeed, the highest reported TONs and TOFs for Ru–Re supramolecular CO<sub>2</sub> reduction photocatalysts have been achieved with BIH as a SED [166].

$$CH_3$$
 $CH_3$ 
 $CH_3$ 

An alternative SED to BNAH and BIH that uses simple, commercially available materials was recently developed by Shan and Schmehl [167], although it has not yet been applied to photocatalytic CO<sub>2</sub> reduction. This system makes use of the more easily oxidized tritolylamine (TTA) to reduce PS\* (where PS = **56** and various derivatives) in the presence of a large excess of TEA that acts as a SED, irreversibly reducing the TTA\*+ cation. Despite the fact that the reduction of TTA\*+ by TEA is thermodynamically unfavorable, in the presence of a sufficient concentration of TEA (0.55 M was used) it becomes kinetically competitive with back electron transfer from PS- to TTA\*+. It is also worth mentioning that a couple of other SEDs have been used for photocatalytic CO<sub>2</sub> reduction in aqueous solution, although only ascorbic acid/ascorbate

(asc<sup>-</sup>) has been tried, albeit unsuccessfuly, with a Mn-based catalysts [103]. Ascorbic acid is the most commonly employed SED for use in aqueous solution. Although it works, it is not truly sacrificial, since the oxidized form of asc<sup>-</sup> is stable enough that it can accept the electron back from PS<sup>-</sup>, thus reducing the efficiency of CO<sub>2</sub> reduction [168]. To address this issue, Ishitani and co-workers recently developed a derivative of BIH, i.e., 2-(1,3-dimethyl-2,3-dihydro-1*H*-benzimidazol-2-yl)benzoic acid (BI(CO<sub>2</sub>H)H), which must be used in the presence of NaOH to generate the carboxylate ion (BI(CO<sub>2</sub><sup>-</sup>)H), which is water soluble [169]. Use of this SED resulted in a significant improvement in excited state quenching efficiency and catalytic performance. An energy level diagram illustrating the electron-transfer free energies ( $\Delta$ G) for the TEOA, BNAH and BIH SED's to the photoexcited state,  $56^*$  {[Ru<sup>III</sup>(bpy)<sub>2</sub>(bpy•<sup>-</sup>)]<sup>2+</sup>}\*, in CH<sub>3</sub>CN (SED $\rightarrow$ PS<sup>\*</sup> reductive quenching), as well as electron-transfer free energies ( $\Delta$ G) from the one-electron reduced  $56^-$  [Ru<sup>II</sup>(bpy)<sub>2</sub>(bpy•<sup>-</sup>)]<sup>+</sup> to the established precatalysts 2 and 6 (PS<sup>-</sup> $\rightarrow$ precatalyst), is illustrated in Scheme 10.



Scheme 10. Energy level alignment diagram illustrating the relevant reduction potentials (in CH<sub>3</sub>CN vs SCE) for the TEOA, BNAH and BIH sacrificial electron donors (SEDs), the ground and excited state (\*) reduction potentials for the [Ru(bpy)<sub>3</sub>]<sup>2+</sup> photosensitizer (PS), and the ground state reduction potentials of the MnBr(bpy)(CO)<sub>3</sub> and [Mn(bpy)(CO)<sub>3</sub>(CH<sub>3</sub>CN)]<sup>+</sup> precatalysts. Free energy differences are included for the SED→PS\* reductive quenching electron-transfer reaction as well as the PS<sup>-</sup>→precatalyst electron-transfer reaction.

# 5.2.4 Measurement of photocatalytic performance

The efficiency with which a SED reductively quenches  $PS^*$  will directly impact the photocatalytic ability of a PS-Cat system. Thus, the quenching rate constant ( $k_q$ ) and the quenching fraction ( $\eta_q$ ) of a  $PS^*$  are important properties to measure. This is usually achieved through some combination of emission quenching (steady-state and/or time-resolved) and transient absorption spectroscopy, making use of Stern-Volmer plots [29]. The catalytic performance of a photocatalytic  $CO_2$  reduction system is typically evaluated by a few different

criteria, some of which overlap with catalytic figures of merit used in electrocatalysis. For example, the product selectivity can be defined in different ways, but it generally refers to the ratio of the concentration of desired CO<sub>2</sub> reduction products to the concentration of undesired products, such as H<sub>2</sub> [15]. The quantum yield (φ), is a measure of the molar ratio of the amount of CO<sub>2</sub> reduction product formed and the number of incident photons absorbed. Finally, the turnover number (TON) represents the number of times a catalytic cycle can repeat (or turnover) during the lifetime of the catalyst, and is calculated by dividing the concentration of CO<sub>2</sub> reduction products by the concentration of the catalyst used. The related quantity of turnover frequency (TOF) is obtained by dividing the TON by the reaction time, and is a measure of the rate of catalysis [15, 136, 170].

A major contrast between electrocatalytic and photocatalytic CO<sub>2</sub> reduction systems that should be appreciated is that electrocatalytic systems have an infinite supply of reducing electrons with a tunable driving force, whereas photocatalytic systems are limited by the quantity of SED to maintain catalytic turnover of the PS cycle via the PS\*/PS\*- redox reaction. In addition to the single-electron capacity and stoichiometric limit of available SED, the potential driving force for Cat reduction is also limited by the intrinsic properties of the chosen PS. All things considered, there are many constraints on the design of a photocatalytic CO<sub>2</sub> reduction system. However, with careful consideration of the relevant thermodynamics, successful turnover of PS, Cat and product can be achieved.

## 5.2.5 Published reports of photocatalytic CO<sub>2</sub> reduction using Mn-based catalysts

The first report of photocatalytic CO<sub>2</sub> reduction with a Mn-based catalyst, by Ishitani and coworkers [18], used a 1:1 homogenous mixture of the MnBr(bpy)(CO)<sub>3</sub> (2) precatalyst and

[Ru(dmbpv)<sub>3</sub>]<sup>2+</sup> (57) redox photosensitizer (0.05 mM), with an excess of BNAH as a SED (0.1 M) in a DMF-TEOA solvent system (DMF:TEOA, 3:1, v/v). Under 1 atm of CO<sub>2</sub> and using 480 nm LED irradiation (4.3 x 10<sup>-8</sup> einsteins) for a 12 h duration, a high selectivity for HCO<sub>2</sub>H was observed (Table 4 entry 2,  $TON_{HCO2H} = 149$ ,  $\phi = 0.053$ ) with trace amounts of CO ( $TON_{CO} = 12$ ) and  $H_2$  (TON<sub>H2</sub> = 14). Replacing [Ru(dmbpy)<sub>3</sub>]<sup>2+</sup> with [Ru(bpy)<sub>3</sub>]<sup>2+</sup> improved catalyst efficiency slightly (Table 4 entry 1, TON<sub>HCO2H</sub> = 157). Remarkably, the reaction showed a strong solvent dependency, with a CH<sub>3</sub>CN:TEOA (3:1, v/v) solvent mixture reducing TON<sub>HCO2H</sub> to 78 (Table 4 entry 4) while increasing TON<sub>CO</sub> to 40. A solvent mixture containing N,N'-dimethylacetamide (DMA:TEOA, 3:1, v/v) also showed a reasonable performance relative to DMF (Table 4 entry 3, TON<sub>HCO2H</sub> = 98). Using UV/vis and IR spectroscopy, the reaction mechanism was demonstrated to follow sacrificial reduction of the [Ru(dmbpy)<sub>3</sub>]<sup>2+3</sup>MLCT excited-state by BNAH to ultimately generate the [Mn(bpy)(CO)<sub>3</sub>]<sub>2</sub> dimer. Initial predominant CO evolution subsided concomitant with the disappearance of the [Mn(bpy)(CO)<sub>3</sub>]<sub>2</sub> dimer within the first 30 mins, at which point steady-state formation of formic acid was observed. Photolysis of a previously isolated sample of [Mn(bpy)(CO)<sub>3</sub>]<sub>2</sub> dimer in DMF-TEOA (4:1 v/v) under argon resulted in the same UV/vis spectral changes that were observed during catalysis, indicating possible homolytic cleavage of the Mn-Mn bond. However, unfortunately the active catalyst could not be identified, with insight being limited to the confirmation of a paramagnetic Mn species via peak broadening in <sup>1</sup>H-NMR analysis after photocatalysis, and the lack of any new  $\nu(CO)$  IR bands being formed after decomposition of the dimer. Intriguingly, the observation of paramagnetism is consistent with the EPR observation of the paramagnetic [Mn<sup>II</sup>(dmbpy)(CO)<sub>3</sub>(CO<sub>2</sub>H)]<sup>+</sup> species following exposure of the [Mn(dmbpy)(CO)<sub>3</sub>]<sub>2</sub> dimer to CO<sub>2</sub> and H<sub>2</sub>O by Orio, Chardon-Noblat and coworkers [106] (see Section 4.2). However, it is probably unlikely that this was the species

formed in Ishitani and co-workers' experiments. While dynamic light scattering indicated no formation of colloidal nanoparticles, the apparatus used could only detect particles larger than 100 nm, so the formation of catalytically-active nanoparticles of <100 nm diameter cannot be ruled out. The mechanism of photocatalytic CO<sub>2</sub> reduction proposed by Ishitani and co-workers is shown in Fig. 28.

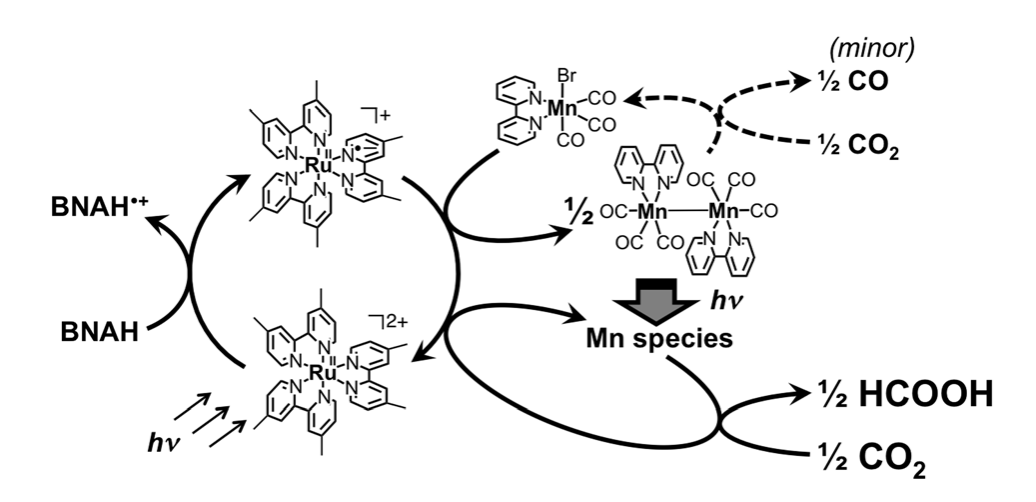


**Figure 28:** Proposed mechanism for the photocatalytic reduction of CO<sub>2</sub> to HCO<sub>2</sub>H and CO upon 480 nm photolysis of a 1:1 mixture of **2** and **57** in CO<sub>2</sub>-saturated DMF–TEOA (3:1 v/v) in the presence of BNAH. Reproduced with permission from ref. [18]. Copyright 2014 Royal Society of Chemistry.

In the previous section, we discussed the unique ability of **23** to electrochemically generate the two-electron reduced [Mn(bpy)(CO)<sub>3</sub>]<sup>-</sup> active catalyst by disproportionation of the one-electron reduced [Mn(CN)(bpy)(CO)<sub>3</sub>]<sup>-</sup> intermediate for highly selective CO formation in the presence of PhOH as a Brønsted acid [96]. In a later study, Kubiak and co-workers cleverly took advantage of this reactivity to complement the single-photon/single-electron restriction of a photocatalysis strategy [98]. Under optimum conditions with 0.1 mM **23**, 1.0 mM **57** as the PS,

excess 0.1 M BNAH as a SED, and a DMF:TEOA (4:1 v/v) solvent mixture, under 1 atm of CO<sub>2</sub> and after 15 h of 470 nm LED irradiation, selective HCO<sub>2</sub>H production was observed (Table 4 entry 8,  $TON_{HCO2H} = 130$ ,  $\phi = 0.026$ ), with significantly less CO ( $TON_{CO} = 7.1$ ,  $\phi = 0.0018$ ) and  $H_2$  (TON<sub>H2</sub> = 1.6). Similar to the earlier work of Ishitani and co-workers [18], changing to a CH<sub>3</sub>CN:TEOA (4:1 v/v) solvent mixture under otherwise identical conditions, Kubiak and coworkers altered the product selectivity to favor CO formation (Table 4 entry 9,  $TON_{CO} = 21$ ,  $\phi =$ 0.0053) over HCO<sub>2</sub>H (TON<sub>HCO2H</sub> = 9,  $\phi = 0.0022$ ) and H<sub>2</sub> (TON<sub>H2</sub> = 1.3), although the decrease in TON<sub>HCO2H</sub> was much more significant in this case. As discussed above in Section 4, cyclic voltammetry and IR-SEC studies suggested that the CH<sub>3</sub>CN/TEOA solvent mixture favors rapid formation of the two-electron reduced [Mn(bpy)(CO)<sub>3</sub>]<sup>-</sup> active catalyst, reacting with CO<sub>2</sub> and a proton source to form the Mn<sup>I</sup>-CO<sub>2</sub>H intermediate and ultimately evolve CO (Scheme 4). However, in the DMF/TEOA solvent mixture, the higher stability (slower disproportionation) of the one-electron reduced species [Mn(CN)(bpy)(CO)<sub>3</sub>]<sup>-</sup> is proposed to allow adequate time for H-atom abstraction from TEOA or perhaps BNAH<sup>•+</sup>, to generate the Mn(H)(bpy)(CO)<sub>3</sub> metalhydride species which in turn could generate HCO<sub>2</sub>H via CO<sub>2</sub> insertion into the M–H bond.

An important observation in the latter study during control experiments was the generation of HCO<sub>2</sub>H in the dark with a DMF–TEOA solvent mixture [98]. We note an earlier report by Vos and co-workers [171], who discussed the formation of HCO<sub>2</sub>H from the hydrolysis of DMF in the presence of H<sub>2</sub>O and bases such as TEA and TEOA. Vos and co-workers urged caution with respect to the water content of the solution, and suggested to avoid an aqueous work-up procedure or analytical method such as ion-chromatography, when attempting to quantify HCO<sub>2</sub>H production after using DMF solvent for photocatalysis in the presence of a base (e.g.,

TEOA or TEA). While Kubiak did not use water or water-based analytical methods [98], and it is therefore unlikely that the HCO<sub>2</sub>H he observed in the dark actually came from DMF hydrolysis, it is worth emphasizing here consideration of the alternative DMA solvent for photocatalytic CO<sub>2</sub> reduction, which does not suffer from this hydrolysis issue with respect to HCO<sub>2</sub>H quantification.

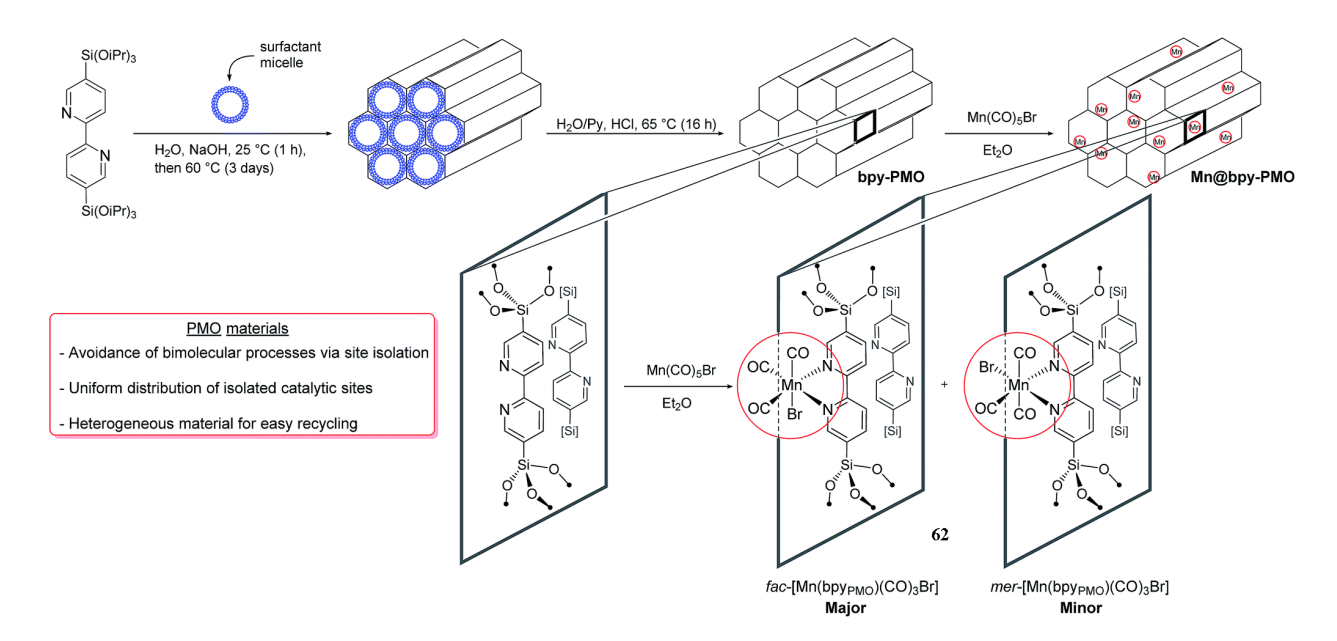
In addition to the electrocatalytic CO<sub>2</sub> reduction studies reported by Compain, Chardon-Noblat and co-workers for the phen-dione catalysts 36 and 37 (Section 5.1.1), photocatalytic studies were also conducted using both 2 and 38 for reference [103]. The following photocatalytic conditions were optimized for both 36 and 37: 0.1 mM Mn, 0.1 M 56 as the PS, 0.1 M BNAH as a SED, 1 atm of CO<sub>2</sub>:CH<sub>4</sub> (95:5) and 16 - 24 h of 480 nm irradiation (Hg-Xe lamp with a monochromatic filter). In contrast to other  $MnX(\alpha$ -diimine)(CO)<sub>3</sub> complexes, which appear to favor HCO<sub>2</sub>H formation in DMF/TEOA and CO formation in CH<sub>3</sub>CN/TEOA solvent systems, selective HCO<sub>2</sub>H production was observed in CH<sub>3</sub>CN/TEOA for both **36** (TON<sub>HCO2H</sub> = 52;  $TON_{CO} = 8$ ) and 37 ( $TON_{HCO2H} = 58$ ;  $TON_{CO} = 15$ ), with no formation of H<sub>2</sub> (Table 4, entries 12 & 14). Under similar conditions, consistent with literature reports of traditional MnX(αdiimine)(CO)<sub>3</sub> complexes, the reference precatalyst 2 exhibited favorable CO formation in CH<sub>3</sub>CN/TEOA (Table 4, entry 7). Upon switching the solvent mixture to DMF/TEOA, selectivity was levelled for 36 (Table 4, entries 13,  $TON_{HCO2H} = 22$ ;  $TON_{CO} = 21$ ) with the reference 2 and 38 precatalysts exhibiting selectivity for HCO<sub>2</sub>H (TON = 39) and CO (TON = 17), respectively (Table 4, entries 6 & 10). Notably, no photocatalysis was observed for 37 in the presence of added 2.78 M H<sub>2</sub>O, or when attempted in neat H<sub>2</sub>O solvent with an ascorbic acid SED based buffer.

**38** was also reported by Wang, Bian and co-workers but using a zinc tetraphenylporphyrin (ZnTPP) photosensitizer [172]. Employing optimum conditions of 2 mM **38**, 0.5 mM ZnTPP as PS, 0.10 M TEA as SED, an aqueous CH<sub>3</sub>CN/H<sub>2</sub>O (20:1 v/v) solvent mixture, and 3 h irradiation with a 500 W Xe-arc lamp (no filter indicated), selective CO formation was observed (Table 4, entry 11, TON<sub>CO</sub> = 119, TON<sub>HCO2H</sub> = 19).

The first example of an immobilized photocatalytic Mn-based system for CO<sub>2</sub> reduction was reported in 2015 by Kubiak and Cohen, where the 5,5'-dicarboxylate-2,2'-bipyridine (bpydc) ligand was incorporated into the backbone of a Zr<sub>6</sub>O<sub>4</sub>(OH)<sub>4</sub>(bpdc)<sub>6</sub> metal-organic framework (MOF; 0UiO-67-bpydc) [173]. Post-synthetic complexation of UiO-67-bpydc with MnBr(CO)<sub>5</sub> was achieved at ~76% of the bpydc coordination sites. The resulting UiO-67-MnBr(bpydc)(CO)<sub>3</sub> MOF (Fig. 29, 60) exhibited photocatalytic reduction of CO<sub>2</sub> to formate (HCOO<sup>-</sup>) (TON<sub>HCOO</sub>-= 110,  $\phi = 0.138$ ) with 96% selectivity following 18 h of 470 nm irradiation (2.51 x 10<sup>-7</sup> einstein s<sup>-1</sup> 1) in DMF/TEOA (4:1 v/v) with 57 present as a PS and BNAH as a SED (Table 4, entry 15). The rigidity of the three-dimensional UiO-67-bpydc structure prevented formation of the Mn<sup>0</sup>-Mn<sup>0</sup> dimer upon one-electron reduction, favoring HCOO<sup>-</sup> formation via CO<sub>2</sub> insertion into an assumed Mn–H intermediate, and also protected the MnBr(α-diimine)(CO)<sub>3</sub> catalytic center from degradation. This stability allowed the photocatalytic MOF 60 to be recycled three more times, culminating in a total TON<sub>HCOO</sub> of 170. Overall, the photocatalytic activity of 60 exceeded that of the homogeneous MnBr(bpydc)(CO)<sub>3</sub> precatalyst **61** (TON<sub>HCOO</sub><sub>-</sub> = 57) as well as related UiO-67 MOFs including the Re(I) analogue.

**Figure 29.** Molecular structure of the UiO-67-MnBr(bpydc)(CO)<sub>3</sub> metal-organic framework (MOF) precatalyst **60** and the MnBr(bpydc)(CO)<sub>3</sub> monomeric precatalyst **61** investigated by Kubiak, Cohen and co-workers [173].

Recently, Mougel, Fontecave and co-workers immobilized the same MnBr(CO)<sub>3</sub> moiety at the bpy coordination centers of a periodic mesoporous organosilica (PMO) material [162]. A series of highly ordered MnBr(bpy<sub>PMO</sub>)(CO)<sub>3</sub> porous solids (62) were prepared by the hydrolysis and condensation of 5,5'-bis(triisopropoxysilyl)-2,2'-bipyridine in the presence of a trimethylstearylammonium surfactant, followed by reaction with MnBr(CO)<sub>5</sub> (Scheme 11). By analyzing the bpy content in the pre-modified bpy-PMO, as well as varying the concentration of MnBr(CO)<sub>5</sub>, three MnBr(bpy<sub>PMO</sub>)(CO)<sub>3</sub> precatalyst materials were prepared with Mn:bpy ratios of 1/2, 1/10 and 1/50. Surprisingly, FTIR and diffuse reflectance UV-Vis confirmed the presence of the *mer*-isomer, although the more stable *fac*-isomer was the primary product.



**Scheme 11:** Synthetic pathway to the MnBr(bpy<sub>PMO</sub>)(CO)<sub>3</sub> solid-state periodic mesoporous organosilica (PMO) precatalyst prepared using the 5,5'-bis(triisopropoxysilyl)-2,2'-bipyridine ligand by Mougel, Fontecave and co-workers. Reproduced with permission from ref. [162]. Copyright 2017 Royal Society of Chemistry.

Initial photolysis studies of MnBr(bpy<sub>PMO</sub>)(CO)<sub>3</sub> conducted under vacuum with a Mn:bpy ratio of 1/10 (300 W Xe arc lamp, > 400 nm band pass filter) demonstrated the grow-in of the *mer* isomer. Prolonged irradiation (up to 24 h) resulted in bromine loss and bpy reduction to form Mn<sup>+</sup>(bpy<sub>PMO</sub><sup>-</sup>)(CO)<sub>3</sub>, followed by gradual loss of all CO signals in the FTIR spectrum via monocarbonyl and dicarbonyl intermediate materials. When repeated under 1 atm of CO, the neutral tetracarbonyl Mn<sup>+</sup>(bpy<sub>PMO</sub><sup>-</sup>)(CO)<sub>4</sub> material was formed. Under optimized photocatalytic conditions (Table 4, entry 16) of 0.01 mM of the MnBr(bpy<sub>PMO</sub>)(CO)<sub>3</sub> precatalyst (Mn:bpy ratio of 1:50), 0.1 mM of **56** as the PS, 0.1 M of BIH as a SED, in a CH<sub>3</sub>CN/TEOA (5:1 v/v) solvent mixture, following 16 h of  $\lambda$  > 400 nm irradiation (300 W Xe arc lamp), the major product observed was HCOO<sup>-</sup> (TON<sub>HCOO</sub>- = 292), followed by CO (TON<sub>CO</sub> = 168) and H<sub>2</sub> (TON<sub>H2</sub> =

72). Surprisingly, no catalytic activity was observed with the more commonly used BNAH SED. Furthermore, using a DMF/TEOA (5:1 v/v) solvent mixture led to a comparable product selectivity but with over an order of magnitude drop in TONs (Table 4, entry 19). Changing the PS from 60 to the organic ZnTPP (58) or fluorescein (59) dyes also resulted in a significant drop in overall TONs but a higher selectivity for HCOO<sup>-</sup> and no H<sub>2</sub> production (Table 4, entries 17 & 18). The absence of H<sub>2</sub> with these PSs suggests that **56** is likely responsible for the H<sub>2</sub> observed when it is used as a PS. Initial TOFs for HCOO<sup>-</sup> and CO were reported as 38 min<sup>-1</sup> and 30 min<sup>-1</sup>, respectively, with a drop in all TOFs after 2 h, attributed to degradation of the 56 PS. Upon recycling the MnBr(bpy<sub>PMO</sub>)(CO)<sub>3</sub> precatalyst (Mn:bpy ratio of 1:50) for three additional runs, the catalytic activity gradually dropped off, with total conversions of  $TON_{HCOO-} = 484$  and TON<sub>CO</sub> = 239. From a mechanistic perspective, the authors proposed that the structural constraints of the MnBr(bpy<sub>PMO</sub>)(CO)<sub>3</sub> material stabilized the one-electron reduced Mn<sup>+</sup>(bpy<sub>PMO</sub><sup>•-</sup>)(CO)<sub>3</sub> radical intermediate, preventing dimerization or disproportionation (as observed for homogeneous Mn(bpy')(CO)<sub>3</sub>L systems). Thus, BIH is required as a SED rather than BNAH since the BI' species produced after one-electron oxidation/deprotonation of BIH is much more reducing compared to BNA\* (see Section 5.2.3). This facilitates the generation of the two-electron reduced [Mn(bpy<sub>PMO</sub>)(CO)<sub>3</sub>]<sup>-</sup> active catalyst for CO formation (Scheme 12). The other pathway for HCOO<sup>-</sup> production is thought to occur via H-atom abstraction from BIH\*+ by Mn<sup>+</sup>(bpy<sub>PMO</sub><sup>\*-</sup>)(CO)<sub>3</sub>, producing a Mn–H intermediate that inserts CO<sub>2</sub> to generate HCOO<sup>-</sup> (or HCO<sub>2</sub>H upon reaction with H<sup>+</sup>).

**Scheme 12:** Proposed mechanisms for the formation of HCO<sub>2</sub>H and CO from the photocatalytic reduction of CO<sub>2</sub> by MnBr(bpy<sub>PMO</sub>)(CO)<sub>3</sub> in CH<sub>3</sub>CN–TEOA in the presence of **56** as a PS and BIH as a SED. Reproduced with permission from ref. [162]. Copyright 2017 Royal Society of Chemistry.

In the first example of photoelectrochemical CO<sub>2</sub> reduction using Mn-based molecular catalysts, Chardon-Noblat, Fabre and co-workers replaced the PS and SED components of traditional homogeneous photocatalysis with hydrogen-terminated flat (Si-H) and nanowire (SiNWs-H) silicon photocathodes [174]. In combination with the three homogeneous precatalysts **2**, **5** (Fig. 1) and [Mn(dmbpy)(CO)<sub>3</sub>(C<sub>3</sub>CN)]<sup>+</sup> (Fig. 30, **63**), selective CO production was

observed upon  $\lambda > 600$  nm steady-state irradiation (20 mW cm<sup>-2</sup>) of both the Si-H and SiNWs-H photocathodes in CO<sub>2</sub>-saturated CH<sub>3</sub>CN containing Bu<sub>4</sub>NClO<sub>4</sub> electrolyte and 5% v/v (2.78 M) H<sub>2</sub>O. Initial voltammetry studies of all three Mn precatalysts investigated under 1 atm Ar exhibited similar behavior at the flat Si-H and nanostructured SiNWs-H electrodes in comparison to a glassy carbon disc, although with a 0.3 V anodic shift of all reduction events. Photocatalytic current density was exhibited by all complexes at both electrodes under 1 atm of CO<sub>2</sub> with 2.78 M H<sub>2</sub>O as a Brønsted acid. For example, photocurrent densities of 0.7 and 1.14 mA cm<sup>-2</sup> were recorded for 5 at -1.0 V vs SCE ( $\upsilon = 0.10 \text{ V}$  s<sup>-1</sup>) at flat Si-H and SiNWs-H, respectively, under catalytic conditions, representing 1.46-fold and 1.52-fold increases relative to the observed photocurrent under 1 atm Ar in the absence of H<sub>2</sub>O. The higher photocurrent density of the SiNWs-H electrode was attributed not only to its greater electrochemically active surface area but also to its greater capacity to decouple minority carrier generation and collection. Control experiments conducted with a glassy carbon disc electrode in the absence of a light source exhibited zero current density under otherwise equivalent electrocatalytic conditions, confirming an essential contribution from the minority charge carriers at the interface of the Si-H and SiNWs-H photocathodes. Of the three precatalysts studied, photocurrent density-voltage (J-V) and power-voltage (P-V) plots recorded under photocatalytic conditions confirmed 5 to exhibit the greatest fill factor (FF = 0.35) and power conversion efficiency ( $\eta$  = 3.0) at SiNWs-H photocathodes. In addition, by modifying the bpy ligand with an electropolymerizable pyrrole substituent in  $[Mn(bpypyr)(CO)_3(CH_3CN)]^+$  (Fig. 30, 64) where bpypyr = 4-[(1H-pyrrol-1yl)butyl]-4'-methyl-2,2'-bipyridine, the authors succeeded in immobilizing 64 at a modified SiNWs-H photocathode and preliminary photoelectrochemical investigations exhibited

photocatalytic current density in the presence of CO<sub>2</sub> and H<sub>2</sub>O, consistent with the homogeneous catalyst studies at SiNWs-H.

**Figure 30.** Molecular structures of precatalysts **63** and **64**, in addition to **2** and **5** (Fig. 1) investigated by Chardon-Noblat, Fabre and co-workers [174].

Finally, in addition to the electrocatalytic studies conducted by Reisner and co-workers on a mesoporoous FTO/TiO<sub>2</sub>/55 modified thin film electrode (discussed in Section 5.1.5) [133], the same system was also driven photoelectrochemically. This was achieved using a CdS quantum-dot-sensitized ZnO nanosheet photoanode, whereby the catalytic Mn-based cathode was kept in the dark in a two-compartment cell with an applied bias of  $\pm$ 0.6 V while the photoanode was irradiated at  $\lambda > 420$  nm (AM 1.5G filter, 100 mW cm<sup>-2</sup>). TEOA was required as a SED to scavenge the holes generated at the ZnO/CdS photoanode. However, its presence was ultimately deemed responsible for a poor catalytic performance (Table 4 entry 20, TON<sub>CO</sub> = 11, FE<sub>CO</sub>= 26%). Nonetheless, this study, along with the work of Chardon-Noblat, Fabre and co-workers [174], holds great promise for the photoelectrochemical catalytic reduction of CO<sub>2</sub> utilizing solar energy as a means of overcoming demanding electrochemical overpotentials.

**Table 4:** A summary of photocatalytic data for reported  $MnX(\alpha\text{-diimine})(CO)_3$   $CO_2$  reduction catalysts.

Table Entry	Catalyst Number	MnX(L <sub>2</sub> )(CO) <sub>3</sub>		[Mn]	PS	SED	Solvent	λ	Duration	TON	Reference
		$L_2$	X	(mM)	(conc)	(conc.)	(v/v)	(light source)	(h)	(CO:HCO <sub>2</sub> H:H <sub>2</sub> )	Reference
1	2	bpy	Br <sup>-</sup>	0.05	<b>56</b> <sup>i</sup> (0.05 mM)	BNAH (0.1 M)	DMF:TEOA (3:1)	480 nm LED	12	12 : 157 :8	[148]
2				0.05	57 (0.05 mM)	BNAH (0.1 M)	DMF:TEOA (3:1)	480 nm LED	12	12 : 149 : 14	[148]
3				0.05	57 (0.05 mM)	BNAH (0.1 M)	DMA:TEOA (3:1)	480 nm LED	12	9:98:14	[148]
4				0.05	57 (0.05 mM)	BNAH (0.1 M)	CH <sub>3</sub> CN:TEOA (3:1)	480 nm LED	12	40 : 78 : 17	[148]
5				0.5	57 (0.5 mM)	BNAH (0.1 M)	DMF:TEOA (4:1)	470 nm LED	18	5.1 : 70 : 0.14	[173]
6		а		0.1	57 (0.1 M)	BNAH (0.1 M)	DMF:TEOA (4:1)	> 480 nm Hg-Xe lamp	16	6:39:0	[103]
7		a		0.1	57 (0.1 M)	BNAH (0.1 M)	CH <sub>3</sub> CN:TEOA (4:1)	> 480 nm Hg-Xe lamp	16	47:15:0	[103]
8	23	bpy	(CN) <sup>-</sup>	0.1	57 (1 mM)	BNAH (0.1 M)	DMF:TEOA (4:1)	470 nm LED	15	130 : 7.1 : 1.6	[98]
9				0.1	57 (1 mM)	BNAH (0.1 M)	CH <sub>3</sub> CN:TEOA (4:1)	470 nm LED	15	21 :9 : 1.3	[98]
10	38	phen a	Br-	0.1	<b>56</b> <sup><i>j</i></sup> (0.1 M)	BNAH (0.1 M)	DMF:TEOA (4:1)	> 480 nm Hg-Xe lamp	16	17:4:0	[103]
11		phen	Br <sup>-</sup>	2	<b>58</b> (0.5 mM)	TEA (0.1 M)	CH <sub>3</sub> CN:H <sub>2</sub> O (20:1)	Xe lamp	3	119:19:0	[172]
12	36	phen-dione <sup>a</sup>	Br-	0.1	<b>56</b> <sup><i>j</i></sup> (0.1 M)	BNAH (0.1 M)	CH <sub>3</sub> CN:TEOA (4:1)	> 480 nm Hg-Xe lamp	16	8:52:0	[103]
13		a		0.1	<b>56</b> <sup><i>j</i></sup> (0.1 M)	BNAH (0.1 M)	DMF:TEOA (4:1)	> 480 nm Hg-Xe lamp	16	21 : 22 : 0	[103]
14	37	phen-dione <sup>a</sup>	CH <sub>3</sub> CN(PF <sub>6</sub> <sup>-</sup> )	0.1	<b>56</b> <sup>i</sup> (0.1 M)	BNAH (0.1 M)	CH <sub>3</sub> CN:TEOA (4:1)	> 480 nm Hg-Xe lamp	24	15:58:0	[103]
immobili	ized catalysts										
15	61	UiO-67-bpydc <sup>b</sup>	Br	0.5	57 (0.5 mM)	BNAH (0.2 M)	DMF:TEOA (4:1)	470 nm LED	18	4.5:110:1.0	[173]
16	62	bpy <sub>PMO</sub> <sup>c</sup>	Br	0.01	<b>56</b> <sup>j</sup> (0.1 mM)	BIH (0.1 M)	CH <sub>3</sub> CN:TEOA (5:1)	> 400 nm Xe lamp	16	168 : 292 : 72	[162]
17				0.01	<b>58</b> (0.1 mM)	BIH (0.1 M)	CH <sub>3</sub> CN:TEOA (5:1)	> 400 nm Xe lamp	5	17 : 52 : 0	[162]

18				0.01	<b>59</b> (0.1 mM)	BIH (0.1 M)	CH <sub>3</sub> CN:TEOA (5:1)	> 400 nm Xe lamp	5	11 : 65 : 0	[162]
19				0.1	<b>56</b> <sup><i>j</i></sup> (1 mM)	BIH (0.1 M)	DMF:TEOA (5:1)	> 400 nm Xe lamp	16	9:18:1	[162]
photo-electrochemical catalysis											
20	55	TiO <sub>2</sub> /bpabpy <sup>d</sup>	Br <sup>-</sup>	e	ZnO/CdS	TEOA <sup>f</sup> (0.1 M)	0.1 M Bu <sub>4</sub> NBF <sub>4</sub> in CH <sub>3</sub> CN:H <sub>2</sub> O (19/1)	> 400 nm AM 1.5G filter	1	11 : nr : 4	[133]
21	2	SiNWs-H/bpy <sup>g</sup>	Br <sup>-</sup>	h	SiNWs-H	none	0.1 M Bu <sub>4</sub> ClO <sub>4</sub> in CH <sub>3</sub> CN:H <sub>2</sub> O (19/1)	> 600 nm	3	$^{h}$ TOF <sub>CO</sub> = 9 mol active-site <sup>-1</sup> s <sup>-1</sup>	[174]
22	3	SiNWs-H/dmbpy <sup>g</sup>	Br <sup>-</sup>	h	SiNWs-H	none	0.1 M Bu <sub>4</sub> ClO <sub>4</sub> in CH <sub>3</sub> CN:H <sub>2</sub> O (19/1)	> 600 nm	5	$^{h}$ TOF <sub>CO</sub> = 5 mol active-site <sup>-1</sup> s <sup>-1</sup>	[174]

<sup>(</sup>a) 1 atm  $CO_2$ :  $C_4$  (95:5) (b) UiO-67-bpydc is a metal-organic framework containing the 5,5'-dicarboxy-2,2'-bipyridine ligand (c) bpy<sub>PMO</sub> is a periodic mesoporous organosilica material containing the 5,5'-dicarboxy)-2,2'-bipyridine ligand (d) FTO/mesoporous-TiO<sub>2</sub>/catalyst working electrode with +0.6 V bias applied to a FTO/ZnO/CdS counter photoanode electrode. (e) surface coverage = 34 nmol Mn cm² (f) TEOA was present only in counter electrode compartment. (g) SiNWs-H = hydrogen terminated silicon nanowire photocathode (h) active catalyst concentration was unknown, precluding TON calculation. No HCO<sub>2</sub>H or H<sub>2</sub> was observed. (i) [Ru(bpy)<sub>3</sub>](PF<sub>6</sub>)<sub>2</sub> salt (j) [Ru(bpy)<sub>3</sub>]Cl<sub>2</sub> salt

## 6. Conclusions and future outlook

In the last several years, manganese-based transition metal complexes have emerged as promising alternatives to their precious-metal-based rhenium counterparts for use as catalysts in both electrocatalytic  $CO_2$  reduction and photocatalytic  $CO_2$  reduction with visible light-absorbing redox photosensitizers and sacrificial electron donors. Since the first example of electrocatalytic  $CO_2$  reduction with  $MnBr(dmb)(CO)_3$  in  $CH_3CN$  in 2011, a diverse range of homogeneous Mn-based precatalysts have been developed, mainly based on the  $[Mn(\alpha-diimine)(CO)_3L]^{+/0}$  family, although some other ligand architectures are beginning to be investigated.

While the catalytic efficiency of the Mn-based precatalysts is still far from what would be required for a practical application, much progress has been and continues to be made. For example, computational methods and several different experimental techniques, including voltammetry, IR-SEC and TRIR spectroscopy, have been used to develop a deep understanding of the mechanism of CO<sub>2</sub> reduction with these catalysts. More work is still required to observe and characterize some of the proposed intermediates, and the knowledge gained from these studies will aid the design of new, more robust, and more efficient catalysts in the future.

For electrocatalytic CO<sub>2</sub> reduction, it was found that the Mn-based precatalysts are predominantly selective for CO as a reduction product and that catalytic current is only observed in the presence of a Brønsted acid. This contrasts with their use in photocatalytic CO<sub>2</sub> reduction, where a mix of CO, HCO<sub>2</sub>H, and H<sub>2</sub> products is often formed, with product selectivity being determined by various experimental conditions, such as the nature of the solvent used (DMF vs.)

A recent trend has been to immobilize Mn-based CO<sub>2</sub> reduction precatalysts in various ways to produce heterogeneous systems for electrocatalytic, photocatalytic, and photoelectrochemical CO<sub>2</sub> reduction. This is a promising strategy for a variety of reasons, including (i) the fact that catalyst immobilization often imparts stability on the otherwise quite fragile homogeneous Mn-based precatalysts, (ii) it offers the possibility of using aqueous solvents for CO<sub>2</sub> reduction, (iii) it can alter product selectivity, for example, by preventing Mn<sup>0</sup>–Mn<sup>0</sup> dimerization, (iv) it generally boosts catalytic efficiency and turnovers, and (v) it can provide a means of overcoming demanding electrochemical overpotentials by utilizing solar energy (in photoelectrochemical

systems). We therefore expect to see more work in this rapidly evolving area in the near future. Additionally, manipulation of the second coordination sphere has been shown to enhance catalytic activity and can be used to alter the mechanistic pathway. For example, the incorporation of hydroxyl substituents on the  $\alpha$ -diimine ligand framework has provided a local proton source and access to HCO<sub>2</sub>H product in addition to CO, while the incorporation of Brønsted basic methoxy groups in one system enabled hydrogen-bonding interactions in the presence of certain Brønsted acids that allowed access to the previously-elusive protonation-first mechanistic pathway, saving 0.55 V in electrochemical overpotential. We also expect this avenue of research to be pursed more in the future. Finally, we note that great success has been achieved in recent years with various types of supramolecular systems, such as Ru–BL–Re, for photocatalytic CO<sub>2</sub> reduction, where Ru = a Ru-based visible-light absorbing photosensitizer complex, BL = a bridging ligand, and Re = a Re-based CO<sub>2</sub> reduction catalyst [164]. It will therefore be interesting to see if a similar direction can be pursued with analogous Ru–BL–Mn supramolecular systems.

In conclusion, although CO<sub>2</sub> reduction with Mn-based catalysts is in its infancy, with improvements still to be made in terms of catalyst efficiencies and stabilities, a tremendous amount of progress has already been made in just the last seven years, as evidenced by the diverse range of systems summarized in this review. We therefore believe that the future is very promising for this class of CO<sub>2</sub> reduction catalysts.

## Acknowledgements

J.R. thanks the National Science Foundation for support under grant number CHE-1301132. The work at BNL (D.C.G. and M.Z.E.), including use of the Van de Graaff facility of the BNL

Accelerator Center for Energy Research (ACER), was supported by the U.S. Department of Energy (DOE), Office of Basic Energy Sciences, Division of Chemical Sciences, Geosciences & Biosciences, under contract No. DE-SC0012704. K.T.N. is grateful to the DOE for an Office of Science Graduate Student Research (SCGSR) award. Some of this research used resources of the Center for Functional Nanomaterials (CFN) for the fabrication of optics for PR-TRIR experiments and computational modeling studies. The CFN is a U.S. DOE Office of Science Facility at Brookhaven National Laboratory, operating under contract No. DE-SC0012704. We are extremely grateful to Dr. Yasuo Matsubara (Kanagawa University, Japan) for helpful discussions regarding the calculation of equilibrium potentials in aqueous organic solvents.

## References

- [1] P. Lahijani, Z.A. Zainal, M. Mohammadi, A.R. Mohamed, Renew. Sus. Energ. Rev. 41 (2015) 615-632.
- [2] K. Aasberg-Petersen, I. Dybkjaer, C.V. Ovesen, N.C. Schjodt, J. Sehested, S.G. Thomsen, Journal of Natural Gas Science and Engineering 3 (2011) 423-459.
- [3] O.H. Zhang, J.C. Kang, Y. Wang, ChemCatChem 2 (2010) 1030-1058.
- [4] X.W. Yu, P.G. Pickup, J. Power Sources 182 (2008) 124-132.
- [5] N.V. Rees, R.G. Compton, J. Solid State Electrochem. 15 (2011) 2095-2100.
- [6] S. Uhm, M. Seo, J. Lee, Applied Chemistry for Engineering 27 (2016) 123-127.
- [7] W. Reutemann, H. Kieczka, Formic Acid, in: Ullmann's Encyclopedia of Industrial Chemistry, Wiley-VCH Verlag GmbH & Co. KGaA, 2000.
- [8] A.M. Appel, J.E. Bercaw, A.B. Bocarsly, H. Dobbek, D.L. DuBois, M. Dupuis, J.G. Ferry, E. Fujita, R. Hille, P.J.A. Kenis, C.A. Kerfeld, R.H. Morris, C.H.F. Peden, A.R. Portis, S.W. Ragsdale, T.B. Rauchfuss, J.N.H. Reek, L.C. Seefeldt, R.K. Thauer, G.L. Waldrop, Chem. Rev. 113 (2013) 6621-6658.
- [9] F.R. Keene, B.P. Sullivan, Electrochemical and Electrocatalytic Reactions of Carbon Dioxide, Edited by B. P. Sullivan, K. Krist, H. E. Guard: Elsevier, 1993, pp. 1-18.
- [10] J.L. Qiao, Y.Y. Liu, F. Hong, J.J. Zhang, Chem. Soc. Rev. 43 (2014) 631-675.
- [11] W. Leitner, Coord. Chem. Rev. 153 (1996) 257-284.
- [12] J. Hawecker, J.M. Lehn, R. Ziessel, Helv. Chim. Acta 69 (1986) 1990-2012.
- [13] E. Fujita and B. S. Brunschwig Vol.4, Catalysis, Heterogeneous Systems, Gas Phase Systems, Electron Transfer in Chemistry, Edited by Vincenzo Balzani, Wiley-VCH: 2001, pp. 88-126.
- [14] H. Arakawa, M. Areasta, J.N. Armor, M.A. Barteau, E.J. Beckman, A.T. Bell, J.E. Bertcaw, C. Creutz, E. Dinjus, D.A. Dixon, K. Domen, D.L. DuBois, J. Eckert, E. Fujita, D.H. Gibson,

- W.A. Goddart, D.W. Goodman, J. Keller, G.J. Kubas, H.H. Kung, J.E. Lyons, L.E. Manzer, T.J. Marks, K. Morokuma, K.M. Nicholas, R. Periana, L. Que, J.R. Rostrup-Nielsen, W.M.H. Sachtler, L.D. Schmidt, A. Sen, J.A. Somorjai, P.C. Stair, B.R. Stults, W. Tumas, Chem. Rev. 101 (2001) 953-996.
- [15] A.J. Morris, G.J. Meyer, E. Fujita, Acc. Chem. Res. 42 (2009) 1983-1994.
- [16] E.E. Benson, C.P. Kubiak, A.J. Sathrum, J.M. Smieja, Chem. Soc. Rev. 38 (2009) 89-99.
- [17] M.D. Doherty, D.C. Grills, J.T. Muckerman, D.E. Polyansky, E. Fujita, Coord. Chem. Rev. 254 (2010) 2472-2482.
- [18] H. Takeda, O. Ishitani, Coord. Chem. Rev. 254 (2010) 346-354.
- [19] M. Mikkelsen, M. Jorgensen, F.C. Krebs, Energy Environ. Sci. 3 (2010) 43-81.
- [20] D.C. Grills, E. Fujita, J. Phys. Chem. Lett. 1 (2010) 2709-2718.
- [21] C. Costentin, M. Robert, J.M. Saveant, Chem. Soc. Rev. 42 (2013) 2423-2436.
- [22] K.A. Grice, C.P. Kubiak, Recent Studies of Rhenium and Manganese Bipyridine Carbonyl Catalysts for the Electrochemical Reduction of CO<sub>2</sub>, in: M. Aresta, R.V. Eldik (Eds.) Adv. Inorg. Chem.: CO<sub>2</sub> Chemistry, Vol. 66, 2014, pp. 163-188.
- [23] N. Elgrishi, M.B. Chambers, M. Fontecave, Chem. Sci. 6 (2015) 2522-2531.
- [24] K.A. Grice, Coord. Chem. Rev. 336 (2017) 78-95.
- [25] J. Hawecker, J.M. Lehn, R. Ziessel, J. Chem. Soc. Chem. Comm. (1983) 536-538.
- [26] J. Hawecker, J.M. Lehn, R. Ziessel, J. Chem. Soc. Chem. Comm. (1984) 328-330.
- [27] B.P. Sullivan, C.M. Bolinger, D. Conrad, W.J. Vining, T.J. Meyer, J. Chem. Soc. Chem. Comm. (1985) 1414-1415.
- [28] C.D. Windle, R.N. Perutz, Coord. Chem. Rev. 256 (2012) 2562-2570.
- [29] Y. Yamazaki, H. Takeda, O. Ishitani, Journal of Photochemistry and Photobiology C-Photochemistry Reviews 25 (2015) 106-137.
- [30] N. Elgrishi, M.B. Chambers, X. Wang, M. Fontecave, Chem. Soc. Rev. 46 (2017) 761-796.
- [31] H. Takeda, C. Cometto, O. Ishitani, M. Robert, ACS Catal. 7 (2017) 70-88.
- [32] R. Francke, B. Schille, M. Roemelt, Chem. Rev. (2018) ASAP, DOI:
- 10.1021/acs.chemrev.1027b00459.
- [33] F.P.A. Johnson, M.W. George, F. Hartl, J.J. Turner, Organometallics 15 (1996) 3374-3387.
- [34] D. Walther, U. Ritter, R. Kempe, J. Sieler, B. Undeutsch, Chemische Berichte-Recueil 125 (1992) 1529-1536.
- [35] M. Bourrez, F. Molton, S. Chardon-Noblat, A. Deronzier, Angew. Chem. Int. Ed. 50 (2011) 9903-9906.
- [36] F.P.A. Johnson, M.W. George, F. Hartl, J.J. Turner, Organometallics 15 (1996) 3374-3387.
- [37] C. Riplinger, M.D. Sampson, A.M. Ritzmann, C.P. Kubiak, E.A. Carter, J. Am. Chem. Soc. 136 (2014) 16285-16298.
- [38] C. Riplinger, E.A. Carter, ACS Catal. 5 (2015) 900-908.
- [39] J. Agarwal, B.C. Sanders, E. Fujita, H.F. Schaefer, T.C. Harrop, J.T. Muckerman, Chem. Comm. 48 (2012) 6797-6799.
- [40] J. Agarwal, E. Fujita, H.F. Schaefer, J.T. Muckerman, J. Am. Chem. Soc. 134 (2012) 5180-5186.
- [41] J.A. Keith, K.A. Grice, C.P. Kubiak, E.A. Carter, J. Am. Chem. Soc. 135 (2013) 15823-15829.
- [42] J. Agarwal, T.W. Shaw, H.F. Schaefer, A.B. Bocarsly, Inorg. Chem. 54 (2015) 5285-5294.
- [43] Y.C. Lam, R.J. Nielsen, H.B. Gray, W.A. Goddard, ACS Catal. 5 (2015) 2521-2528.
- [44] K.S. Rawat, A. Mahata, I. Choudhuri, B. Pathak, J. Phys. Chem. C 120 (2016) 8821-8831.

- [45] T.W. Schneider, M.Z. Ertem, J.T. Muckerman, A.M. Angeles-Boza, ACS Catal. 6 (2016) 5473-5481.
- [46] J.K. Nganga, C.R. Samanamu, J.M. Tanski, C. Pacheco, C. Saucedo, V.S. Batista, K.A. Grice, M.Z. Ertem, A.M. Angeles-Boza, Inorg. Chem. 56 (2017) 3214-3226.
- [47] K.T. Ngo, M. McKinnon, B. Mahanti, R. Narayanan, D.C. Grills, M.Z. Ertem, J. Rochford, J. Am. Chem. Soc. 139 (2017) 2604-2618.
- [48] C. Riplinger, F. Neese, J Chem Phys 138 (2013) 034106.
- [49] C. Riplinger, B. Sandhoefer, A. Hansen, F. Neese, J Chem Phys 139 (2013) 134101.
- [50] A.D. Becke, Phys. Rev. A 38 (1988) 3098-3100.
- [51] C.T. Lee, W.T. Yang, R.G. Parr, Phys. Rev. B 37 (1988) 785-789.
- [52] A.D. Becke, J. Chem. Phys. 98 (1993) 5648-5652.
- [53] S. Grimme, J. Antony, S. Ehrlich, H. Krieg, J. Chem. Phys. 132 (2010).
- [54] A. Klamt, G. Schuurmann, Journal of the Chemical Society-Perkin Transactions 2 (1993) 799-805.
- [55] D.C. Grills, J.A. Farrington, B.H. Layne, S.V. Lymar, B.A. Mello, J.M. Preses, J.F. Wishart, J. Am. Chem. Soc. 136 (2014) 5563-5566.
- [56] E. Fujita, J.T. Muckerman, Inorg. Chem. 43 (2004) 7636-7647.
- [57] J.M. Smieja, M.D. Sampson, K.A. Grice, E.E. Benson, J.D. Froehlich, C.P. Kubiak, Inorg. Chem. 52 (2013) 2484-2491.
- [58] P.G. Jessop, T. Ikariya, R. Noyori, Chem. Rev. 95 (1995) 259-272.
- [59] A. Hansen, D.G. Liakos, F. Neese, J Chem Phys 135 (2011) 214102.
- [60] Y. Zhao, D.G. Truhlar, J. Chem. Phys. 125 (2006).
- [61] V. Barone, M. Cossi, J. Phys. Chem. A 102 (1998) 1995-2001.
- [62] M. Cossi, N. Rega, G. Scalmani, V. Barone, Journal of Computational Chemistry 24 (2003) 669-681.
- [63] B. Marten, K. Kim, C. Cortis, R.A. Friesner, R.B. Murphy, M.N. Ringnalda, D. Sitkoff, B. Honig, J. Phys. Chem. 100 (1996) 11775-11788.
- [64] M.D. Sampson, A.D. Nguyen, K.A. Grice, C.E. Moore, A.L. Rheingold, C.P. Kubiak, J. Am. Chem. Soc. 136 (2014) 5460-5471.
- [65] Y. Zhao, D.G. Truhlar, Theor. Chem. Acc. 120 (2008) 215-241.
- [66] A.V. Marenich, C.J. Cramer, D.G. Truhlar, J. Phys. Chem. B 113 (2009) 6378-6396.
- [67] Y. Hayashi, S. Kita, B.S. Brunschwig, E. Fujita, J. Am. Chem. Soc. 125 (2003) 11976-11987.
- [68] H.A. Schwarz, R.W. Dodson, J. Phys. Chem. 93 (1989) 409-414.
- [69] Y. Matsubara, D.C. Grills, Y. Kuwahara, ACS Catal. (2015) 6440-6452.
- [70] A.D. McNaught, A. Wilkinson, IUPAC. Compendium of Chemical Terminology (the "Gold Book"), 2nd ed., Blackwell Scientific Publications, Oxford, 1997.
- [71] E.S. Rountree, B.D. McCarthy, T.T. Eisenhart, J.L. Dempsey, Inorg. Chem. 53 (2014) 9983-10002.
- [72] A.M. Appel, M.L. Helm, ACS Catal. 4 (2014) 630-633.
- [73] Y. Matsubara, Acs Energy Letters 2 (2017) 1886-1891.
- [74] M.L. Pegis, J.A.S. Roberts, D.J. Wasylenko, E.A. Mader, A.M. Appel, J.M. Mayer, Inorg. Chem. 54 (2015) 11883-11888.
- [75] C. Costentin, S. Drouet, M. Robert, J.M. Saveant, Science 338 (2012) 90-94.
- [76] J.M. Smieja, C.P. Kubiak, Inorg. Chem. 49 (2010) 9283-9289.
- [77] C. Costentin, M. Robert, J.M. Saveant, Acc. Chem. Res. 48 (2015) 2996-3006.

- [78] J. Agarwal, T.W. Shaw, C.J. Stanton, G.F. Majetich, A.B. Bocarsly, H.F. Schaefer, Angew. Chem. Int. Ed. 53 (2014) 5152-5155.
- [79] C.J. Stanton, J.E. Vandezande, G.F. Majetich, H.F. Schaefer, J. Agarwal, Inorg. Chem. 55 (2016) 9509-9512.
- [80] S.J.P. Spall, T. Keane, J. Tory, D.C. Cooker, H. Adams, H. Fowler, A. Meijer, F. Hartl, J.A. Weinstein, Inorg. Chem. 55 (2016) 12568-12582.
- [81] A. Gennaro, A.A. Isse, E. Vianello, J. Electroanal. Chem. Interfacial. Electrochem. 289 (1990) 203-215.
- [82] R.S. Nicholson, I. Shain, Anal. Chem. 36 (1964) 706-723.
- [83] J.M. Saveant, E. Vianello, Electrochim. Acta 10 (1965) 905-920.
- [84] C. Costentin, G. Passard, J.M. Saveant, J. Am. Chem. Soc. 137 (2015) 5461-5467.
- [85] G.J. Stor, F. Hartl, J.W.M. Vanoutersterp, D.J. Stufkens, Organometallics 14 (1995) 1115-1131.
- [86] P. Christensen, A. Hamnett, A.V.G. Muir, J.A. Timney, J. Chem. Soc. Dalton. Trans. (1992) 1455-1463.
- [87] J. Washington, C.P. Kubiak, Canadian Journal of Chemistry-Revue Canadienne De Chimie 74 (1996) 2503-2508.
- [88] R.J. Haines, R.E. Wittrig, C.P. Kubiak, Inorg. Chem. 33 (1994) 4723-4728.
- [89] B.D. Rossenaar, F. Hartl, D.J. Stufkens, C. Amatore, E. Maisonhaute, J.N. Verpeaux, Organometallics 16 (1997) 4675-4685.
- [90] F. Hartl, B.D. Rossenaar, G.J. Stor, D.J. Stufkens, Recueil Des Travaux Chimiques Des Pays-Bas-Journal of the Royal Netherlands Chemical Society 114 (1995) 565-570.
- [91] C.W. Machan, M.D. Sampson, S.A. Chabolla, T. Dang, C.P. Kubiak, Organometallics 33 (2014) 4550-4559.
- [92] M.D. Sampson, C.P. Kubiak, J. Am. Chem. Soc. 138 (2016) 1386-1393.
- [93] C.W. Machan, C.P. Kubiak, Dalton Trans. 45 (2016) 15942-15950.
- [94] F. Franco, C. Cometto, L. Nencini, C. Barolo, F. Sordello, C. Minero, J. Fiedler, M. Robert, R. Gobetto, C. Nervi, Chem. Eur. J. 23 (2017) 4782-4793.
- [95] J.J. Walsh, C.L. Smith, G. Neri, G.F.S. Whitehead, C.M. Robertson, A.J. Cowan, Faraday Discuss. 183 (2015) 147-160.
- [96] C.W. Machan, C.J. Stanton, J.E. Vandezande, G.F. Majetich, H.F. Schaefer, C.P. Kubiak, J. Agarwal, Inorg. Chem. 54 (2015) 8849-8856.
- [97] X.H. Meng, J. Sedman, F.R. van de Voort, Food Chemistry 135 (2012) 722-729.
- [98] P.L. Cheung, C.W. Machan, A.Y.S. Malkhasian, J. Agarwal, C.P. Kubiak, Inorg. Chem. 55 (2016) 3192-3198.
- [99] Q. Zeng, J. Tory, F. Hartl, Organometallics 33 (2014) 5002-5008.
- [100] M.V. Vollmer, C.W. Machan, M.L. Clark, W.E. Antholine, J. Agarwal, H.F.S. Iii, C.P. Kubiak, J.R. Walensky, Organometallics 34 (2015) 3-12.
- [101] D.W. Agnew, M.D. Sampson, C.E. Moore, A.L. Rheingold, C.P. Kubiak, J.S. Figueroa, Inorg. Chem. 55 (2016) 12400-12408.
- [102] C.W. Machan, C.P. Kubiak, Dalton Trans. 45 (2016) 17179-17186.
- [103] M. Stanbury, J.-D. Compain, M. Trejo, P. Smith, E. Gouré, S. Chardon-Noblat, Electrochim. Acta 240 (2017) 288-299.
- [104] B. Reuillard, K.H. Ly, T.E. Rosser, M.F. Kuehnel, I. Zebger, E. Reisner, J. Am. Chem. Soc. 139 (2017) 14425-14435.
- [105] G. Neri, P.M. Donaldson, A.J. Cowan, J. Am. Chem. Soc. 139 (2017) 13791-13797.

- [106] M.B.M. Orio, F. Molton, H. Vezin, C. Duboc, A. Deronzier, S. Chardon-Noblat, Angew. Chem. Int. Ed. 53 (2014) 240-243.
- [107] T. Scheiring, W. Kaim, J. Fiedler, J. Organomet. Chem. 598 (2000) 136-141.
- [108] R. Usón, V. Riera, J. Gimeno, M. Laguna, Transition Met. Chem. 2 (1977) 123-130.
- [109] H. Behrens, R.-J. Lampe, P. Merbach, M. Moll, J. Organomet. Chem. 159 (1978) 201-217.
- [110] S.R. Wang, C.P. Cheng, T.-I. Ho, Journal of the Chemical Society, Dalton Transactions (1988) 2695-2699.
- [111] V. Yempally, S.J. Kyran, R.K. Raju, W.Y. Fan, E.N. Brothers, D.J. Darensbourg, A.A. Bengali, Inorg. Chem. 53 (2014) 4081-4088.
- [112] H. Fabian, D. Naumann, Methods 34 (2004) 28-40.
- [113] J.M. Smieja, E.E. Benson, B. Kumar, K.A. Grice, C.S. Seu, A.J.M. Miller, J.M. Mayer, C.P. Kubiak, Proc. Natl. Acad. Sci. U.S.A. 109 (2012) 15646-15650.
- [114] M.D. Sampson, J.D. Froehlich, J.M. Smieja, E.E. Benson, I.D. Sharp, C.P. Kubiak, Energy Environ. Sci. 6 (2013) 3748-3755.
- [115] A. Gilbert, J. Baggott, Essentials of Molecular Photochemistry, Blackwell Science Ltd, Oxford, 1991.
- [116] K.N. Tanner, R.L. King, Nature 181 (1958) 963-965.
- [117] K. McFarlane, B. Lee, J. Bridgewater, P.C. Ford, J. Organomet. Chem. 554 (1998) 49-61.
- [118] M.W. George, J.J. Turner, Coord. Chem. Rev. 177 (1998) 201-217.
- [119] J.R. Schoonover, G.F. Strouse, Chem. Rev. 98 (1998) 1335-1355.
- [120] D.M. Dattelbaum, K.M. Omberg, P.J. Hay, N.L. Gebhart, R.L. Martin, J.R. Schoonover, T.J. Meyer, J. Phys. Chem. A 108 (2004) 3527-3536.
- [121] J.M. Butler, M.W. George, J.R. Schoonover, D.M. Dattelbaum, T.J. Meyer, Coord. Chem. Rev. 251 (2007) 492-514.
- [122] A. Vlcek, H. Kvapilova, M. Towrie, S. Zalis, Acc. Chem. Res. 48 (2015) 868-876.
- [123] J.X. Yang, B.R. N'Guessan, A. Dedieu, D.C. Grills, X.Z. Sun, M.W. George, Organometallics 28 (2009) 3113-3122.
- [124] V. Yempally, S. Moncho, F. Hasanayn, W.Y. Fan, E.N. Brothers, A.A. Bengali, Inorg. Chem. 56 (2017) 11244-11253.
- [125] Y. Tabata, Pulse Radiolysis, CRC Press, Boca Raton, FL, 1990.
- [126] G.V. Buxton, Q.G. Mulazzani, Radiation-Chemical Techniques, in: V. Balzani (Ed.)
- Electron Transfer in Chemistry, Wiley-VCH, Weinheim, Germany, 2001, pp. 503-557.
- [127] D.C. Grills, D.E. Polyansky, E. Fujita, ChemSusChem 10 (2017) 4359-4373.
- [128] H.A. Schwarz, J. Chem. Phys. 72 (1980) 284-287.
- [129] P. Pagsberg, A. Sillesen, J.T. Jodkowski, E. Ratajczak, Chem. Phys. Lett. 252 (1996) 165-171
- [130] D.C. Grills, J.A. Farrington, B.H. Layne, J.M. Preses, H.J. Bernstein, J.F. Wishart, Rev. Sci. Instrum. 86 (2015) 044102.
- [131] D.C. Grills, A.R. Cook, E. Fujita, M.W. George, J.M. Preses, J.F. Wishart, Applied Spectroscopy 64 (2010) 563-570.
- [132] J. Hack, D.C. Grills, J.R. Miller, T. Mani, J. Phys. Chem. B 120 (2016) 1149-1157.
- [133] T.E. Rosser, C.D. Windle, E. Reisner, Angew. Chem. Int. Ed. 55 (2016) 7388-7392.
- [134] C.F. Sun, L. Rotundo, C. Garino, L. Nencini, S.S. Yoon, R. Gobetto, C. Nervi, ChemPhysChem 18 (2017) 3219-3229.
- [135] G.K. Rao, W. Pell, I. Korobkov, D. Richeson, Chem. Comm. 52 (2016) 8010-8013.

- [136] B. Shan, T. Baine, X.A.N. Ma, X. Zhao, R.H. Schmehl, Inorg. Chem. 52 (2013) 4853-4859.
- [137] J.J. Walsh, G. Neri, C.L. Smith, A.J. Cowan, Chem. Comm. 50 (2014) 12698-12701.
- [138] M.B. Mizen, M.S. Wrighton, J. Electrochem. Soc. 136 (1989) 941-946.
- [139] F. Franco, C. Cometto, F.F. Vallana, F. Sordello, E. Priola, C. Minero, C. Nervi, R. Gobetto, Chem. Comm. 50 (2014) 14670-14673.
- [140] T.K. Mukhopadhyay, N.L. MacLean, L. Gan, D.C. Ashley, T.L. Groy, M.-H. Baik, A.K. Jones, R.J. Trovitch, Inorg. Chem. 54 (2015) 4475-4482.
- [141] W.N. Olmstead, Z. Margolin, F.G. Bordwell, J. Org. Chem. 45 (1980) 3295-3299.
- [142] F.G. Bordwell, Acc. Chem. Res. 21 (1988) 456-463.
- [143] F.G. Bordwell, R.J. McCallum, W.N. Olmstead, J. Org. Chem. 49 (1984) 1424-1427.
- [144] E. Raamat, K. Kaupmees, G. Ovsjannikov, A. Trummal, A. Kütt, J. Saame, I. Koppel, I. Kaljurand, L. Lipping, T. Rodima, V. Pihl, I.A. Koppel, I. Leito, Journal of Physical Organic Chemistry 26 (2013) 162-170.
- [145] I. Bhugun, D. Lexa, J.M. Saveant, J. Phys. Chem. 100 (1996) 19981-19985.
- [146] E. Fujita, M. Chou, K. Tanaka, App. Organomet. Chem. 14 (2000) 844-846.
- [147] A. Zhanaidarova, H. Steger, M.H. Reineke, C.P. Kubiak, Dalton Trans. 46 (2017) 12413-12416.
- [148] H. Takeda, H. Koizumi, K. Okamoto, O. Ishitani, Chem. Comm. 50 (2014) 1491-1493.
- [149] J.D. Compain, M. Stanbury, M. Trejo, S. Chardon-Noblat, Eur. J. Inorg. Chem. (2015) 5757-5766.
- [150] A.M. Mansour, A. Friedrich, Inorganic Chemistry Frontiers 4 (2017) 1517-1524.
- [151] T.J. Reade, T.S. Murphy, J.A. Calladine, R. Horvath, I.P. Clark, G.M. Greetham, M.
- Towrie, W. Lewis, M.W. George, N.R. Champness, Philos. Trans. R. Soc., A 375 (2017).
- [152] J. Jimenez, I. Chakraborty, P.K. Mascharak, Eur. J. Inorg. Chem. (2015) 5021-5026.
- [153] E. Ustun, M.C. Ayvaz, M.S. Celebi, G. Asci, S. Demir, I. Ozdemir, Inorg. Chim. Acta 450 (2016) 182-189.
- [154] E. Ustun, S. Koc, S. Demir, I. Ozdemir, J. Organomet, Chem. 815-816 (2016) 16-22.
- [155] E. Torralba-Penalver, Y. Luo, J.D. Compain, S. Chardon-Noblat, B. Fabre, ACS Catal. 5 (2015) 6138-6147.
- [156] S.L.-F. Chan, T.L. Lam, C. Yang, S.-C. Yan, N.M. Cheng, Chem. Comm. 51 (2015) 7799-7801.
- [157] J.F. Martinez, N.T. La Porte, C.M. Mauck, M.R. Wasielewski, Faraday Discuss. 198 (2017) 235-249.
- [158] N.T. La Porte, J.F. Martinez, S. Hedstrom, B. Rudshteyn, B.T. Phelan, C.M. Mauck, R.M. Young, V.S. Batista, M.R. Wasielewski, Chem. Sci. 8 (2017) 3821-3831.
- [159] S. Lian, M.S. Kodaimati, D.S. Dolzhnikov, R. Calzada, E.A. Weiss, J. Am. Chem. Soc. 139 (2017) 8931-8938.
- [160] A. Juris, V. Balzani, F. Barigelletti, S. Campagna, P. Belser, A. Vonzelewsky, Coord. Chem. Rev. 84 (1988) 85-277.
- [161] Y.-J. Yuan, Z.-T. Yu, D.-Q. Chen, Z.-G. Zou, Chem. Soc. Rev. 46 (2017) 603-631.
- [162] X. Wang, I. Thiel, A. Fedorov, C. Coperet, V. Mougel, M. Fontecave, Chem. Sci. 8 (2017) 8204-8213.
- [163] Y. Pellegrin, F. Odobel, Comptes Rendus Chimie 20 (2017) 283-295.
- [164] Y. Tamaki, O. Ishitani, ACS Catal. 7 (2017) 3394-3409.

- [165] E. Fujita, B.S. Brunschwig, Homogeneous Redox Catalysis in CO<sub>2</sub> Fixation, in: V. Balzani
- (Ed.) Electron Transfer in Chemistry, Wiley-VCH, Weinheim, 2001, pp. 88-126.
- [166] Y. Tamaki, K. Koike, T. Morimoto, O. Ishitani, J. Catal. 304 (2013) 22-28.
- [167] B. Shan, R. Schmehl, J. Phys. Chem. A 118 (2014) 10400-10406.
- [168] A. Nakada, K. Koike, T. Nakashima, T. Morimoto, O. Ishitani, Inorg. Chem. 54 (2015) 1800-1807.
- [169] A. Nakada, K. Koike, K. Maeda, O. Ishitani, Green Chem. 18 (2016) 139-143.
- [170] Y. Tamaki, T. Morimoto, K. Koike, O. Ishitani, Proc. Natl. Acad. Sci. 109 (2012) 15673-15678.
- [171] A. Paul, D. Connolly, M. Schulz, M.T. Pryce, J.G. Vos, Inorg. Chem. 51 (2012) 1977-1979.
- [172] J.-X. Zhang, C.-Y. Hu, W. Wang, H. Wang, Z.-Y. Bian, Applied Catalysis A: General 522 (2016) 145-151.
- [173] H. Fei, M.D. Sampson, Y. Lee, C.P. Kubiak, S.M. Cohen, Inorg. Chem. 54 (2015) 6821-6828.
- [174] E. Torralba-Peñalver, Y. Luo, J.-D. Compain, S. Chardon-Noblat, B. Fabre, ACS Catal. 5 (2015) 6138-6147.